

DTIC FILE COPY

①

AD-A216 194



DTIC
ELECTE
JAN 02 1990
S B D

BASELINE EXPERIMENT FOR ACTIVE CONTROL
OF STRUCTURAL VIBRATIONS
THESIS

David R. Jacques
Captain, USAF

AFIT/GAE/ENY/89D-15

DEPARTMENT OF THE AIR FORCE
AIR UNIVERSITY

AIR FORCE INSTITUTE OF TECHNOLOGY

Wright-Patterson Air Force Base, Ohio

DISTRIBUTION STATEMENT A

Approved for public release;
Distribution Unlimited

89 12 29 041

AFIT/GAE/ENY/89D-15

BASELINE EXPERIMENT FOR ACTIVE CONTROL
OF STRUCTURAL VIBRATIONS

THESIS

Presented to the Faculty of the School of Engineering
of the Air Force Institute of Technology

Air University

In Partial Fulfillment of the
Requirements for the Degree of
Master of Science in Aeronautical Engineering

David R. Jacques, B.S.

Captain, USAF

December 1989

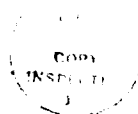
Approved for public release; distribution unlimited

Preface

This experiment is a reincarnation of the Advanced Beam Experiment which was originally developed by the Vibrations Branch of the Flight Dynamics Lab at WPAFB. The modified experiment was constructed and carried out in the AFIT labs, also at WPAFB. The structure and some of the actuators are the same as the original Advanced Beam Experiment, while the remaining hardware is either new or significantly modified from the original experiment.

The primary goal of this project was to develop a simple baseline experiment which could be used to evaluate controllers for the large space structure problem. A secondary goal was to actually demonstrate several of these controllers once the system was developed. In accordance with these goals, the majority of this text describes the development and characterization of the system. For those interested only in the overall configuration and results, Chapters I, V, VI, VII, and VIII should provide all the necessary information. Chapters II, III, and IV are dedicated to the characterization of the components and design considerations used in developing the system.

I would not have made it as far as I did with this experiment had it not been for the help I received from several individuals, and I would like to take this time now to thank them. Dr. Calico, my thesis advisor, provided invaluable guidance. He nudged me along when I was stalled, and he shared my enthusiasm when results started coming in. Mr. Nick Yardich, the lab supervisor, not only made sure I had what I needed, but he also managed to get me most of what I wanted. The lab technicians provided answers to the questions you can't always find in text books, and I found that there are many questions which fit into this category. Most of all, I would like to thank my wife, Lynette, for marrying an engineer. Although she didn't always understand what I was



Distribution/Availability Codes	
Dist	Avail and/or Special
A-1	

doing, she always listened to me, she always sympathized with me, and she celebrated with me when it was all over.

David R. Jacques

Table of Contents

	<u>Page</u>
Preface	ii
List of Figures	vi
List of Tables	viii
Abstract	ix
I. Introduction	1
II. Actuator Characterization	7
Actuator System Overview	7
Proof Mass Actuators-Actuators A and B	8
Structural Dynamics Shaker-Actuator C	19
III. Structure	23
Overview	23
Analytical Models	23
Modal Analysis	33
Final Characterization	39
IV. Sensors/Measurement Channels	42
Overview	42
Accelerometers	42
Integration Circuits	42
Final Measurement Channel	45
V. System Configuration, Modelling, and Verification	50
System Overview	50
Model Development	55
Model Verification	61
VI. Closed Loop Digital Control	66
Optimal Control Methods	66
Optimal Control Design #1	69
Optimal Control Design #2	71
Estimator Inadequacies	74

	<u>Page</u>
VII. Modal Suppression Techniques	78
Theory	78
Modal Suppression Design #1	82
Modal Suppression Design #2	84
VIII. Conclusions and Recommendations	87
Fundamental Issues	87
Capabilities and Limitations of the ABE	88
Bibliography	91
Appendix A: Component Specifications	94
Appendix B: Advanced Beam State Space Formulation	100
Appendix C: Z-248 Personal Computer Modifications	103
Vita	108

List of Figures

<u>Figure</u>	<u>Page</u>
1 Advanced Beam Experiment	6
2 Proof Mass Actuators	9
3 Actuator Compensation Circuit Diagram	11
4 Actuator Compensation Block Diagram	12
5 Actuator A Predicted Frequency Response	14
6 Actuator A Measured Frequency Response	15
7 Actuator B Measured Frequency Response	16
8 APS Shaker-Actuator C	20
9 APS Shaker Frequency Response	21
10 ABE Base Plate with Actuators	24
11 ABE Structure Configuration	25
12 Eigenfunctions for Fixed-Free Beam	30
13 Eigenfunctions for Fixed-Pinned Beam	31
14 Mode Shapes Predicted by FEM Analysis	32
15 Impact Hammer Calibration Device	36
16 Mode Shapes for Z-Axis Bending - Clean Configuration	38
17 Mode Shapes for Z-Axis Bending - Final Configuration	40
18 Integration Circuit Diagram	43
19 Predicted Integrator Frequency Response	44
20 Measured Integrator Frequency Response	46
21 Integrator Frequency Response - Very Low Frequency	47
22 Measurement Channel Block Diagram	48
23 Advanced Beam Setup	51

<u>Figure</u>	<u>Page</u>
24 ABE Final Configuration	52
25 ABE Base Plate Configuration	53
26 ABE Block Diagram	54
27 Normalized Mode Shapes for Z-Axis Bending	60
28 Predicted and Measured Open Loop Response	63
29 Optimal Control Design #1, Position 5 Response	72
30 Optimal Control Design #1, Torque Response	73
31 Optimal Control Design #2, Position 5 Response	75
32 Optimal Control Design #2, Torque Response	76

List of Tables

<u>Table</u>	<u>Page</u>
I. Actuator Maximum Force Outputs at 2 Hz	18
II. Structure Physical Properties	26
III. Predicted Natural Frequencies from Analytical Models	33
IV. Frequencies and Damping - Clean Configuration	39
V. Frequencies and Damping - Final Configuration	41
VI. Measurement Channel Gains	49
VII. Generalized Coordinates	57
VIII. Output Variable Relationships	61
IX. Results of Position 5 Velocity Feedback Tests	64
X. Optimal Control Design #1 Results	71
XI. Optimal Control Design #2 Results	74
XII. Modal Suppression Design #1 Predictions	83
XIII. Modal Suppression Design #1 Results	84
XIV. Modal Suppression Design #2 Predictions	85
XV. Results of Suppression with Direct Measurement Feedback	86

Abstract

The past decade has seen much interest generated in developing a permanent space based platform. One of the primary challenges to establishing these platforms lies in the ability to control the structural vibrations which will inevitably be generated. Many different control methods have been proposed for the large space structure vibration problem, but as yet there are few baseline experiments which allow consistent comparison of these different controllers. Such a baseline experiment must be completely characterized, and all variables affecting the outcome must be understood and controlled. The experiment described in this report represents a small scale attempt to establish such a baseline experiment at AFIT. It consists of an inverted cantilever beam with rectangular cross section. Proof mass actuators mounted on the free end of the beam, and a structural dynamics shaker mounted at a midpoint on the beam provide the control force inputs. The integrated output of beam mounted accelerometers provide velocity feedback, and a programmable controller allows different control algorithms to be easily implemented. In addition to a complete characterization of the system, basic velocity feedback tests were conducted for gain verification. Several optimal controllers were implemented, and modal suppression techniques were attempted to demonstrate control over selected modes while maintaining overall system stability. In all cases experimental results are compared to analytical predictions. Suggestions for improving upon the baseline experiment are made, and fundamental issues regarding experimental research in this area are discussed.

BASELINE EXPERIMENT FOR ACTIVE CONTROL OF STRUCTURAL VIBRATIONS

I. Introduction

It is no secret that man's presence in space is increasing. It should also come as no surprise that the size and complexity of the structures being put in space are also increasing. Projects such as the NASA space station and the Space Defense Initiative (SDI) are but two examples of where this trend is leading to in the near future. These projects will require large structures and very stable platforms in order for functions such as pointing and tracking to be carried out, often with requirements for arc-second accuracy. In the case of the space station, the platform must remain stable and relatively still during docking maneuvers and in the presence of shifting cargo and personnel. Although problems such as these have long since been solved for earth based platforms, the zero-gravity environment presents a much more challenging problem.

In addition to the size of the structure, a second factor compounding the problem is the weight constraints being placed on them due to launch payload considerations. The large size, and relatively light weight of these structures will result in many low frequency, very lightly damped and closely spaced vibration modes. The low damping inherent in these structures must be compensated for in order to minimize the effect of disturbances on the system. Passive damping (i.e. sophisticated shock absorbers) is a partial solution to the problem, but a final stabilization system for a large space structure will most likely require a combination of passive damping and active control. In most cases, it will not be practical or possible to control all the modes. Often the higher frequency modes are not as easily excited, and passive damping will probably be able to

solve most of the problems associated with these modes. The lower frequency modes, on the other hand, most likely will require active control in order to stabilize them. Even with the lower frequency modes however, the cost and complexity of these systems will require hard choices concerning which of these modes can and need to be controlled.

During the past decade there has been a great deal of interest generated in control schemes for large space structures (LSS), and several of the proposed methodologies show great promise. Although most of the work to date has been analytical in nature, several of these control schemes have been implemented in experimental hardware. Examples of experimental work in this field include the following:

NASA Langley Research Center: The active control of a free-free uniform beam using a non-linear, on-off control law. (1)

NASA Langley Research Center: Active vibration damping of a 7 by 10 foot flexible grid. (2)

Jet Propulsion Laboratory: Static shape and dynamic control of a vertical, pinned-free flexible beam. (3)

Lockheed Palo Alto Research Laboratory: The control of both the rigid body and structural modes for a circular plate using High Authority Control/Low Authority Control (HAC/LAC) designs. (4)

Control Research Laboratory, The Ohio State University: The structural control of a free-free flexible beam using classical design techniques and decentralized optimal controllers. (5)

Control Research Laboratory, The Ohio State University: The control of both the rigid body and structural modes of a counterbalanced slewing beam using classical design techniques. (6)

Charles Stark Draper Laboratory: The active vibration damping of a fixed-free flexible beam using Optimal Projection/Maximum Entropy design methodologies. (7)

The projects mentioned above often defined controllers which produced predictable results for a specific system. Missing from much of this work however, are direct comparisons between different controllers implemented on the same system. In order to accomplish this, a baseline experiment is needed in which the structure, sensors, and actuators have been thoroughly characterized, and a good simulation model for the system is available. Such an experiment would be capable of providing useful and valid evaluations and comparisons of candidate control systems. There is work being done towards this end, and examples of this are the NASA-VCOSS Test Facility at the Marshall Space Flight Center, and the 12-meter space truss experiment being developed at the Air Force Flight Dynamic Lab (WRDC/FIBG). Although not on the same grand scale as these two examples, the present work being pursued at AFIT with the reincarnated "Advanced Beam Experiment" is also directed towards providing a baseline experiment for evaluation of candidate control methods.

The Advanced Beam Experiment (ABE) was originally developed by WRDC/FIBG. (See Figure 1.) It was devised to demonstrate active control of a cantilevered beam in two orthogonal bending axes and torsion. The original goal of the experiment was to use inertial sensors and actuators mounted on the beam itself, such that the dynamics of the actuators become coupled to those of the structure they are attempting to control. Several different control schemes were implemented on this structure. Cristler(8) demonstrated active control using a Linear Quadratic Gaussian (LQG) design and modal suppression techniques. Breitfeller(9) used a low authority controller based on root perturbation techniques, and a high authority controller based on a frequency-shaped cost functional. Both of these efforts were partially successful; however, there were several problems which became evident in the original configuration for the ABE. The first of these problems was that the linear proof mass actuators had limited travel (± 0.5 in), and as such were limited to less than rated force output below about 5 Hz. (The first bending mode for each axis was below 2 Hz.) Compounding the actuator problem was that they were all located on a mounting plate attached to the free end of the beam, which happened to be very close to a node for the second and third bending modes. (In fact, the weight of the mounting plate and actuators moved the node of the second and third bending mode towards the free end of the beam.) The second problem with the experiment was low frequency drift present in the sensor channels which caused the proof mass actuators to continually drift into the mechanical stops. It was with full knowledge of these problems, and hopes of correcting them, that AFIT chose to resurrect the ABE so that it may yet again be used to evaluate candidate control methods for structural vibrations.

The modified ABE consists of the inverted fixed-free cantilever beam. Only two of the original four proof mass actuators were available for use; therefore, torsion and

bending in only one plane can be controlled. The two proof mass actuators remain mounted on the base plate at the free end of the beam, but a structural dynamics shaker has been added at a second location to provide better control over 2nd and 3rd mode bending. Sensor channels have been modified to partially correct the low frequency drift problem. Systolic Array Systems' PC-1000 is again used as the programmable estimator/controller.

The goals of the work presented here are to develop a simple baseline experiment in which all variables are understood and controlled. This involves system identification of the structure, actuators and sensors. A model based on the system identification will be developed which accounts for structural damping, damping caused by the actuators, and damping caused by the presences of sensor and actuator cables along the beam. Basic velocity feedback will be used for gain verification, and control over selected modes will be attempted using optimal control and modal suppression methods.



Figure 1. Advanced Beam Experiment

II. Actuator Characterization

Actuator System Overview

The original Advanced Beam Experiment (ABE) used two pairs of linear proof mass actuators mounted in orthogonal axes on a circular base plate attached to the bottom of the beam. Although this allowed for simultaneous control in both bending planes, the combined weight of the actuators (≈ 4 lb/actuator) and base plate (≈ 11 lb) created a node for the second and third bending modes in both planes very close to the free end of the beam. As a result, the actuators were not in a very good position to affect second and third mode bending. To make matters worse, maximum force output from the actuators (≈ 2 lbf/actuator) could not be achieved below about 5 Hz, while the first mode bending frequencies were both below 2 Hz. The end result was that the actuators were only capable of providing efficient control for the torsion mode whose frequency was approximately 13 Hz.

For the reincarnation of the ABE, only two of the original four actuators were available for use. This limited the modified experiment to control in torsion and only one bending plane. Modifications to the beam were considered which would have raised the first mode bending frequencies and moved the nodal positions away from the free end; however, this had the adverse effect of moving the third mode bending frequency out of the linear range of the actuator dynamics. The final decision concerning the actuators was to leave the two proof mass actuators mounted on the base plate to control a single bending plane and torsion. In order to provide greater control over second and third mode bending, a structural dynamics shaker was attached to a higher position on the beam. This went against the original goal of using inertial actuators mounted on the beam itself, but it was the most attractive option available at the time.

Proof Mass Actuators-Actuators A and B

The proof mass actuators used in the ABE are linear dC motors which provide control force using momentum exchange between the base and the moving mass. (See Figure 2.) They consist of a linear motor coil mounted on two support brackets which are mounted to the base plate. The 2 lb cylindrical proof mass contains the motor magnets which are driven by the motor coil. The proof mass travels on linear bearings which allow for ± 0.5 inches of travel. Rubber grommets on the shaft prohibit travel beyond this limit and protect the brackets and proof mass from impact damage. The actuators are instrumented with Linear Variable Differential Transformers (LVDT's) which provide feedback of the relative position between the proof mass and brackets. Mounted on the proof mass is a piezoresistive accelerometer to provide force feedback. The motor coil is driven by a current driving power amplifier circuit. The power amplifier has a current limiter (limited to 2 amps) which prevents burning out the motor coils. With a current of 2 amps from the amplifier card, each motor can provide a maximum of 2 lbf. Specifications on the motors, LVDT's, accelerometers and power amplifiers can be found in Appendix A. A complete description of the development of these actuators can be found in Reference 8.

The open loop response of the actuators exhibited several undesirable characteristics:

1. The low frequency behavior was non-linear due to several factors. The bearing friction and associated hysteresis caused drift of the center position. Also, the limited stroke length would not allow for maximum force output below about 5 Hz. For very low frequencies (< 1 Hz), the bearing friction often overcame the commanded force output of the actuator.

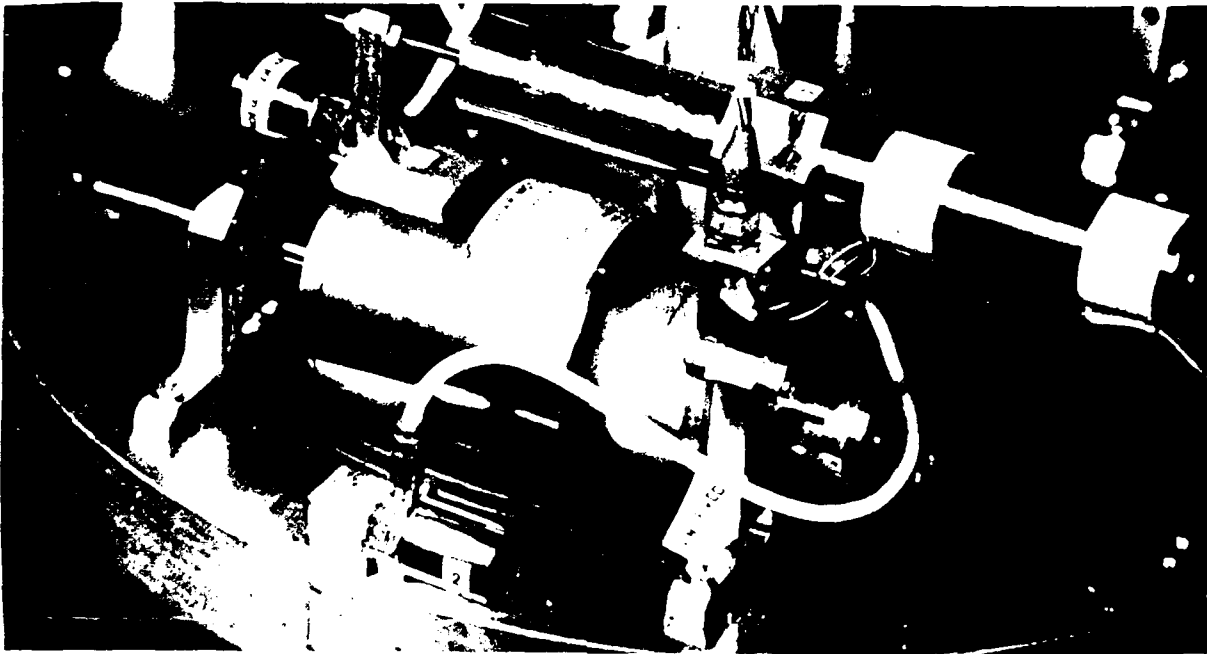


Figure 2. Proof Mass Actuator

2. The zero adjustment of the power amplifier circuit required continual adjustment, as the zero position would shift as a function of both frequency and amplitude.
3. The open loop frequency response has a roll off and associated phase shift in the vicinity of one of the fundamental bending mode frequencies.
4. Non-linear bracket dynamics appeared in the region of 120-150 Hz.

In order to overcome these open loop characteristics, a closed loop feedback system was implemented around each of the actuators. The details of this feedback design and implementation are completely described in Ref. 8, and will not be repeated in this report. The overall goals of the final design were as follows:

1. Provide a flat response over the experiment control bandwidth. While the original ABE limited the control bandwidth to 0 to 50 Hz, the modified experiment uses an expanded control bandwidth of 0 to 100 Hz.
2. The actuator proof mass should remain inertially stationary when uncommanded.
3. The actuator proof mass should remain centered when commanded at varying frequencies and amplitudes.
4. The actuator proof mass should remain within the ± 0.5 inch physical limits.

The actuator compensator circuit diagram is shown in Figure 3. The associated block diagram for the final control configuration is shown in Figure 4. Although the compensator circuit is the same as was used in the original ABE, modifications in the form of varying resistance values were necessary for the following reasons:

1. The characterization of the open loop actuator seemed to change slightly. The low frequency pole shifted higher, the bearing friction deteriorated further, and the actuators were sensitive to environmental changes. (The environmental sensitivity was discovered during a two week period in which the lab air conditioning was inoperable.)
2. The modified ABE required a bandwidth of 0-100 Hz due to the inclusion of third mode bending with a frequency of 60-70 Hz.
3. Different feedback accelerometers were used, and the difference in the sensitivities had to be compensated for.

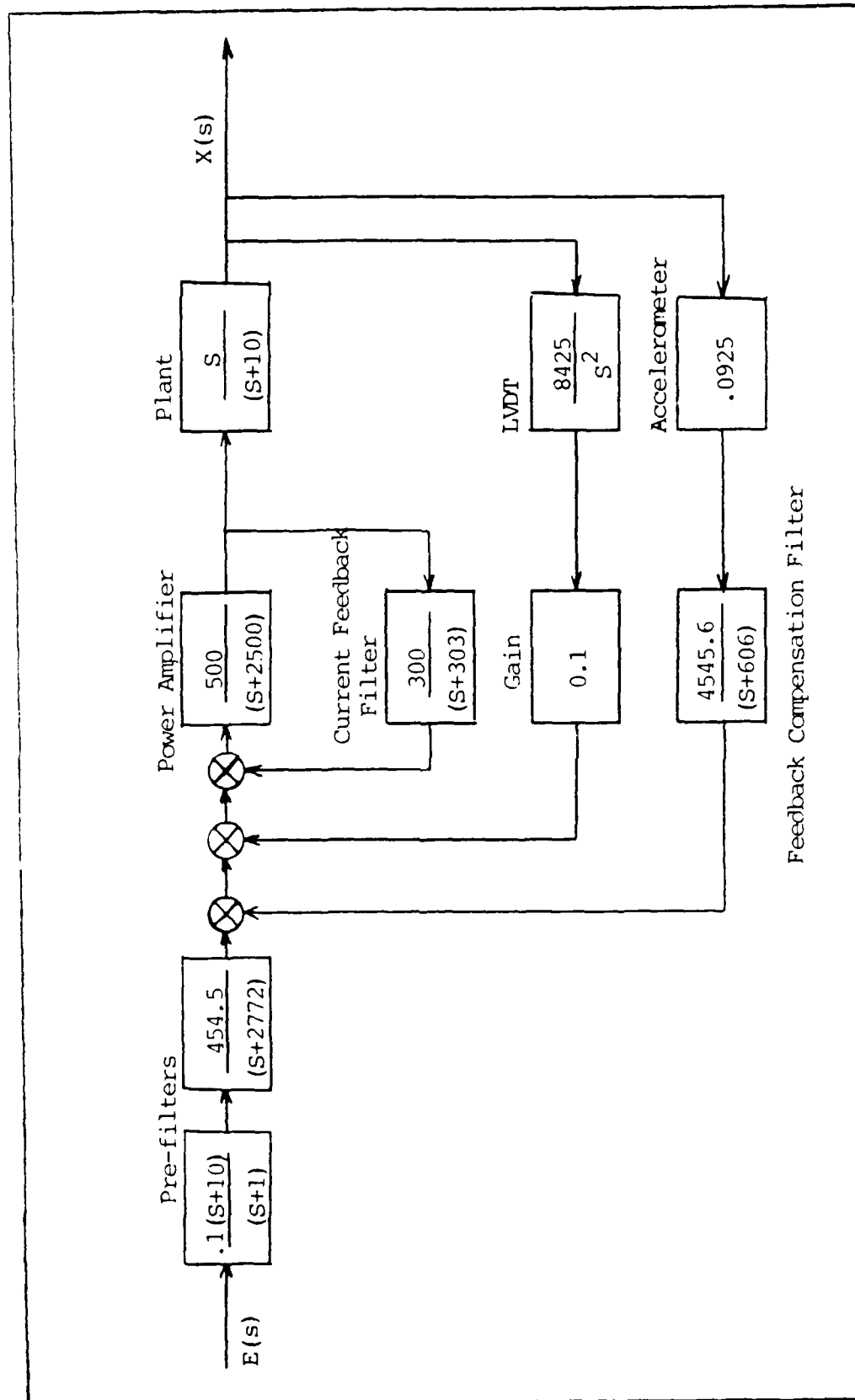


Figure 4. Actuator Compensation Block Diagram

The predicted frequency response of the final configuration for Actuator A is shown in Figure 5. Although the actual output of the motors is force, the transfer function shown is a ratio of accelerometer voltage to command voltage into the power amplifier. The magnitude of response remains fairly flat over the entire control bandwidth, but a phase shift is present at both the low and high end. Even the phase shift, however, stays within ± 10 degrees of zero between first mode (2 Hz) and third mode (63 Hz); therefore, this configuration was deemed adequate pending actual measurements.

Closed loop actuator response was measured using sine dwell tests on the bench mounted actuators. The ratio of proof mass acceleration voltage output to voltage input was measured using a B&K Model 2032 Signal Analyzer which provided both the magnitude and the phase shift. A comparison of the measured and predicted response for actuator A is shown in Figure 6. The overall shape of the response shows good agreement with the prediction. A slightly greater phase shift at the high end of the control bandwidth can be noted in the measured response, but it is still within ± 10 degrees at the third mode bending frequency. The offset in the magnitude of response is attributed to differences in the open loop responses of the actuators. A similar offset is noted in the characterization of actuator B, (see Figure 7), but it shows up as a decrease rather than an increase in amplitude. One possible cause of this is that the mounting bracket consists of two supports; the bearing shaft alignment, which depends on the relative position of these two supports, will determine how freely the proof mass moves along the shaft. The shaft alignment is a function of the initial fabrication of the supports and how carefully the brackets are aligned each time the actuator is remounted. Because the remounting affects the alignment, the characterization of each actuator will change slightly as the actuator is transferred from the calibration bench to the base plate of the structure where it will be used; therefore, the calibration must be rechecked after

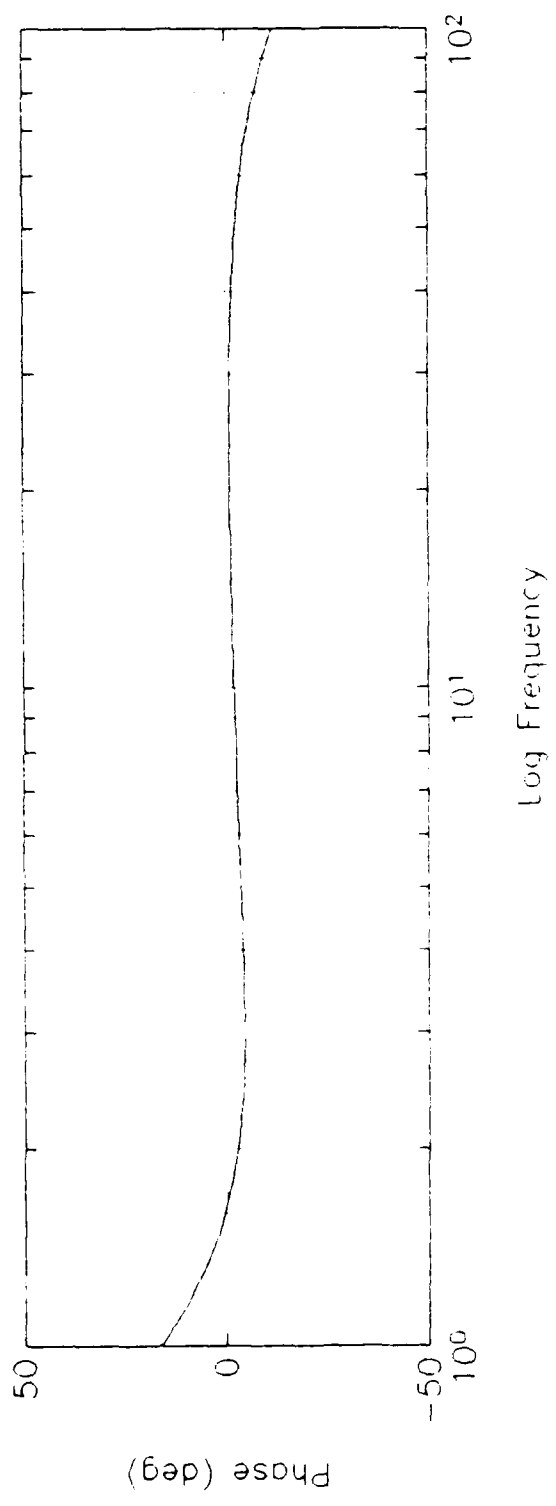
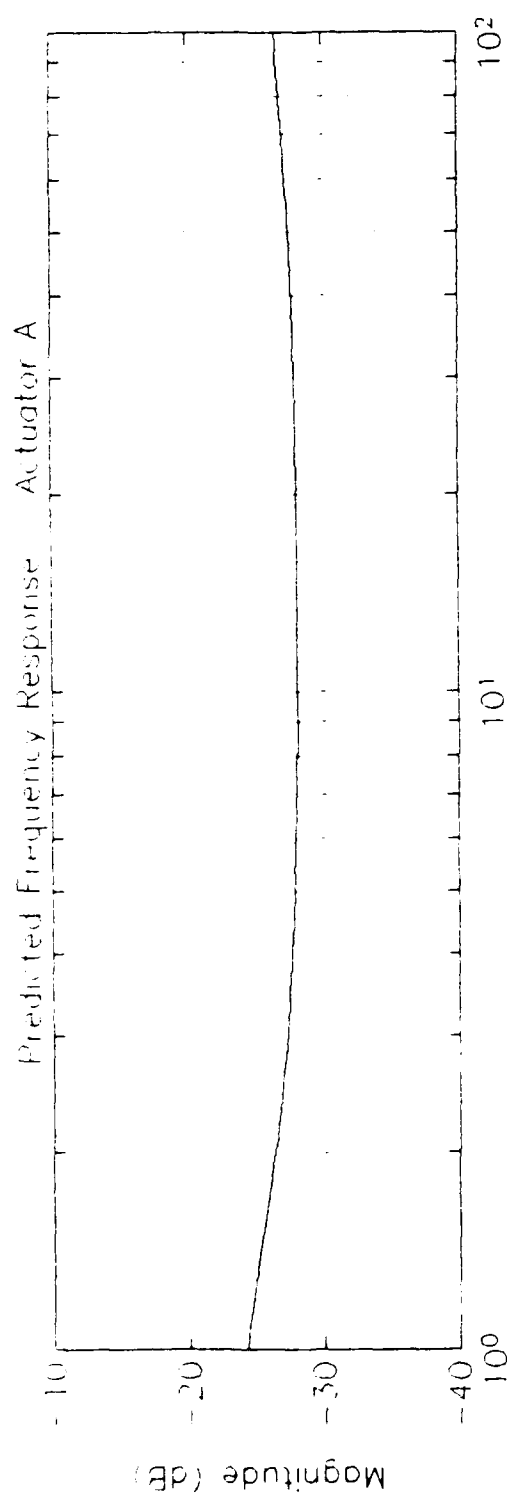
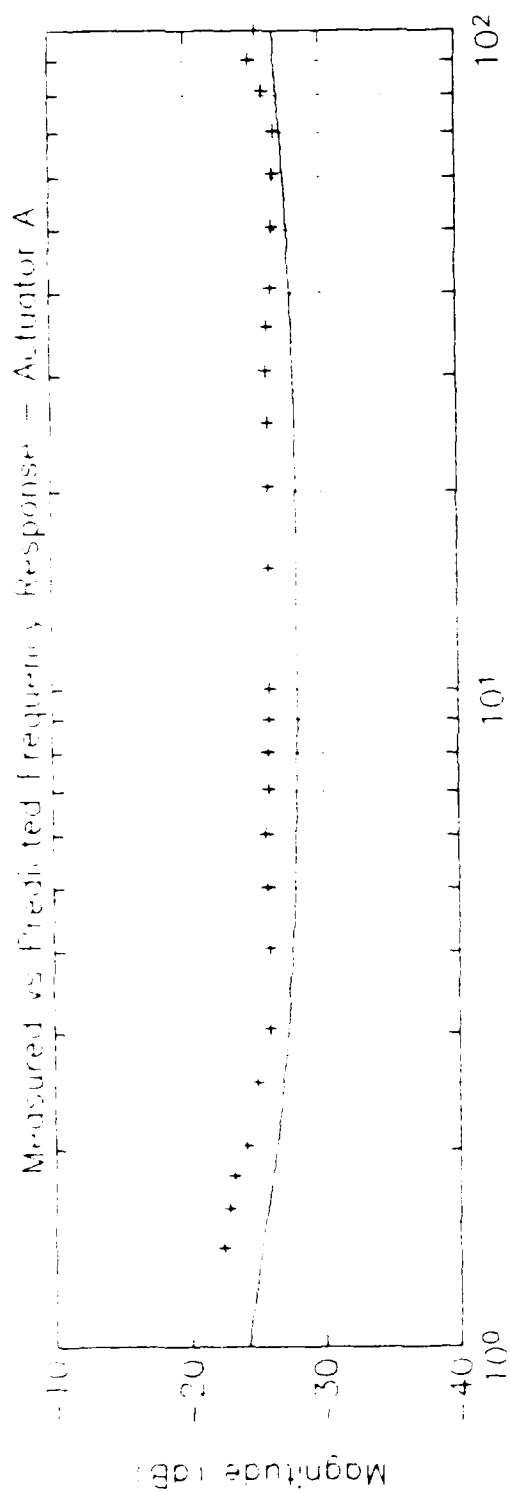


Figure 5. Actuator A Predicted Frequency Response



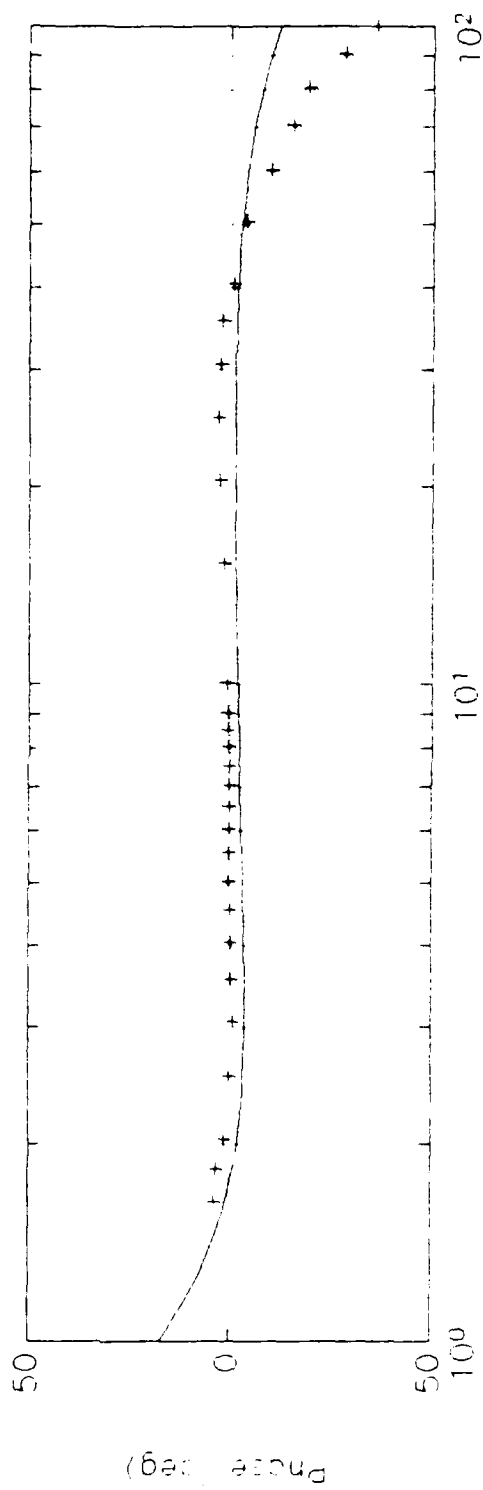
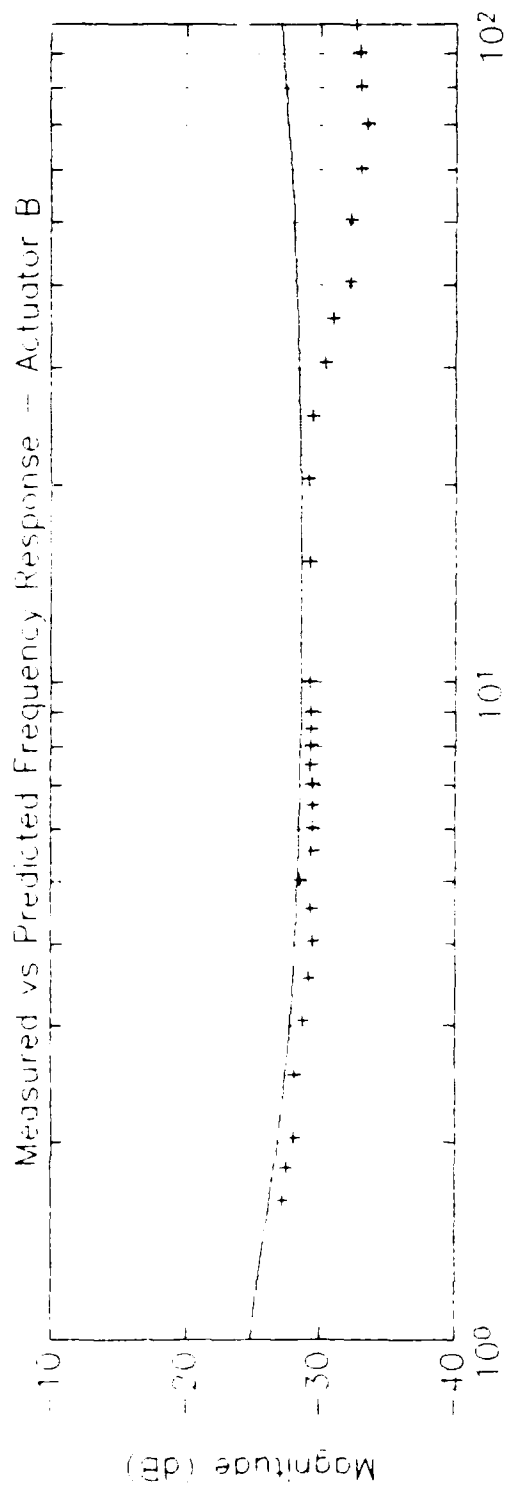


Figure 7. Actuator B Measured Frequency Response

each mounting. In hindsight, a better design would have been to have the shaft set in a one piece cradle assembly which would not be affected by remounting.

Once the actuators had been characterized on a fixed table, a series of tests were conducted in which the base was free to move, thus simulating the actual conditions under which the actuators will be used. The first test re-measured the frequency response of the actuator with the base free to move. The second test measured the maximum force output of the actuators at the first bending mode frequency, and the final test measured the uncommanded proof mass response to base motion. These tests were conducted with the actuator mounted on a slip table. The slip table consists of two plates and bearings which ride in grooves cut in the lower plate. The upper plate, on which the actuator is mounted, is free to move in a single direction. The upper plate is instrumented with an accelerometer; the force output of the actuator can be determined by multiplying the acceleration of the plate by the combined mass of the actuator base, upper plate, and accelerometer. Proof mass acceleration for the uncommanded base motion tests were measured with the accelerometer mounted on the proof mass itself.

The frequency response test of the actuators showed no significant change from those conducted with the base fixed. As was previously noted in Ref 8, the larger displacements associated with the low frequencies showed the cable stiffness to be a factor in the response; however, this should not be a problem in the final configuration because the cables will be moving with the actuator base. Only the accelerometer lead from the proof mass itself will experience relative motion, and this was included to some degree in the earlier characterization.

The maximum force output of the actuator can be limited by one of two factors. Above 5 Hz the maximum output is limited to about 2 lbf by the motor coil capability

(2 amps max). Below 5 Hz the maximum force output is limited by the distance the proof mass can travel. For low frequencies, the peak force can be predicted by

$$F_{out} = m_{pm} \omega^2 d \quad (1)$$

where m_{pm} is the mass of the proof mass and attached accelerometer (5.286×10^{-3} lbf sec²/in), ω is the frequency of the signal driving the motor, and d is the peak displacement. For maximum output, $d = \pm 0.42$ in, because .16 inch of the nominal stroke is lost to the rubber grommets which buffer the proof mass from the mounting brackets. In order to measure the maximum force output at the first bending mode, (all other modes are above 5 Hz), the motor was driven at 2 Hz, and the amplitude was increased to the maximum possible without the proof mass impacting the stops. Table I shows the theoretical vs measured maximum force output at the first mode bending frequency. Adding the maximum output for both actuators indicates the maximum total control force available from the proof mass actuators for control of mode 1 bending is $\pm .59$ lbf.

Table I. Actuator Maximum Force Outputs at 2 Hz

Actuator	F_{pred} (lbf)	F_{meas} (lbf)	Efficiency (%)
A	.361	.298	82.5
B	.361	.292	80.9

The base motion transfer function test is designed to test the ability of the uncommanded actuator control system to maintain an inertial position while the base is moving. This test was performed by driving the base with a structural dynamics shaker,

and measuring the acceleration of the proof mass. A dynamic force gauge between the shaker and slip table base was used to measure the driving force. A perfectly floating proof mass would register zero acceleration regardless of the base motion, provided it stayed within the physical limits of the stops. An ideal viscous damping element would have a 90 degree phase lag between the input and the output. In actual tests, a 70-110 phase lag between the driving force and proof mass acceleration was noted, indicating damping which can reasonably be modelled as viscous. Although these tests could be used to determine quantitatively the actuator damping, the method for beam characterization described in Chapter III includes actuator damping as part of the measured structural damping. For this reason, the actuator damping calculations were unnecessary, and were not carried out. The primary reason for performing this test was to check the viscous damping assumption, and insure that the proof mass could remain centered. Although the proof mass maintained its centering very well for a given frequency, large variations in frequency or amplitude still caused the centering to shift and eventually the actuator would hit the stops. This problem was noted in the previous work with these actuators, and there was not much that could be done about it.

Structural Dynamics Shaker-Actuator C

The third actuator (termed Actuator C) was added to effect more control over second and third mode bending. Actuator C is an Acoustic Power Systems (APS) Model 113-LA Structural Dynamics Shaker, and it is driven by an APS Model 114 dual mode power amplifier. (See Figure 8.) This shaker was chosen because of its long stroke limit (6 inches) and excellent response in the control bandwidth. Specification sheets for the shaker and amplifier are contained in Appendix A.

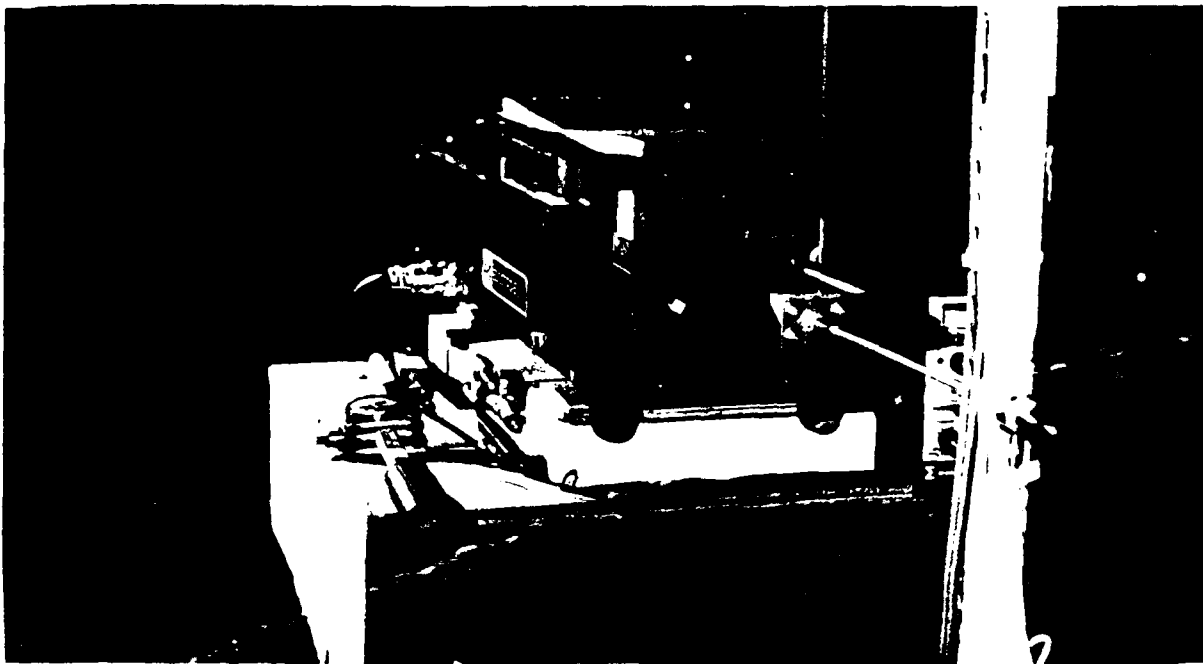


Figure 8. APS Shaker-Actuator C

The APS shaker and amplifier are capable of operating in several different modes depending on whether the shaker body is free to move, whether or not the internal (rubber band) suspension of the shaker is engaged, and which mode (current or voltage) the amplifier is operating in. The best frequency response was obtained using the current mode of operation with the suspension removed. Figure 9 shows the frequency response of the shaker operating in this mode. The exceptionally flat response allows "open loop" operation, thereby eliminating the feedback problems encountered with the proof mass actuators.

In keeping with the original goals of using inertial actuators and sensors for the ABE, the "correct" method for attaching the shaker to the beam would be to suspend the

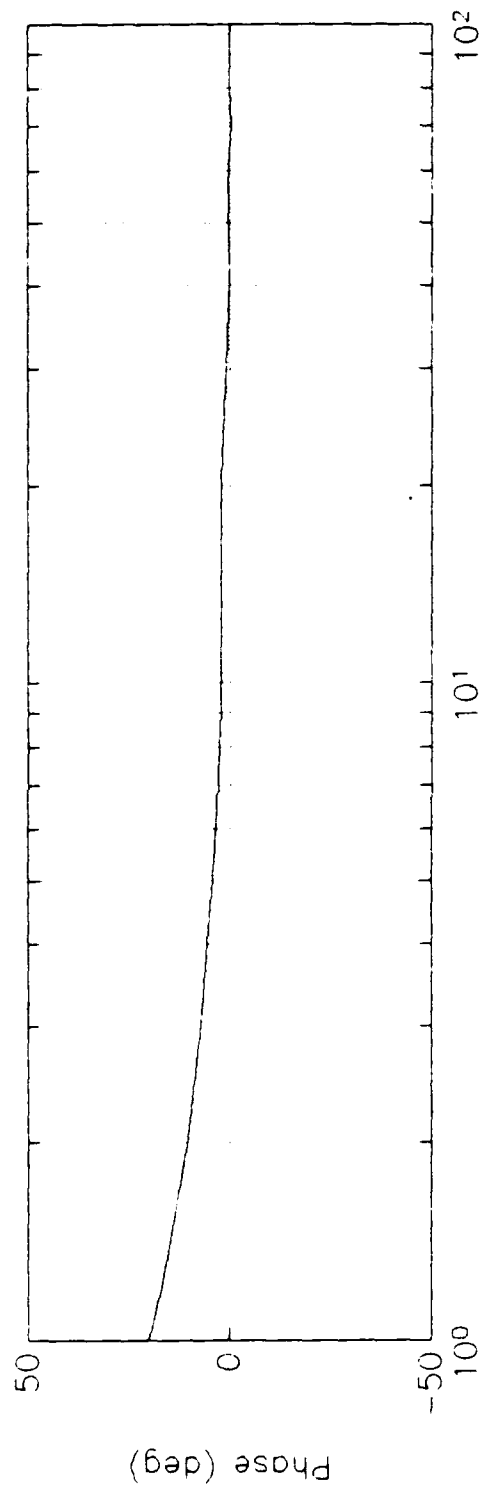
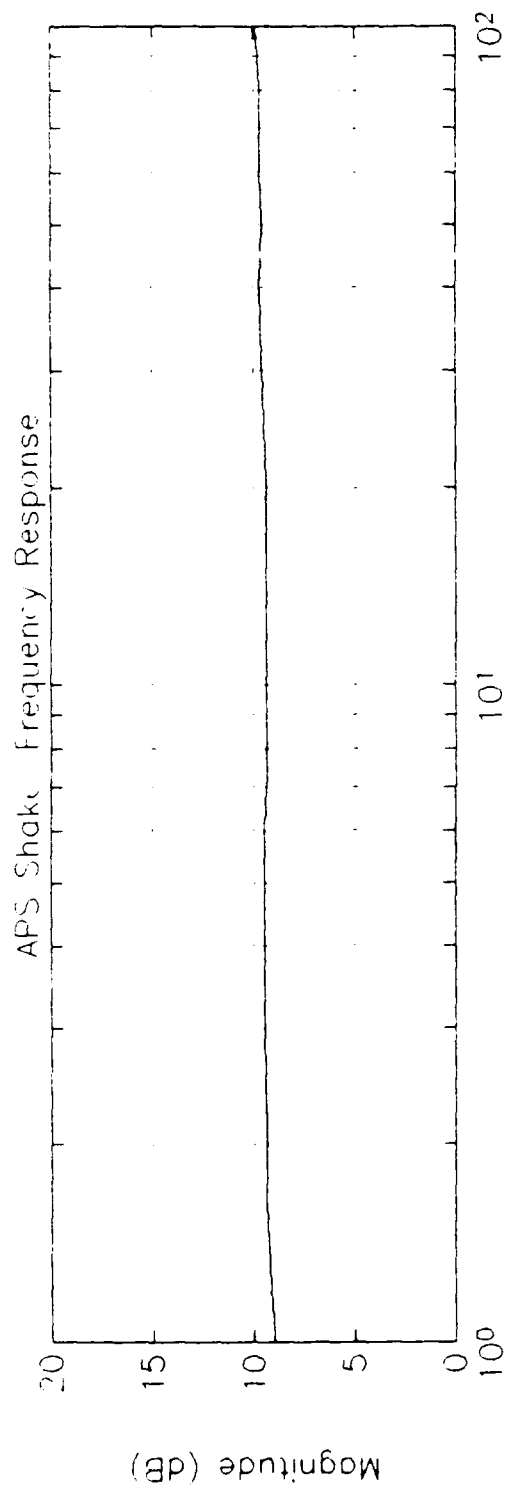


Figure 9. APS Shaker Frequency Response

shaker body from a high ceiling and attach the armature to the beam. The shaker body then acts as a reaction mass in the same way as the proof mass does for the linear motors. In order to not interfere with the first mode bending, the pendulum frequency should be at least an order of magnitude below the bending frequency; this would require a suspension height of 20 to 30 feet.

Alas, the "correct" way is not always the best way for a given situation. Only one APS shaker was available, and because this shaker was also being used to calibrate accelerometers and force gauges, an easier mounting method was required which would allow for relatively quick remounting and realignment. As a result, the shaker was set on a platform external to the beam, and the armature was connected to the beam with a thin push rod. Although this provides for excellent control force input, it is not truly indicative of the space structure problem, in that the dynamics of the shaker do not become part of the structure being controlled. Time permitting, or if a second shaker becomes available for calibration work, suspension from the ceiling should be reconsidered.

III. Structure

Overview

The structure consists of a six foot inverted cantilever beam with a 1" x 3/4" rectangular cross section. A circular disk, (12" diameter, 1" thick), bolted to the free end provides a mounting platform for the proof mass actuators. (See Figure 10.) The disk also provides the primary component of rotary inertia for the torsion mode, thus lowering the torsion mode frequency to within the control bandwidth. The configuration was originally developed by the WRDC Flight Dynamics Lab to exhibit the large space structure characteristics of low frequency, lightly damped and closely spaced vibration modes. The vertical suspension of the beam, and the beam mounted sensors and actuators, are meant to simulate the zero gravity, free vibration environment of a large space structure. While the original ABE considered the first two bending modes in each plane and the first torque mode, the modified ABE discussed here will consider the first three bending modes in only one plane and the first torque mode.

Figure 11 shows the configuration and dimensions of the structure, and Table II lists the physical characteristics.

Analytical Models

The ABE structure is simple enough that a partial differential equation (PDE) model could be used in order to estimate natural frequencies and mode shapes. For ease of analysis, a Bernoulli-Euler beam model was chosen for preliminary analysis. The Bernoulli-Euler model assumes small deflections, linear elastic behavior, no axial (x-axis) forces, and homogenous material characteristics. In addition, the model neglects shear deformation and rotatory inertia effects. Of all these assumptions, the one

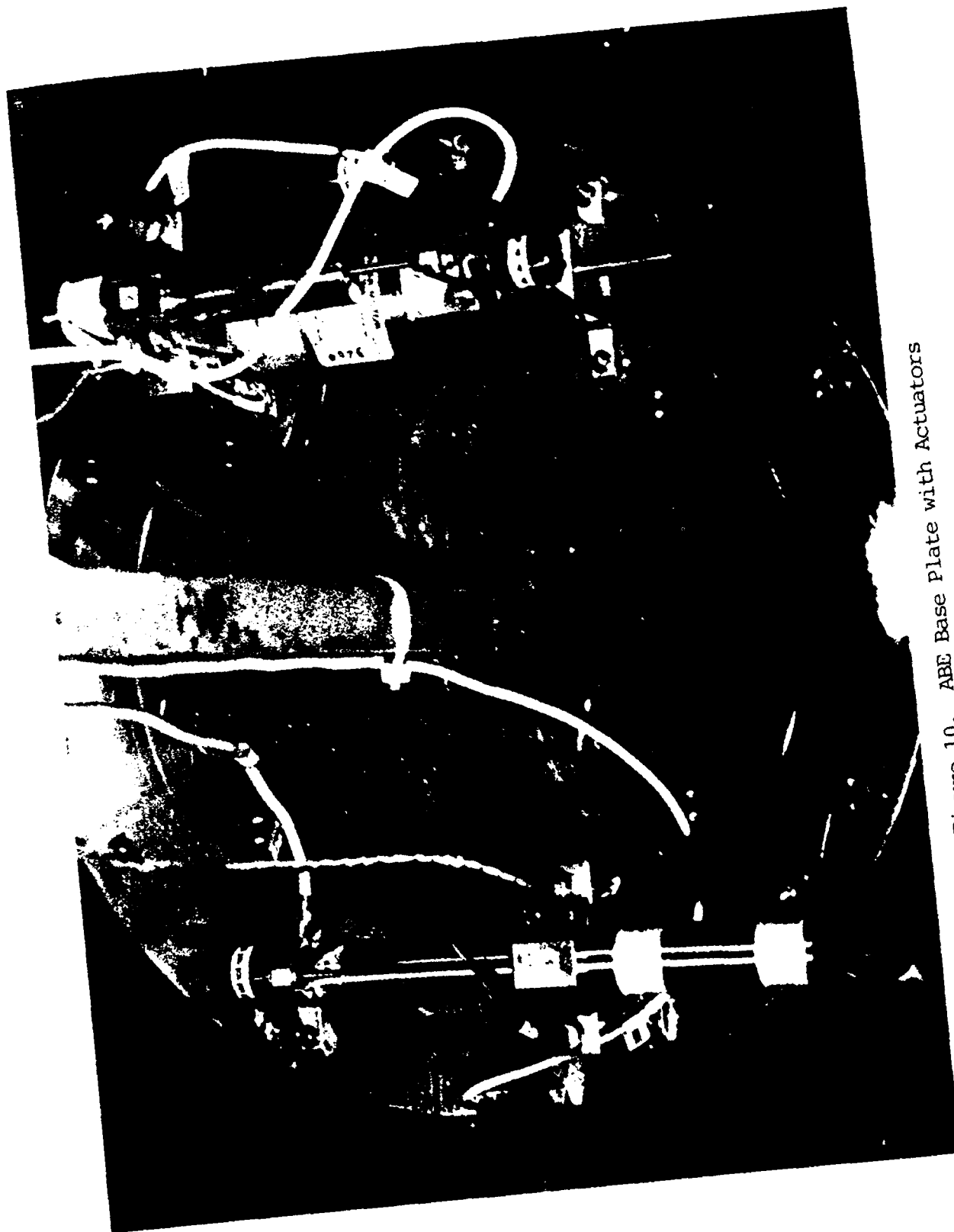


Figure 10. ABE Base Plate with Actuators

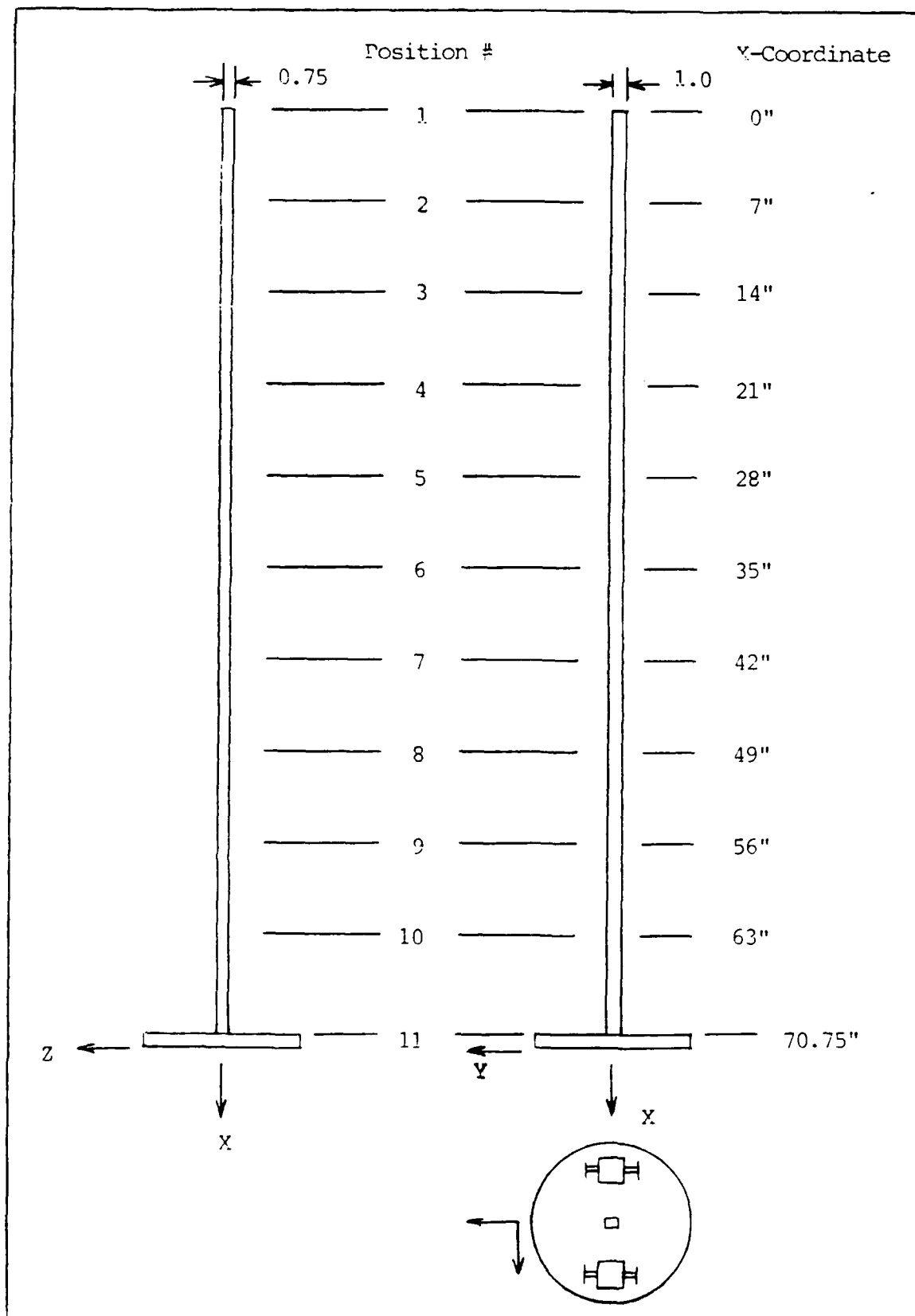


Figure 11. ABE Structure Configuration

Table II. Structure Physical Properties

Property Description	Value	Units
Beam Length (L)	70.75	in
Y Cross-Section Width (a)	1.01	in
Z Cross-Section Width (b)	0.758	in
Cross-Section Area (A)	0.7656	in ²
Young's Modulus (E)	10.8x10 ⁶	lbf/in ²
Shear Modulus (G)	4.1x10 ⁶	lbf/in ²
Beam Density (ρ)	2.591x10 ⁻⁴	lbf·sec ² /in ⁴
Beam Mass (m_b)	1.403x10 ⁻²	lbf·sec ² /in
Y Moment of Inertia (I_y)	3.667x10 ⁻²	in ⁴
Z Moment of Inertia (I_z)	6.508x10 ⁻²	in ⁴
Torsional Moment of Inertia (K)*	7.913x10 ⁻²	in ⁴
Polar Moment of Inertia (I_{xx})	1.865x10 ⁻³	lbf·sec ² /in
Plate Diameter (d)	12.0	in
Plate Thickness (t)	1.0	in
Plate Mass (m_p)	2.847x10 ⁻²	lbf·sec ² /in
Plate X Mass Moment of Inertia (I_{Dmx})	0.5125	lbf·sec ² ·in
Plate Y-Z Mass Moment of Inertia (I_{Dm})	0.2562	lbf·sec ² ·in

* Adjusts for the rectangular cross-section

$$K = ab^3[16/3 - 3.36(b/a)(1 - b^4/12a^4)]/8 \quad (10:290)$$

most severely violated by the ABE structure is that of no axial forces. The relatively heavy disk and actuator assembly at the bottom (free end) of the beam actually places the beam in tension. However, the PDE model is only being used for preliminary estimates; therefore, the assumptions are easily justified. Experimental modal analysis will be used for the final characterization and model development, and this process will account for axial loading effects, as well as shear deformation and rotatory inertia.

The Bernoulli-Euler equation of motion for Z-axis bending is

$$EI \frac{\partial^4 v(x,t)}{\partial x^4} + \rho A \frac{\partial^2 v(x,t)}{\partial t^2} = 0 \quad (2)$$

The boundary conditions for the ABE structure are

$$v(0,t) = 0 \quad (3)$$

$$\frac{\partial v(0,t)}{\partial x} = 0 \quad (4)$$

$$V_L + EI \frac{\partial^3 v(L,t)}{\partial x^3} = 0 \quad (5)$$

$$M_L - EI \frac{\partial^2 v(L,t)}{\partial x^2} = 0 \quad (6)$$

where V_L and M_L represent the inclusion of the base disk in the boundary conditions.

$$V_L = -m_p \frac{\partial^2 v(L,t)}{\partial t^2} \quad (7)$$

$$M_L = -I_{om} \frac{\partial^2}{\partial t^2} \left(\frac{\partial v(L,t)}{\partial x} \right) \quad (8)$$

If we employ separation of variables

$$v(x,t) = \phi(x) \theta(t) \quad (9)$$

we can then set up the eigenvalue problem

$$\phi^{(4)}(x) - \beta^4 \phi(x) = 0 \quad (10)$$

$$\ddot{\theta}(t) + \beta^4 \frac{EI}{\rho A} \theta(t) = 0 \quad (11)$$

The general solution of the position dependent equation can be written as

$$\phi(x) = A \sin(\beta x) + B \cos(\beta x) + C \sinh(\beta x) + D \cosh(\beta x) \quad (12)$$

Applying the boundary conditions (equations 3-8) to equation 12, and eliminating any possibilities of translational modes ($\beta=0$), results in

$$A = -B, \quad C = -D \quad (13), (14)$$

$$\begin{bmatrix} F_{11} & F_{12} \\ F_{21} & F_{22} \end{bmatrix} \begin{bmatrix} A \\ B \end{bmatrix} = \begin{bmatrix} 0 \\ 0 \end{bmatrix} \quad (15)$$

$$F_{11}(\beta) = m_p \frac{\beta}{\rho A} [\sin(\beta L) - \sinh(\beta L)] - [\cos(\beta L) + \cosh(\beta L)] \quad (16)$$

$$F_{12}(\beta) = m_p \frac{\beta}{\rho A} [\cos(\beta L) - \cosh(\beta L)] + [\sin(\beta L) - \sinh(\beta L)] \quad (17)$$

$$F_{21}(\beta) = \frac{I_{Dm}}{\rho A} \beta^3 [\cos(\beta L) - \cosh(\beta L)] + [\sin(\beta L) + \sinh(\beta L)] \quad (18)$$

$$F_{22}(\beta) = \frac{I_{Dm}}{\rho A} \beta^3 [\sin(\beta L) + \sinh(\beta L)] + [\cos(\beta L) + \cosh(\beta L)] \quad (19)$$

The n modal frequencies can be determined by setting $\det[F(\beta)] = 0$ and, from the time dependent equation

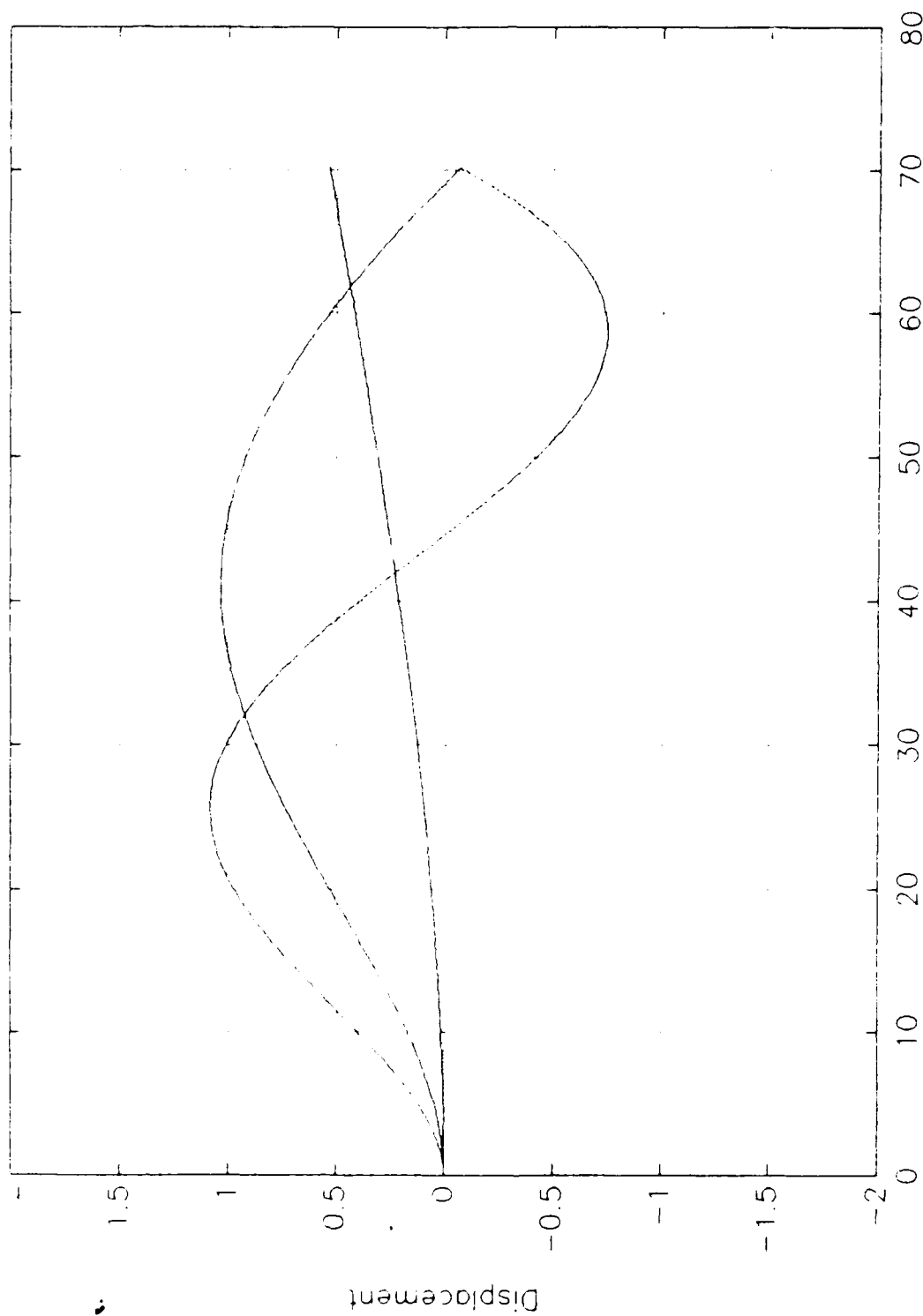
$$\omega_n = \beta_n^2 \sqrt{EI/\rho A} \quad (20)$$

Once the values of β_n have been determined, the coefficients of the eigenfunctions (equation 12) can be determined from equation 15.

For this preliminary analysis the actuators were not included in the mass of the disk. Figure 12 shows the eigenfunctions predicted by the PDE model for the first three modes. Of special note is that the weight of the base disk causes the structure to behave much like a fixed-pinned beam. For comparison, a PDE model of a fixed-pinned Bernoulli-Euler beam was developed, and the eigenfunctions for this model are shown in Figure 13. Modes 1 and 2 for the fixed-pinned beam correspond closely to modes 2 and 3 for the fixed-free beam.

A finite element model (FEM) for the modified ABE structure was developed by Capt. Kevin Silva, a fellow AFIT student. This model included the mass and inertias of the actuator bases. Because the proof masses theoretically "float" when uncommanded, the proof masses themselves were not included in the FEM analysis. Figure 14 shows the mode shapes predicted by the FEM analysis, and a comparison of the predicted natural frequencies for the FEM and PDE model is presented in Table III.

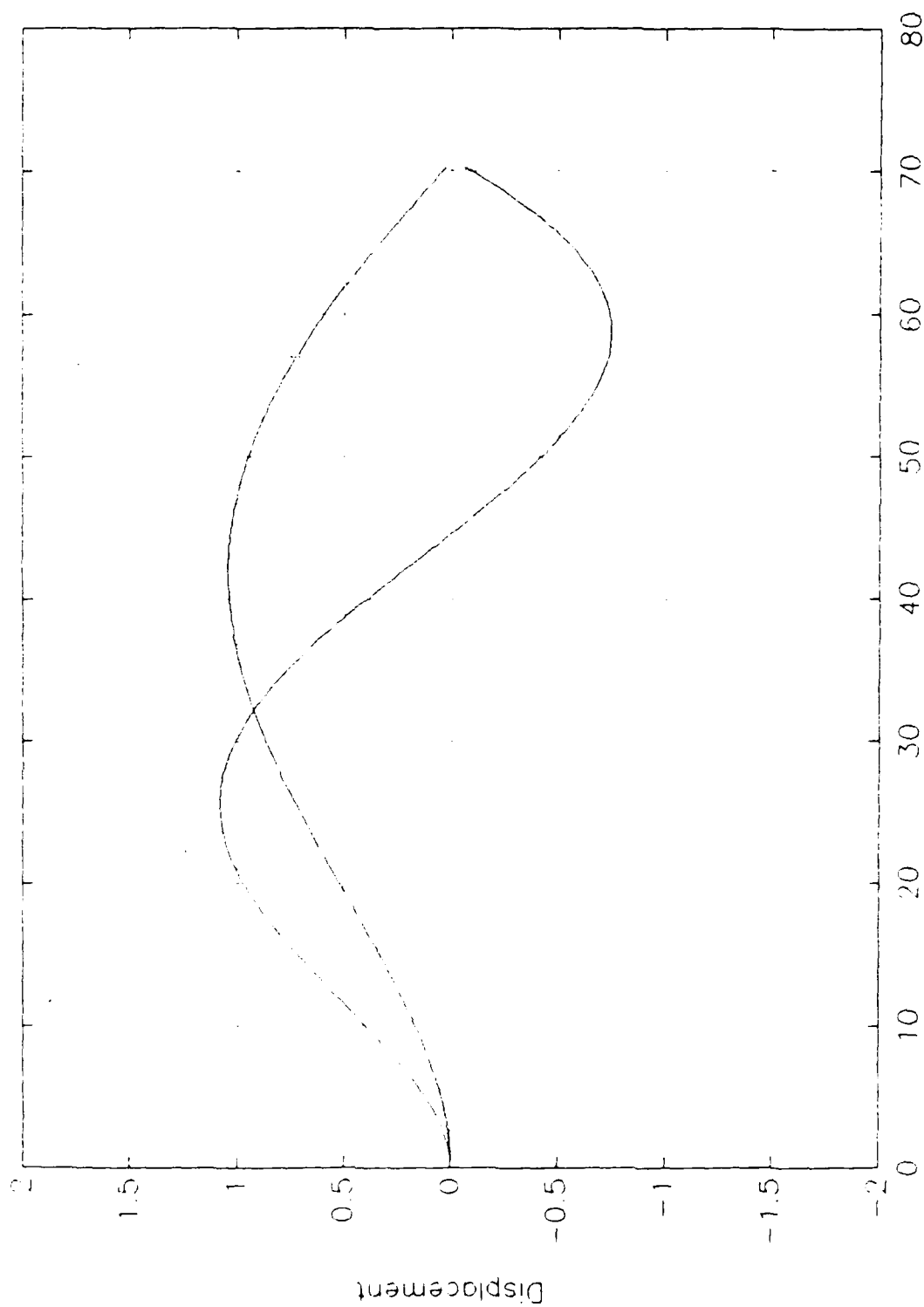
Modes 1, 2 & 3 for Fixed-Free Bernoulli-Euler Beam



Beam Position (Inches)

Figure 12. Eigenfunctions for Fixed-Free Beam

Modes 1 & 2 for Fixed-Pinned Bernoulli-Euler Beam



Beam Position (Inches)

Figure 13. Eigenfunctions for Fixed-Pinned Beam

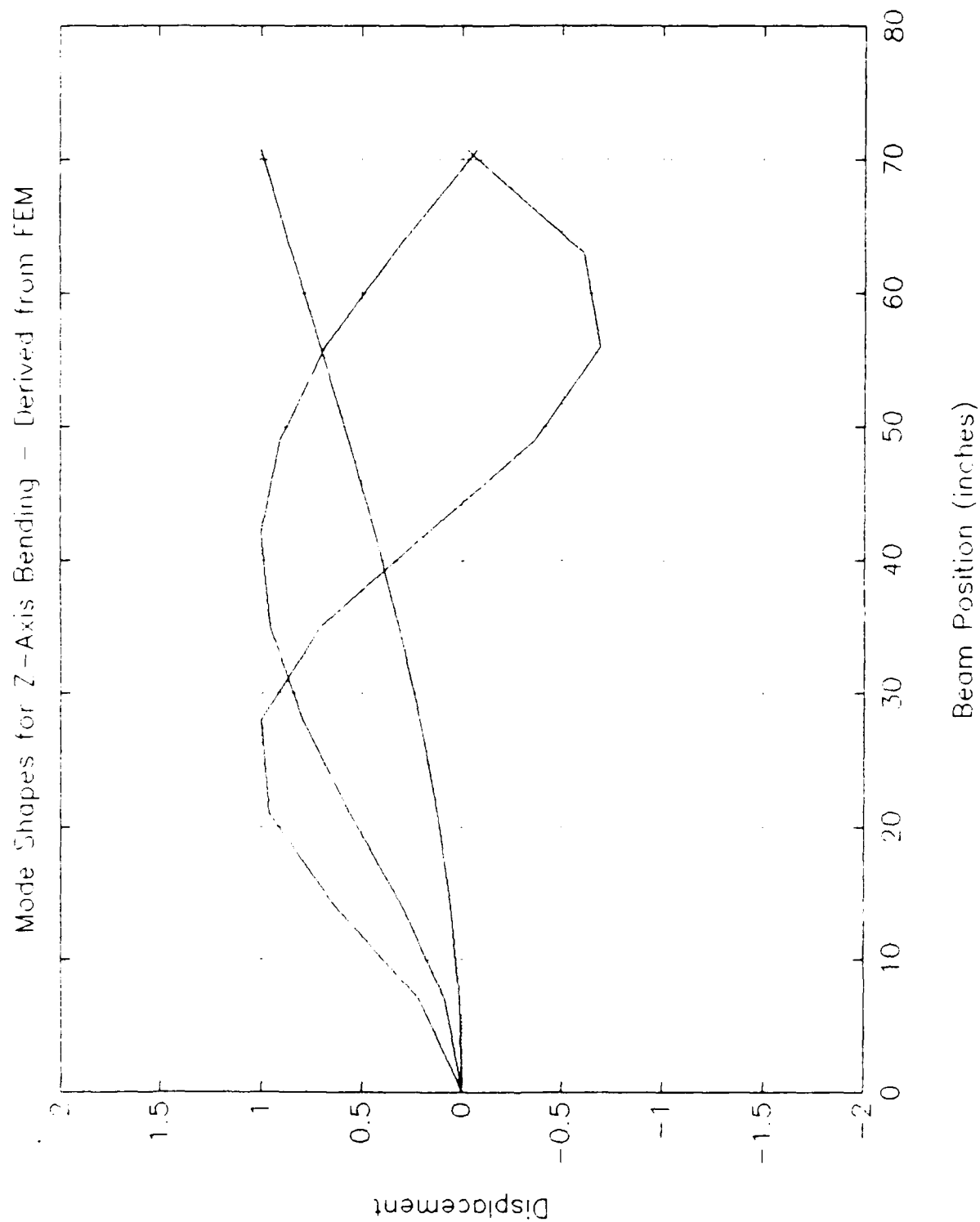


Figure 14. Mode Shapes Predicted by FEM Analysis

Table III. Predicted Natural Frequencies from Analytical Models

	Fixed-Free Beam	Fixed-Pinned Beam	FEM Model
Mode #	Frequency (Hz)	Frequency (Hz)	Frequency (Hz)
1	2.17	N/A	2.06
2	28.01	27.44	27.75
3	76.36	76.36	76.10
4	138.35	137.54	Not Calculated
5	240.29	238.74	Not Calculated

Modal Analysis

Modal analysis is the process of extracting the dynamic characteristics of a vibrating system from experimentally derived frequency response functions. The frequency response functions (FRF's) are measured ratios of the system response to the force input. The characteristics of interest are the resonant frequencies, damping ratios and mode shapes. Although modal masses are not usually calculated directly from modal analysis data, the mode shapes can be normalized in such a way that the modal masses take on values of unity. Modal analysis provides a means for measuring the dynamic characteristics of a structure, as opposed to relying on an analytical model to provide this information. Modal analysis also provides measurements of structural damping which can not be predicted by a PDE or finite element model. Because a large space structure will most likely be assembled for the first time in space, it may not be possible or practical to perform a complete modal analysis on the final structure. However, the present goal of the ABE is to develop a baseline experiment in which the structure is

completely understood; therefore, modal analysis, as the most accurate means available for characterizing the structure, will be used as the basis for the model of the system.

Modal analysis relies on three main assumptions: linearity, time invariance, and observability. These assumptions are easily justified for the ABE structure. Small displacements will confine the system to a linear operating region, excitations will always begin while the system is at rest or a known initial condition, and sensors can be placed on the beam such that all modes of vibration are visible. An additional assumption, based on linearity, is the reciprocity principle. This states that for linear systems, the energy stored in the structure ($KE + PE$) is symmetric in the variables of force and velocity. Stated another way, a force at location A and measurement at location B will yield the same FRF as a force at B and measurement at A. The reciprocity principle greatly simplifies the procedure of modal analysis by allowing us to vary the location of either the force input or the response measurement, while keeping the location of the other constant. An excellent description of the modal analysis theory and method is contained in reference 11.

An additional benefit of the linearity assumption is that, within the limitations of the measuring devices, a measured response to any known input enables us to predict the response to any other input. The two most common inputs used to measure FRF's are impacts and uniform (or wide-band Gaussian) random noise. Both of these inputs can provide a relatively flat frequency spectrum for the bandwidth of interest, thus equally exciting all vibration modes in that bandwidth. For the present project, both impact and random noise inputs (in separate tests) will be used to excite the structure. For the impact tests, the response coordinate will remain stationary while the location of the impact will vary. For the random noise tests, the opposite method will be used. A B&K signal analyzer will be used to measure the complex FRF's, and Structural

Measurements System's STAR Modal software package (12) will be used to derive natural frequencies, damping ratios, and mode shapes from the measurements. The STAR Modal package uses a complex polynomial curve fit which employs the Rational Fraction Least Squares method. (Other curve fit methods are available in the software, but this was the method used.) Where possible, damping ratios calculated by STAR Modal are compared to log decrement measurements from time response plots.

A series of impact tests were performed on the "clean" structure. The clean configuration consisted of the actuator bases mounted on the base disk. The proof masses were removed to simulate the floating of the uncommanded actuator during Z-axis bending and torsion. No wires were present on the structure, and the shaker was also not attached. This configuration is the same as was used for the FEM discussed previously. The impact hammer for these tests was instrumented with a B&K Model 8200 force gauge, and an eraser tip for the hammer was chosen in order to get sufficient energy into the structure for exciting low frequency modes. An impact calibrator was developed based on a method described in reference 11. The calibrator consists of a pendulous mass to which the accelerometer being used for response measurements is attached. (See Figure 15.) The accelerometer was attached with beeswax, this being the same method of attachment for the actual test. By using the same sensors, amplifiers, signal conditioners and impact motion for the calibration as will be used for the actual tests, a transductance ratio can be calculated which embodies the calibrations for both the impact and response measurement channels.

$$R = m_c (E_s/E_t) \quad (21)$$

where E_f is the force voltage, E_a is the acceleration voltage and m_c is the mass of the calibrator. Although the transductance ratio is actually a function of frequency, it was relatively flat across the control bandwidth for these tests and was averaged into a single constant.



Figure 15. Impact Hammer Calibration Device

The B&K signal analyzer has the capability of overlaying separate measurement windows on each of the input channels. For the impact tests, a transient force window was used on the hammer impact measurements, and an exponential window was used on the accelerometer response. The force window is set equal to unity during the duration of the impact, and then a trailing cosine quickly tapers off to zero. This reduces the

effect of stray signals from the hammer after the impact has occurred. The exponential window is designed to minimize leakage errors associated with terminating the response measurement before all vibrations have damped out, as is often the case for very lightly damped structures. The exponential window starts at unity where the impact occurs, and decays to a value of approximately .01 by the end of the measurement period. Because the exponential window adds apparent damping to the measured response, the apparent damping must be subtracted from the measured damping in order to determine the structural damping.

Frequency resolution requirements dictated three separate tests to measure the first three Z-axis bending modes and the first torsion mode. The first test used a 25 Hz bandwidth to measure the first bending mode, the second used a 100 Hz bandwidth to measure bending modes 2 and 3, and the third used a 50 Hz bandwidth to measure the torque mode. The location of the response coordinate for each test was selected to obtain a good response for the particular mode being measured, and an average of 10 measurements were taken for each combination of impact and response coordinates. Table IV lists the natural frequencies and damping ratios obtained from impact testing of the clean configuration, and Figure 16 shows the associated mode shapes. The mode shapes have been normalized to a maximum amplitude of 1 for comparison to the FEM derived modes. The first mode shows very little error between the FEM and measured data, with increasing error showing up in the estimates for the higher frequency modes. Once again, of special interest are the mode shape components at the free end for modes 2 and 3. Other tests on these modes revealed that Z-axis rotation of the base plate was taking place, which accounts for the fixed-pinned nature of the mode shapes. The node near the free end of the beam created by the heavy disk and actuators greatly reduces the effectiveness of the proof mass actuators in controlling modes 2 and 3. Sensors

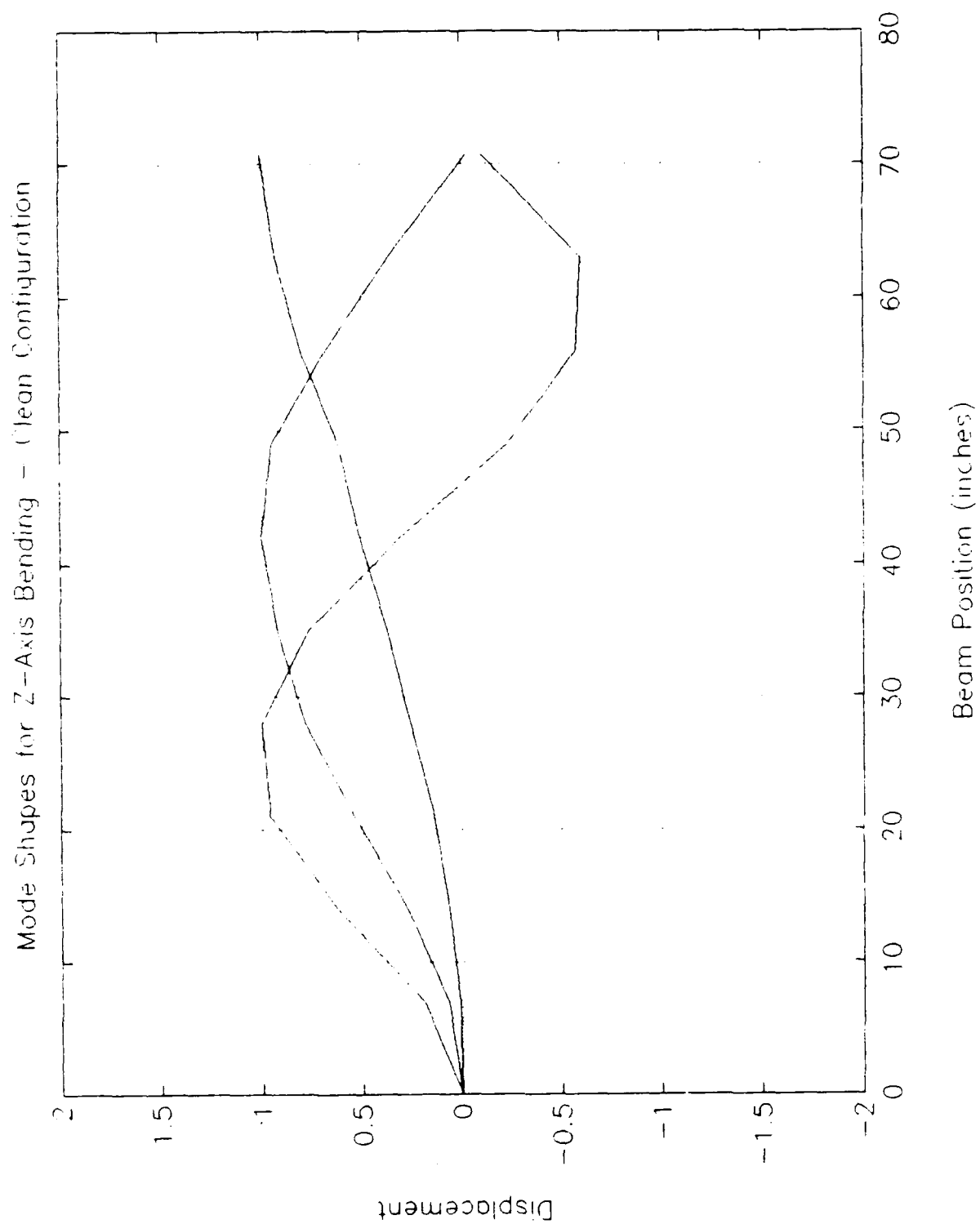


Figure 16. Mode Shapes for Z-Axis Bending - Clean Configuration

located at the free end will also see limited response from these modes. For these reasons, position 5 (28 inches from the fixed end) was chosen for the location of the third actuator, and additional accelerometers will be located at positions 5 and 8. (Position 8 is located 49 inches from the fixed end.)

Table IV. Frequencies and Damping - Clean Configuration

Mode #	Frequency (Hz)	Damping (%)
1 (Z1)	2.03	.129
2 (Z2)	26.48	.375
3 (Z3)	69.57	.086
4 (T1)	13.50	Not Determined

Final Characterization

For the final modal analysis tests, the structure was put in its final configuration. The proof masses were returned to the actuators, the APS shaker was attached at position 5, the four response accelerometers were attached, and all wires and cables were tied down along the length of the beam. While performing the tests, all actuators were powered but uncommanded. Table V lists the frequency and damping ratios, and Figure 17 shows the mode shapes for the first three Z-axis bending modes. Both impact and random noise tests were used to generate these results. For the random noise tests, a rectangular measurement window was used, and 1000 overlapping averages were taken for each pair of input and response coordinates. Overall, a significant increase in damping and decrease in frequency is noted for the final configuration. Although most of the damping increase is due to actuator friction, the presence of the wires and cables on the beam also contribute to the final damping measurements. Also noticeable is a

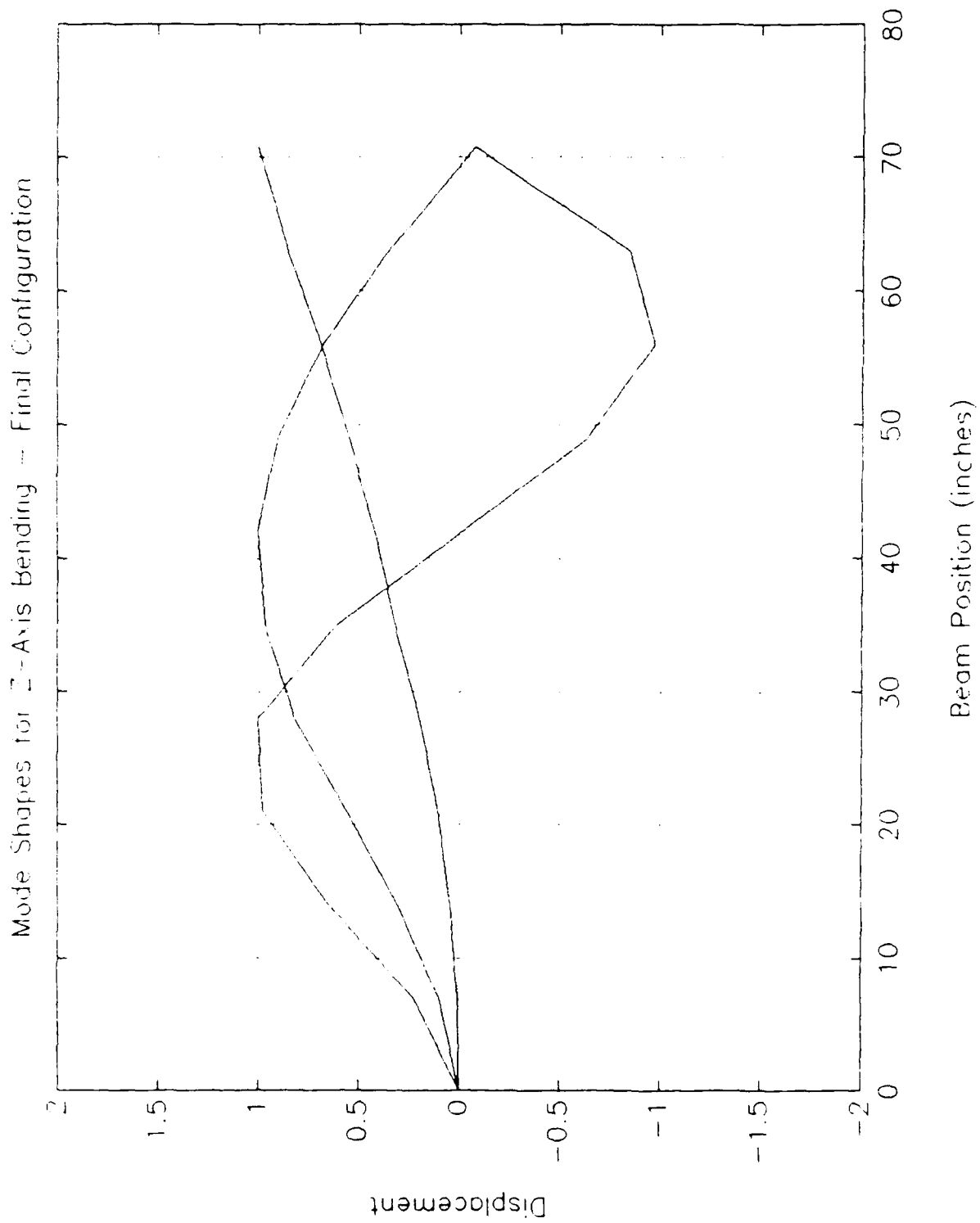


Figure 17. Mode Shapes for Z-Axis Bending - Final Configuration

decrease in the relative mode shape components (as compared to the clean configuration) in the vicinity of the shaker attachment point. The normalization of the mode shapes and the development of the model based on these final modal analysis tests will be discussed in Chapter V of this report.

Table V. Frequencies and Damping - Final Configuration

Mode #	Frequency (Hz)	Damping (%)
1 (Z1)	1.97	6.40
2 (Z2)	23.43	2.36
3 (Z3)	62.92	1.21
4 (T1)	13.35	0.839

IV. Sensors/Measurement Channels

Overview

The original ABE used the integrated output of piezoelectric accelerometers to provide velocity feedback for the controller. Although the integration process does a great job of filtering out high frequency noise, the output is very susceptible to drift caused by integrating dC offsets or very low frequency signals. The piezoelectric accelerometers aggravated the problem by providing a relatively poor low frequency response. One of the goals of the modified ABE was to improve upon the sensor/integration channels.

Accelerometers

The modified ABE uses Endevco Model 2262 piezoresistive accelerometers for measuring beam response. (Accelerometer specifications are listed in Appendix A.) These accelerometers have a good low frequency response, and can in fact provide static measurements. The signal conditioners (Endevco Model 4423) used in conjunction with the accelerometers include a zero adjustment such that the output of the accelerometers can be nulled prior to testing. Although the accelerometers and signal conditioners were calibrated across the entire bandwidth, in most cases a single calibration constant had to be chosen according to the frequency of interest for the particular test being conducted.

Integration Circuits

An ideal integration circuit for this experiment would provide perfect integration for signals above 1 Hz, and would reject all signals below this. Unfortunately, filters such as this can not be built; even filters which approach this ideal would have adverse phase shifts well above 1 Hz. In order to not affect the phase above 1 Hz (an ideal integrator

should have a constant phase lag of -90 degrees), the break frequency needs to be placed a full decade below this value.

The integrator used for the modified ABE experiment is shown in Figure 18. This circuit is based on a design provided by WRDC/FIBG. The predicted frequency response is shown in Figure 19. As shown, the circuit should provide "clean" integration above 1 Hz. At 2 Hz, (the first mode bending frequency), there is less than 1 degree of phase shift, and the slope of the magnitude is -20 dB/decade. Below .1 Hz, signals are increasingly attenuated with decreasing frequency, and the circuit should eliminate all dC signals. The one remaining problem with this circuit is the high gain in the low frequency region from .01 to 1 Hz, but this characteristic is unavoidable. The final stage op-amp for the circuit includes an offset null adjustment which provides a means for zeroing the entire measurement channel prior to testing.

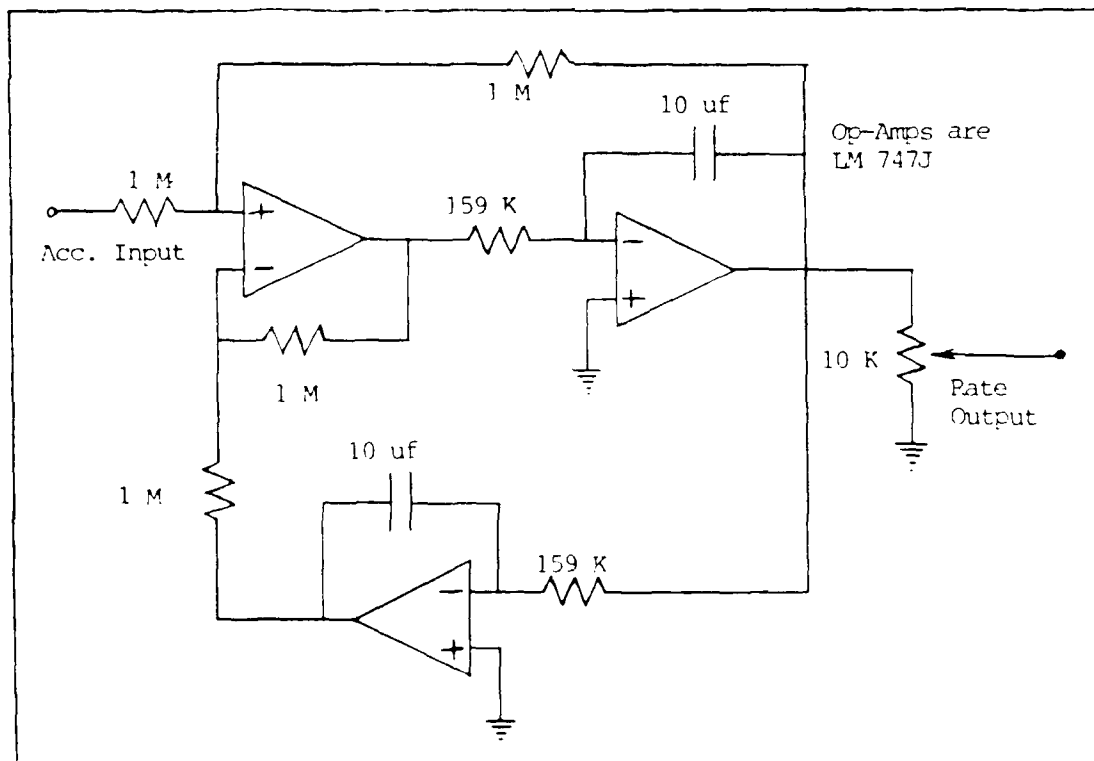


Figure 18. Integration Circuit Diagram

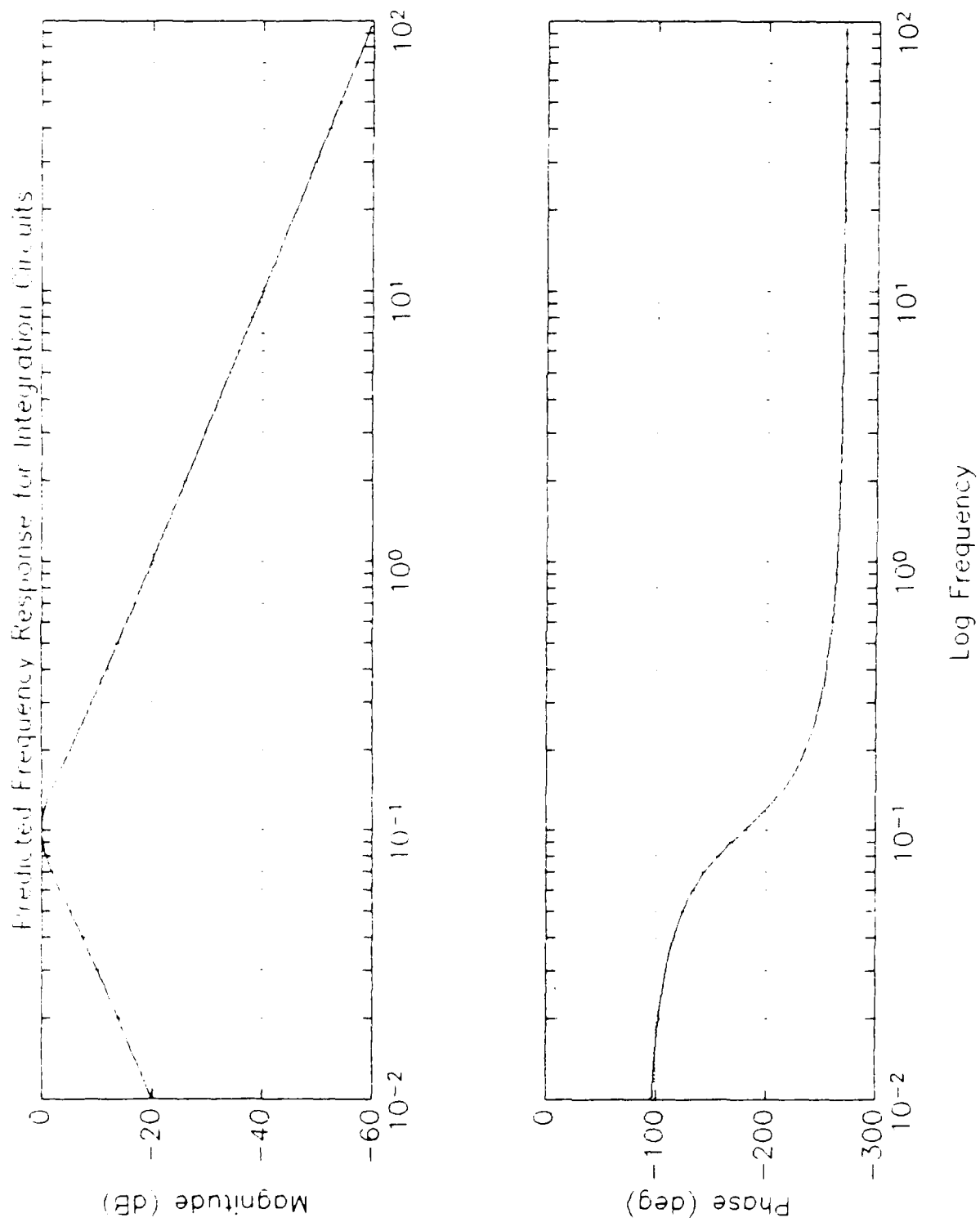


Figure 19. Predicted Integrator Frequency Response

Four integrators were constructed for the experiment, one for each measurement channel. Figure 20 shows the measured frequency response of one of the integrators. The integrator behaves as expected, with negligible phase shift and a straight -20 dB/decade magnitude slope above 1 Hz. The break frequency is not as sharp as predicted; this seems to be caused by variations and mismatching of the component values. The random noise generator on the B&K signal analyzer can not provide a flat noise spectrum down to dC, so the response below .1 Hz could not be measured accurately. (See Figure 21.) However, the trend does show decreasing magnitude with decreasing frequency below .1 Hz.

Final Measurement Channel

A side effect of the integration process is significant attenuation of the accelerometer signal. This required compensation in order to boost the signal amplitude to values close to the minimum full scale range of the input analog-digital converter on the controller. To accomplish this, two stages of amplification were used on each channel. (This is in addition to the amplification provided by the signal conditioners used with the accelerometers.) A block diagram for a single measurement channel is shown in Figure 22. The amplifiers are standard instrumentation amplifiers with selectable gain. A low pass filter on the amplifiers was set to 1 KHz. The first stage amplifier was placed before the integration circuit, while the second stage was placed after the integrators. Gain had to be kept low ($G_1=5$) in the first stage to avoid clipping the signals in the integrator. The remainder of the required gain was provided by the second stage ($G_2=20$).

The complete measurement channels (excluding the accelerometer and signal conditioner) were calibrated using the random noise tests with the B&K signal analyzer.

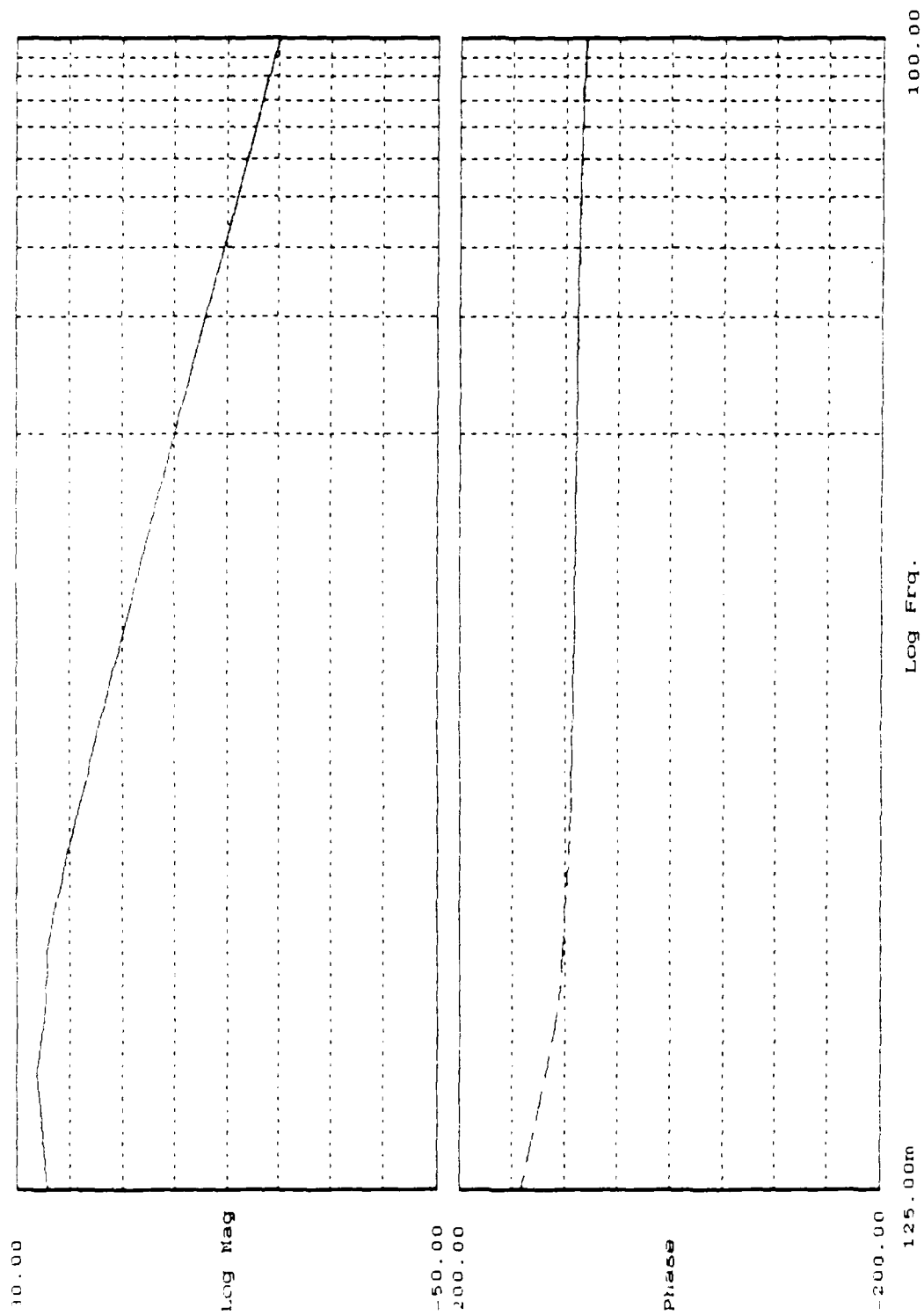


Figure 20. Measured Integrator Frequency Response

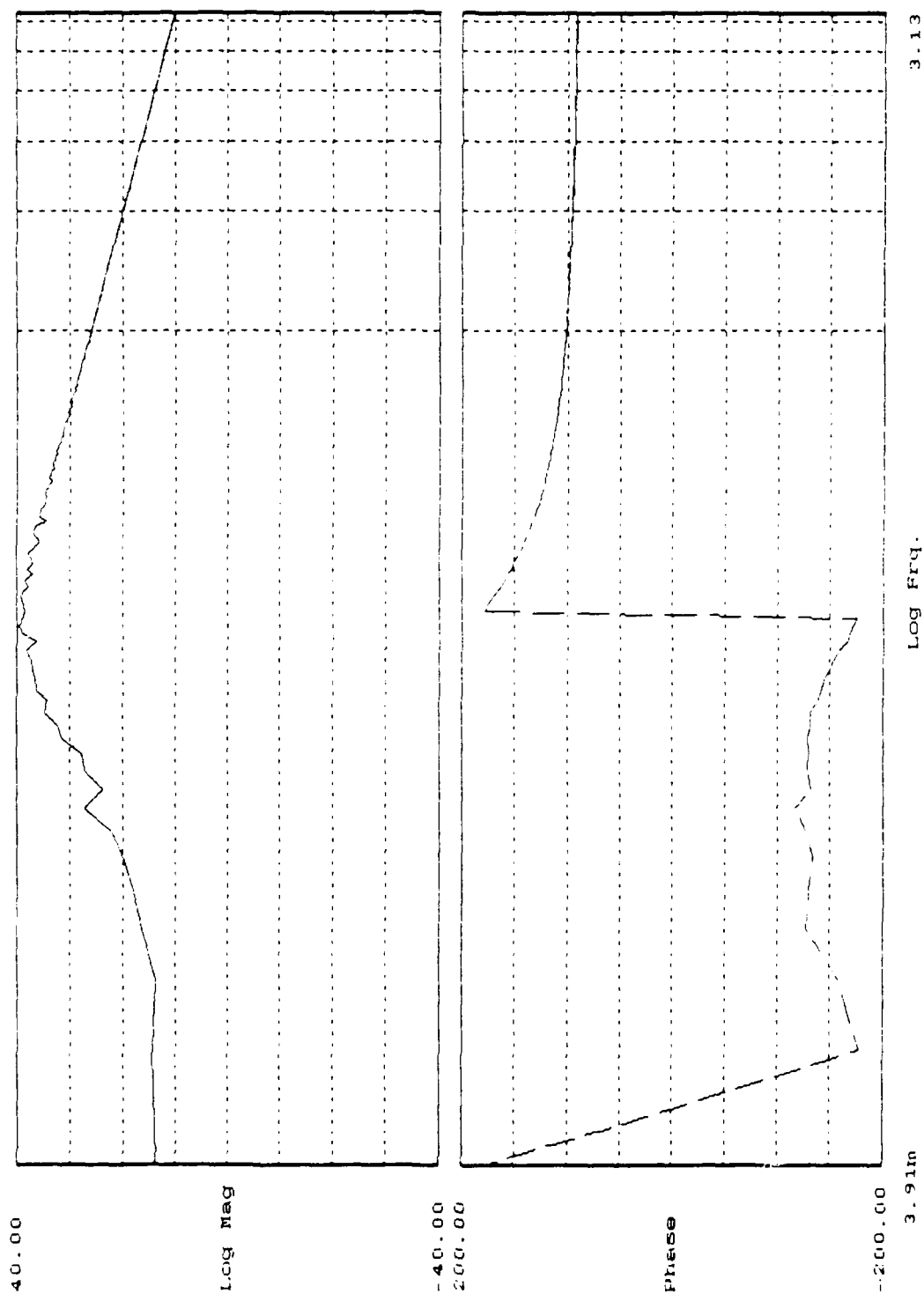


Figure 21. Integrator Frequency Response - Very Low Frequency

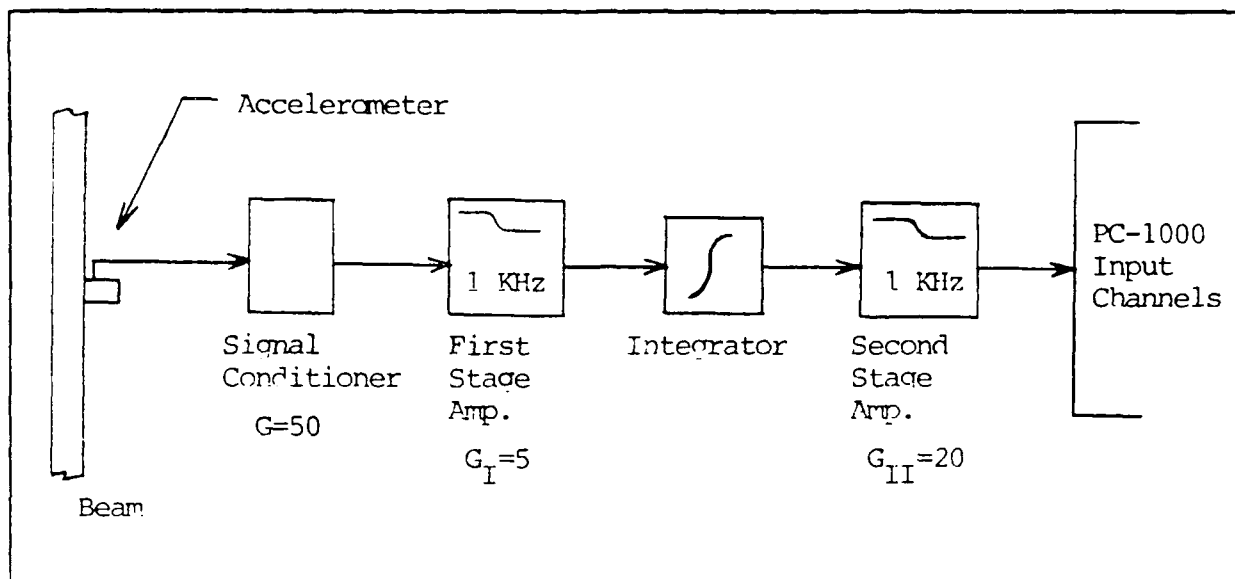


Figure 22. Measurement Channel Block Diagram

These calibration values (units of Volt-sec/Volt) were then multiplied by the accelerometer calibration values to obtain a final gain value for each channel. The calibrated gains for each of the measurement channels are listed in Table VI. These gains assume an average sensitivity across the control bandwidth. If desired, these gains could be optimized for a specific frequency by using the accelerometer sensitivity determined for that specific frequency.

The measurement channels corrected some, but not all of the problems experienced in the previous work done with the ABE. The piezoresistive accelerometers provide good response at the first mode frequency, and the integrators introduced less of a phase shift than those previously used. The dC cancellation of the integration circuit appears to work well; the entire measurement circuit can be zeroed prior to testing, and even intentional offsets introduced ahead of the integration circuit will be damped out after a

Table VI. Measurement Channel Gains

Channel #	Beam Position	Gain (Volts/in/sec)
1	5	.1449
2	8	.1646
3	11a	.1564
4	11b	.1329

slow oscillatory decay. The measurement channels still have problems with low frequency drift. Much of this seems to be caused by the amplifiers and could not be avoided. The instrumentation amplifiers were "salvaged" from storage and were known to have problems with drift. These amplifiers were the only ones available, and should be replaced if the ABE is to be used more in the future. The other more fundamental part of the drift problem is the limitation imposed by using accelerometers to measure low level, low frequency motion in a noisy environment. The integration process exaggerates the low frequency noise problem, and the amplification required by the integration process amplifies the noise along with the useful signal. An alternative method would be to use acceleration feedback directly, and let the state reconstruction routines provide modal velocity estimates for control purposes. Sensor designs for the space based control problem is, and will continue to be, one of the more technically challenging aspects of these systems.

V. System Configuration, Modelling, and Verification

System Overview

The hardware used in the modified ABE consists of an inverted cantilever beam with base plate, two linear proof mass actuators, a structural dynamics shaker, four response accelerometers, four integration/signal conditioning channels, the PC-1000 Array processor and its host computer, a modified Z-248 personal computer. (The reasoning for, and details of the Z-248 modifications are discussed in Appendix C.) Data collection was accomplished using the B&K signal analyzer and a DATAQ A/D board for the Z-248. The STAR Modal software package was used for frequency and damping measurements, and Mathworks' PC-MATLAB was used for modelling and simulation as well as control system design.

Figures 23 and 24 show the system in its final configuration. The shaker (Actuator C) is mounted 28 inches from the fixed end of the beam, providing good control over second and third mode bending about the Z-axis. The proof mass actuators (Actuators A and B) are mounted on the base plate parallel to the Y-axis. (See Figure 25.) The proof mass actuators can be operated symmetrically to provide control over Z-axis bending, and asymmetrically for control of the torsion mode. The arrows indicate positive direction for measurement or force input. A fourth actuator was provided for at location 8 in the final model, but there is no actuator physically located there. The fourth actuator was included in the model to enable simulations of a hammer impact at position 8. The accelerometers were arbitrarily numbered with #1 at position 5, #2 is at position 8, and #'s 3 and 4 are located at positions 11a and 11b respectively.

Figure 26 shows the component layout for the sensors, controller, actuators, and data acquisition devices. The integrated and amplified output of the accelerometers is fed

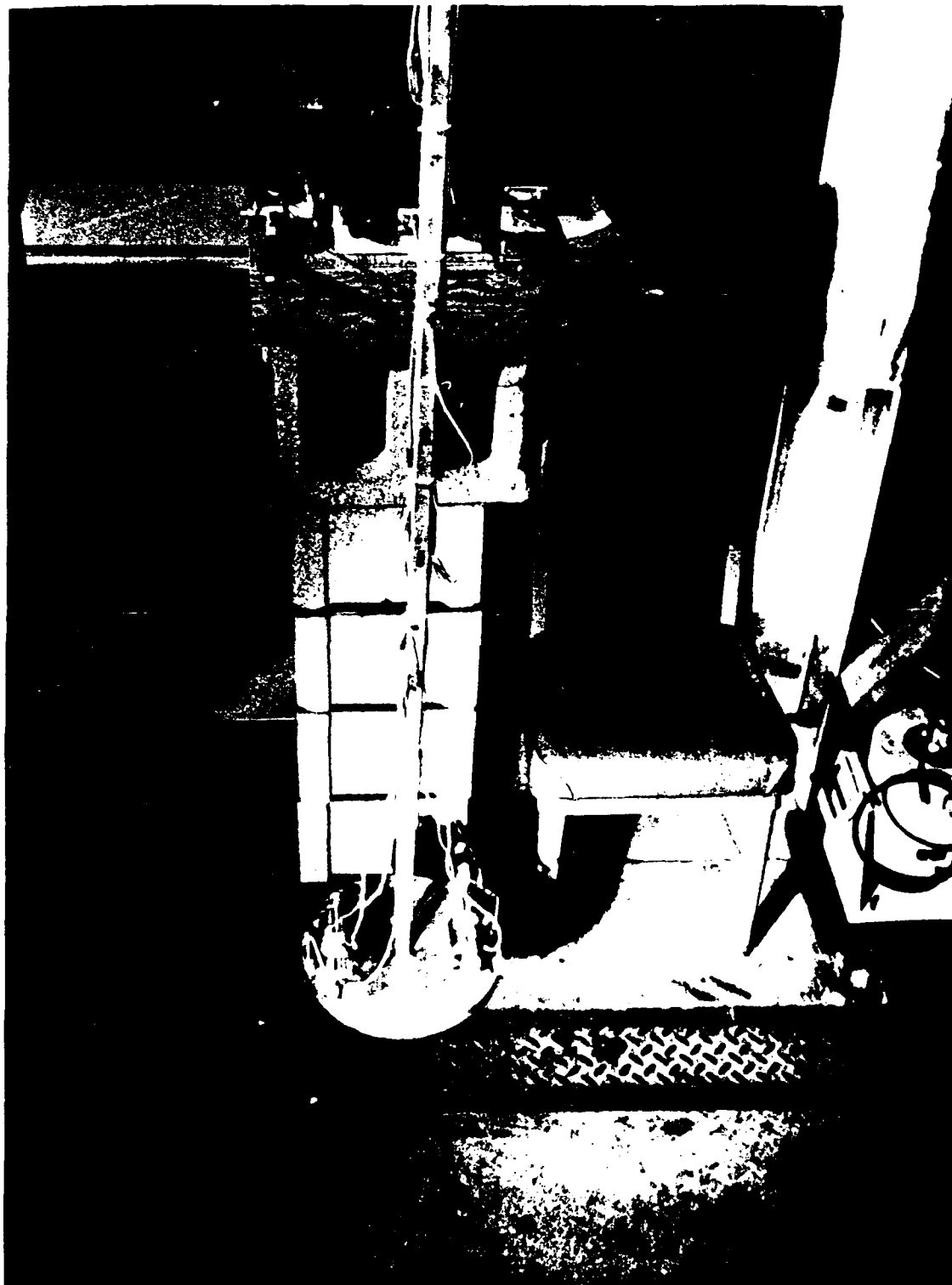


Figure 23. Advanced Beam Setup

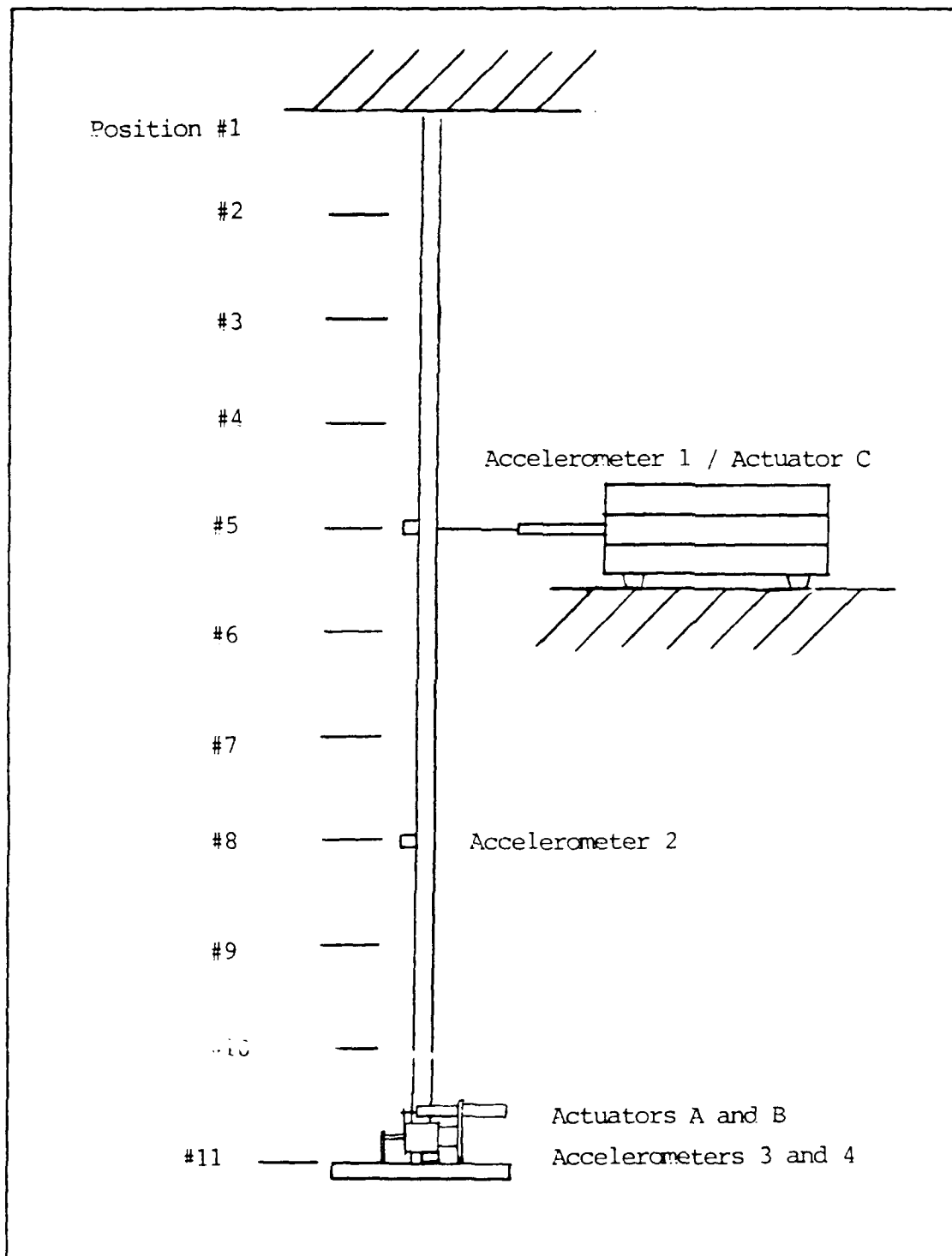


Figure 24. ABE Final Configuration

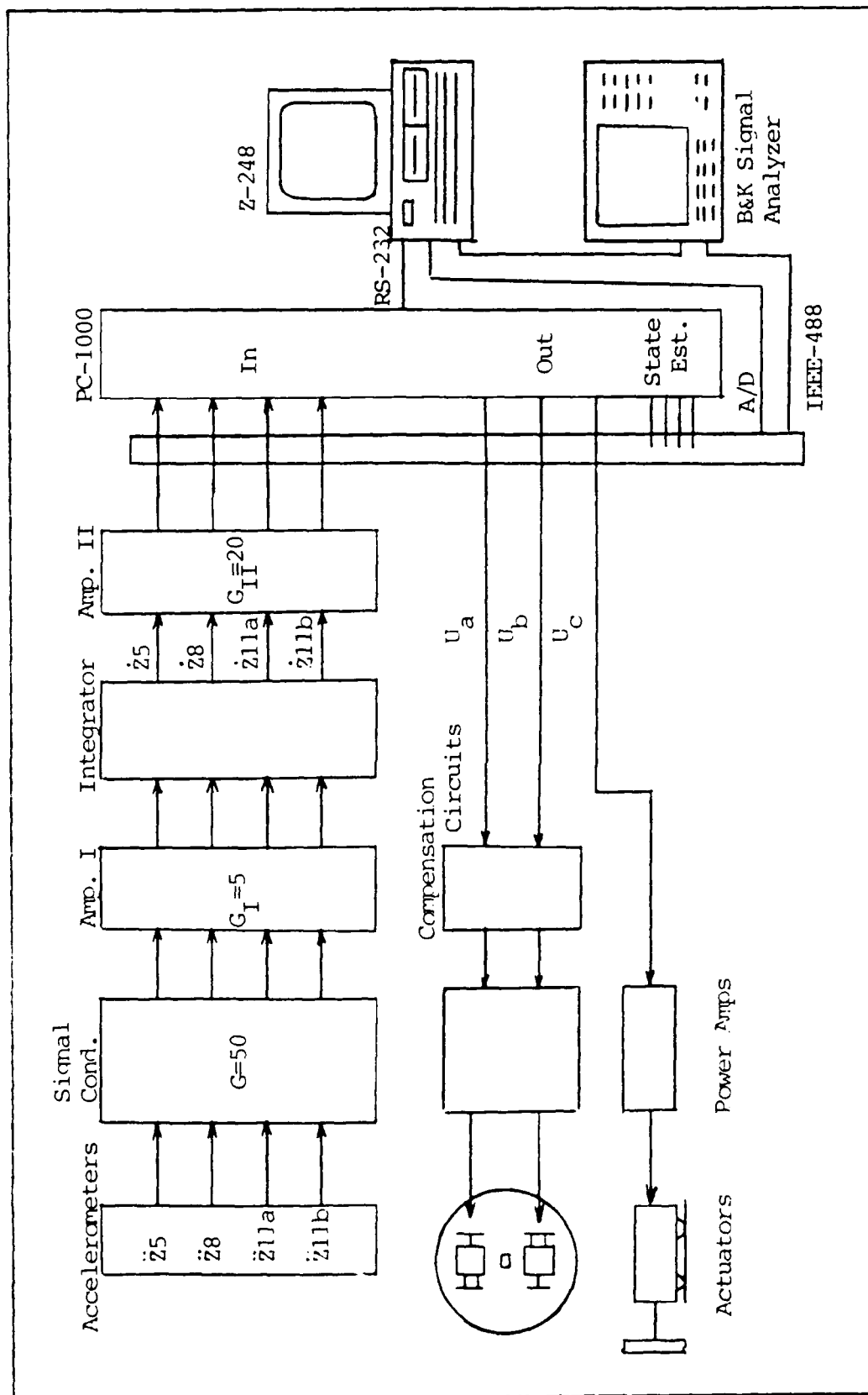


Figure 26. ABE Block Diagram

into the PC-1000 which acts as the state estimator and controller. The PC-1000 is a high speed programmable digital array processor, which has 12 bit A/D converters on the input channels and 12 bit D/A converters on the output channels. Internal calculations are performed using 32 bit floating point arithmetic. The PC-1000 can be programmed for various sampling rates (up to 2000 Hz), input and output gains, and estimation and control algorithms. For this project, the sampling rate was set for 2000 Hz, the input gains were set to the reciprocal of the measurement channel gain, and the output gains were set to the reciprocal of the actuator gains. (Further information on the operation and capabilities of the PC-1000 can be found in Reference 13.) The outputs of the PC-1000 consist of control signals for the actuators and estimates of the modal states. All of the inputs and outputs of the PC-1000 are available for measurement with either the signal analyzer or the A/D data acquisition board on the computer.

Model Development

The model for the system is based on the final modal analysis data, and the assumption that only the first three Z-axis bending modes and the first torsion mode would be present in any response. Y-axis bending and all higher frequency modes were neglected. Although the beam is free to move in the Z direction (Y-axis bending), care will be taken not to inadvertently excite these modes. The higher frequency modes will exhibit very low amplitudes (partially as a result of higher damping), and measurements of these modes will be increasingly attenuated by the integration process. Although the higher frequency modes could be included in the measurement and state estimation model, they could not be controlled on the existing system because they lie outside the control bandwidth. The model will also assume no coupling of the modes, and the same assumptions stated in Chapter III for the modal analysis process apply to the model.

The frequencies and damping used for the final model are listed in Table III, which appeared in Chapter III of this report.

For the ABE structure with control inputs, the equations of motion can be written as

$$M\ddot{\underline{q}} + C\dot{\underline{q}} + K\underline{q} = D\underline{u} \quad (22)$$

where \underline{q} is a 4-vector of generalized coordinates, M is a 4x4 symmetric mass matrix, C is a 4x4 damping matrix, and K is a 4x4 stiffness matrix. For a system obeying the assumptions stated above, equation 22 can be decoupled using modal coordinates $\underline{\eta}$ and the modal matrix of right eigenvectors Φ to define a transformation such that

$$\underline{q} = \Phi \underline{\eta} \quad (23)$$

The matrix Φ actually contains components of the mode shapes which can be normalized such that

$$\Phi^T M \Phi = I \quad (24)$$

If Φ is normalized in this manner, equation 22 can be transformed into

$$\ddot{\underline{\eta}} + [2\zeta\omega]\dot{\underline{\eta}} + [\omega^2]\underline{\eta} = \Phi^T D \underline{u} \quad (25)$$

The matrix $[2\zeta\omega]$ represents a diagonal matrix with the individual elements $2\zeta_i\omega_i$ representing the damping for the i^{th} mode, and $[\omega^2]$ is a 4x4 diagonal matrix of the eigenvalues of equation 22. The above transformation requires mode shapes which have

been normalized with respect to the mass matrix, which can not be directly measured. A normalization procedure was developed for this purpose, and it provided a way to base the model entirely on the open loop measurements. However, before describing the normalization procedure, it is necessary to define the generalized coordinates used for the model.

Table VII lists the generalized coordinates and their relationship to physical coordinates. The only constraint on the selection of generalized coordinates is that they must be of sufficient number, (in this case, 4), and they must be linearly independent. For this model the choice was made for ease of understanding, measurement, and the method used for normalization of the mode shapes. Note that q_4 , which is a torque displacement, shows units of inches. Because q_4 represents a differential displacement at a known radius, it does in fact represent a torque measurement.

Table VII. Generalized Coordinates

Generalized Coord.	Measured Coord.	Units
q_1	Z5	in
q_2	Z8	in
q_3	$0.5 (Z11a-Z11b)^*$	in
q_4	$0.5 (Z11a+Z11b)^*$	in

* See Figure 25 for orientation of base plate accelerometers.

For the ABE system we can look at the response of mode i to a shaker force input at position 5,

$$\ddot{\eta}_i + 2\omega_i\dot{\eta}_i + \omega_i^2\eta_i = \phi_{5,i}K_i u \quad (26)$$

The control input has been broken down into command voltage (u_c) and shaker gain (K_s). If the shaker is driven at a mode i resonant frequency, equation 26 yields

$$\frac{\eta_i}{u_c} = \frac{\phi_{s,i} K_s}{2\zeta_i \omega_i^2} \quad (27)$$

The response of the beam at position 5 has the form

$$z_5 \approx q_i = \phi_{s,i} \eta_i + \phi_{s,2} \eta_2 + \phi_{s,3} \eta_3 \quad (28)$$

If the beam is being driven at mode i resonance, and there are no coupled modes involved, it can be safely assumed that only one mode of vibration is present in the response;

$$q_i = \phi_{s,i} \eta_i \quad (29)$$

With a driving point measurement at position 5, the ratio

$$\frac{\ddot{q}_i}{u_c} = \frac{\phi_{s,i}^2 K_s}{2\zeta_i} \quad (30)$$

can be measured with the signal analyzer. From this equation, the normalized mode shape can be solved for in terms of the measurement.

$$\phi_{s,i} = \left[\frac{2\zeta_i}{K_s} \left(\frac{\ddot{q}_i}{u_c} \right) \right]^{1/2} \quad (31)$$

Once a single component of the mode shape has been normalized using this method, the remaining mode shape components can be scaled accordingly. This procedure normalizes with respect to the mass matrix without having to solve for the modal masses. Figure 27 shows the normalized mode shapes for the Z-axis bending modes. A similar procedure was used to normalize the torque mode shape component, with the exception that the proof mass actuators were used to make the driving point measurement. Only the component of the mode shape at position 11 (the base plate) is required for the torque mode.

Equation 25 can be formulated in the standard state space form of

$$\dot{\underline{x}} = A\underline{x} + B\underline{u} \quad (32)$$

where the state vector \underline{x} is defined as an 8-vector composed of \underline{q} and $\dot{\underline{q}}$, and A and B have the form

$$A = \begin{bmatrix} 0 & I \\ -\omega^2 & -2\zeta\omega \end{bmatrix} \quad (33)$$

$$B^T = [0 \mid D^T\Phi] \quad (34)$$

In general, the states of a structure can not be measured directly; often the actual measurements can be described as linear combinations of the states

$$\underline{y} = C\underline{x} \quad (35)$$

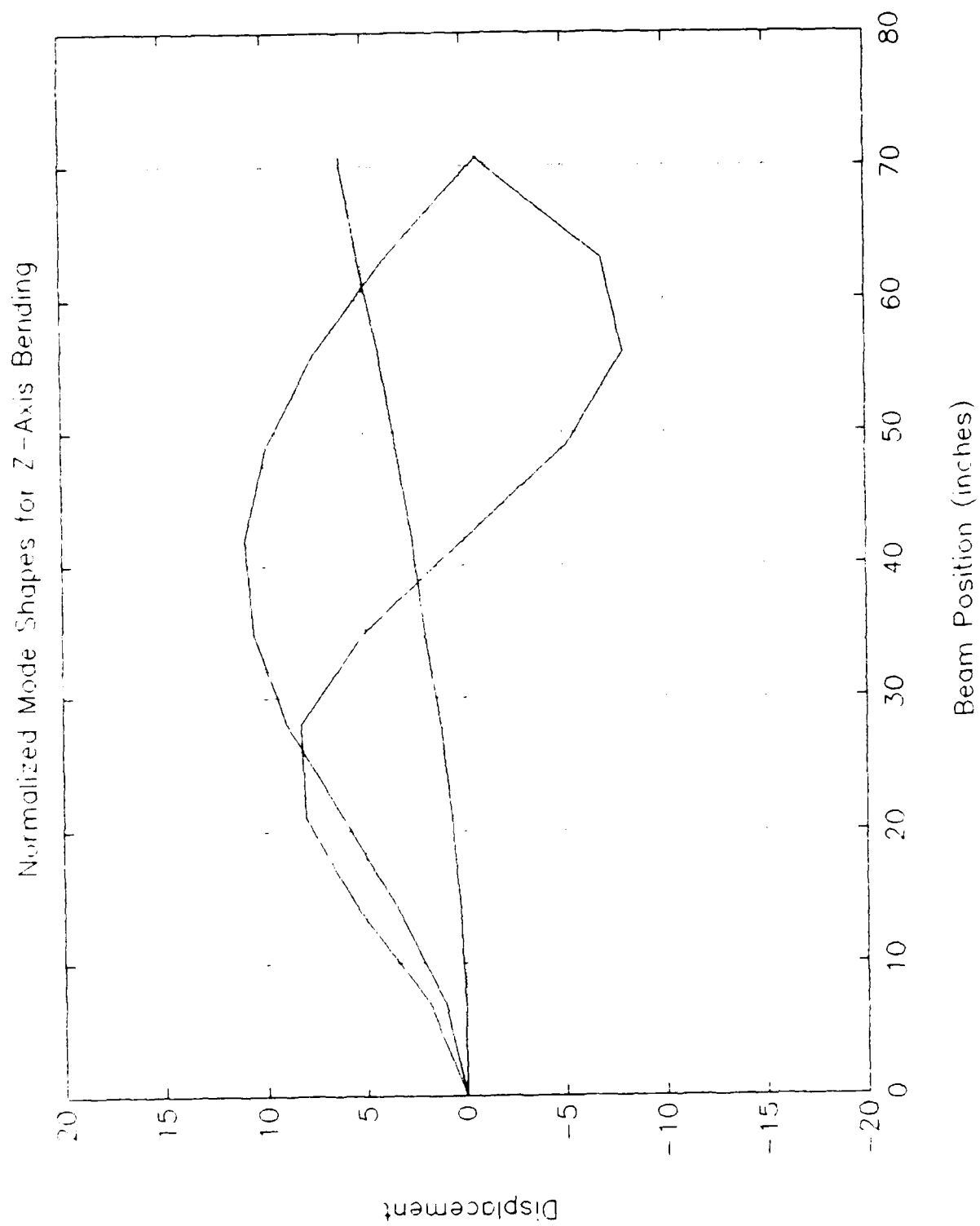


Figure 27. Normalized Mode Shapes for Z-Axis Bending

Table VIII lists the output variables and their relationships to the generalized and physical coordinates. For this experiment, y is a 4-vector and C is a 4x8 matrix which can be partitioned into

$$C = [C_p \Phi \mid C_v \Phi] \quad (36)$$

where the partitions C_p and C_v are the coefficients for position and velocity sensors, respectively. Since position feedback is not being used in this system, $C_p=0$. The final state model for the modified ABE is summarized in Appendix B.

Table VIII. Output Variable Relationships

Output Variable	Generalized Coord.	Physical Coord.
y_1	\dot{q}_1	\dot{Z}_5
y_2	\dot{q}_2	\dot{Z}_8
y_3	$+\dot{q}_3 + \dot{q}_4$	\dot{Z}_{11a}
y_4	$-\dot{q}_3 + \dot{q}_4$	\dot{Z}_{11b}

Model Verification

For the model to be valid, it must accurately predict the response of the beam to a given input, providing the input does not violate the assumptions on which the model is based. It should also provide accurate predictions of the closed loop system behavior; i.e. with the controller and actuators engaged. In order to test the validity of the model, simulated responses were compared to measured responses to known inputs. These tests included open loop beam response tests, and both analog and digital velocity feedback tests. The simulations were performed using PC-MATLAB, an interactive matrix

manipulation, signal processing and controls software package. The closed loop eigenvalues of the model were used to predict damping levels for the velocity feedback tests.

The model was developed using open loop beam response measurements; therefore, one would expect that the measured open loop response would compare closely with that predicted by the model. However, the model assumes only three bending modes are present, while the actual beam has an infinite number of higher frequency modes. An open loop comparison of the time responses was needed to insure that the high frequency modes neglected in the model are not a significant part of the response of the actual beam. Figure 28 shows the predicted impulse response and measured response to an impact with an eraser tipped hammer. All measurements and force inputs were at position 5 on the beam. (The amplitude of the simulated response was scaled to match the measured response, no attempt was made to simulate the physical impact.) As shown, the form of the responses match closely. The initial difference between the responses is due to the difference between an ideal impulse and a physical impact with an eraser tipped hammer. There is no significant presence of higher frequency modes in the measured response, thus validating the three bending mode assumption for the ABE model. A similar test was also carried out for the open loop torque response.

Prior to incorporating the PC-1000 into the system, an analog feedback test was carried out. This test used feedback of position 5 velocity to the shaker. The gains for the velocity measurement channel and actuator C were combined in order to determine a feedback gain for the simulation. For a velocity feedback gain of .708, the predicted and measured damping levels are listed in Table IX. Predicted damping levels closely matched the levels measured using the STAR Modal software. The log decrement method could not be used to check the damping measurements because the response was

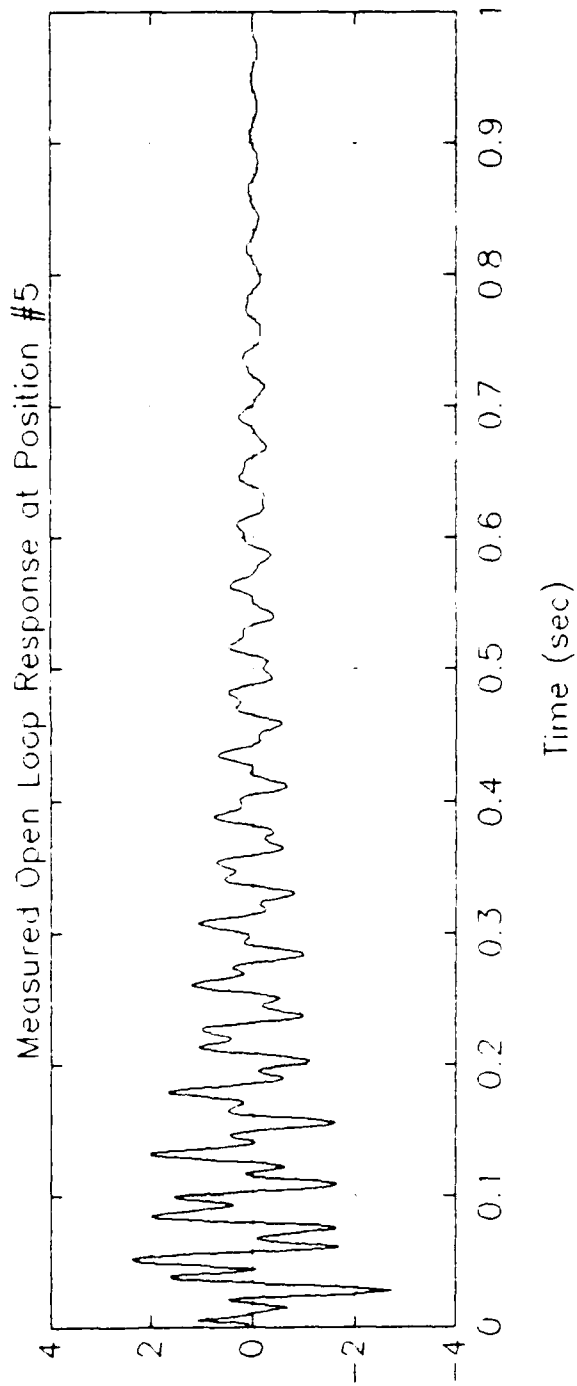
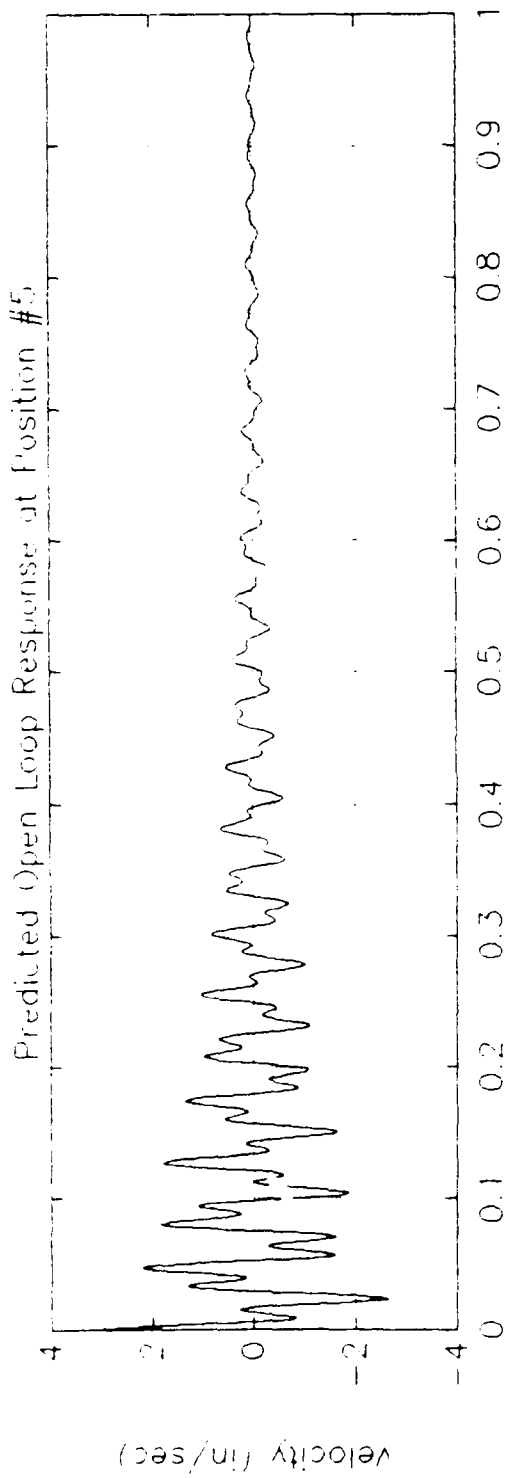


Figure 28. Predicted and Measured Open Loop Response

composed of three different modes, each with its own damping ratio. Mode 1 damping was not measured during this test because of the relatively small participation of mode 1 in the position 5 response. This test reinforced confidence in the model, and validated the gains for the sensors and shaker (Actuator C) channel.

Table IX. Results of Position 5 Velocity Feedback Tests

Mode #	Predicted Damping (%)	Measured Damping (%)
2 (Z2)	21.8	21.9 \pm .5
3 (Z3)	7.2	7.3 \pm .5

A simple analog feedback test could not be performed using the proof mass actuators because the mounting configuration required equal output forces from both actuators, when in fact the gains of actuators A and B were significantly different. A simple digital feedback test was designed using the PC-1000 which provided a simple means for gain equalization and signal inversion when necessary. Originally, the test plan called for first mode bending and torque response tests using only the proof mass actuators as control inputs. Velocity feedback for the first mode bending test was to consist of the differential output of sensors 3 and 4, while feedback for the torsion test would consist of a sum of the outputs. The first mode bending test could not be conducted because of the nature of the signals being used to drive the actuators. By the time the unfiltered differential output of the sensors made it through the PC-1000, the drift and noise was severe enough to cause the proof mass actuators to continually wander into their stops. The state estimation and filtering process used in the later controllers should solve most of the drift and noise problem; therefore, it was decided to go on with the testing without further modification to the system.

The torque response test also had problems with actuator drift, but not nearly as severe as that experienced while differencing the sensor outputs. The measurements could be taken, but the centering of the actuators had to be adjusted after each impact and measurement. The predicted damping level for this test was 11.4%, while the measured value was 9% (as compared to 0.84% for the open loop response). While this test did not demonstrate impressively accurate predictions by the model, the prediction was not too far off for the model to be considered bad. Much of the error can be attributed to sensor noise finding its way into the actuator circuits; no attempt was made to prevent this from happening in this test. A filtering process prior to feeding measurements back to the proof mass actuators should improve their behavior and provide a more predictable response. Having said this, the model was considered valid pending the results from the full-up estimator/controller tests.

VI. Closed Loop Digital Control

Optimal Control Methods

The state space model for the ABE system was developed in the previous chapter. The resulting equation, repeated here, are

$$\dot{\underline{x}} = A\underline{x} + B\underline{u} \quad (37)$$

$$\underline{y} = C\underline{x} \quad (38)$$

where \underline{x} contains the modal amplitudes and velocities, \underline{u} contains the control inputs, and \underline{y} contains the sensor outputs. The values for the constant gain matrices A, B, and C are contained in Appendix B.

If full state feedback is used, the control input can be defined as linear combinations of the state variables

$$\underline{u} = -G\underline{x} \quad (39)$$

Generally, as is the case for this system, the state variables can not be measured directly. For this reason, an estimator is required to reconstruct the states from the sensor outputs and the system model. The estimator has the form

$$\dot{\hat{\underline{x}}} = A\hat{\underline{x}} + B\underline{u} + K(\underline{y} - \hat{\underline{y}}) \quad (40)$$

$$\hat{\underline{y}} = C\hat{\underline{x}} \quad (41)$$

where $\hat{\underline{x}}$ is the estimated state vector, and \hat{y} is the estimated output. The observer gain K must be chosen such that the error in the state estimate defined by

$$\underline{e} = \hat{\underline{x}} - \underline{x} \quad (42)$$

is stable. As stated earlier, the actual state vector is not available; therefore, the control input must be based on the estimate of the state vector

$$\underline{u} = -G\hat{\underline{x}} \quad (43)$$

Equations 40 and 41 can be combined to provide

$$\dot{\hat{\underline{x}}} = (A - BG - KC)\hat{\underline{x}} + K\hat{y} \quad (44)$$

which, together with equation 43 are the governing equations for the estimator controller to be implemented on the PC-1000.

There are many methods for selecting the estimator gain matrix K , and the control gain matrix G . If the statistics of the measurement noise and model uncertainties are available, a cost functional can be defined for the estimator

$$J_o = \int_0^{\infty} (\hat{\underline{x}}^T Q_o \hat{\underline{x}} + \hat{y}^T R_o \hat{y}) dt \quad (45)$$

where Q_o represents the process noise covariance, and R_o represents the measurement noise covariance. For an observable system, a K matrix can be selected which

minimizes the quadratic cost functional, and this is the basis of a Kalman filter.

A quadratic cost functional can also be defined for the controller

$$J_c = \int_0^{\infty} (\underline{x}^T Q_c \underline{x} + \underline{u}^T R_c \underline{u}) dt \quad (46)$$

where Q_c is a state weighting matrix, and R_c serves as a control usage penalty matrix. For full state feedback on a controllable system, a G can be determined which minimizes this cost functional. This is known as a Linear Quadratic Regulator (LQR). The combination of a Kalman filter and LQR is referred to as a Linear Quadratic Gaussian (LQG) compensator.

Time constraints precluded the complete characterization of the process and measurement noise statistics for the ABE system. For this reason a "true" LQG compensator was not implemented. The same cost functional was used to derive the estimator gain K , but Q_e and R_e were merely chosen such that the resulting estimator damping (determined from the eigenvalues of $[A - KC]$) was 20-30% for all states. Relative estimates of the noise covariance were used to determine a K which met this criteria. The 20-30% damping for the estimator was taken from previous work on the ABE.(8) This damping level provided smooth actuator commands without relatively long time delays to damp out errors between the estimates and the measurements. Higher damping seemed to cause excessive drift in the estimates, and significantly lower damping allowed excessive error to build up. The controller gain matrix G was selected based on the specific type of control being demonstrated.

Optimal Control Design #1

The first controller was designed using LQR theory. Only states 2 (Z2) and 4 (T1) were weighted, and care was taken to insure that the control gains were kept relatively low. A high penalty was placed on input 4, reflecting the fact that there is actually no fourth actuator; its presence in the model is only to allow for simulating impacts at position 8. The resulting gain matrix divided the responsibility for controlling mode 2 between the shaker and the proof mass actuators, while the torque mode can only be controlled by the proof mass actuators.

In order to implement the estimator and control algorithms on the PC-1000, the equations need to be converted to an equivalent discrete time form. The discrete time equivalent of equations 43 and 44 are

$$\hat{\underline{x}}_{k+1} = \exp(A_{\infty}\delta t)\hat{\underline{x}}_k + A_{\infty}^{-1}[\exp(A_{\infty}\delta t) - I] K \underline{y}_k \quad (47)$$

$$\underline{u} = -G\hat{\underline{x}}_k \quad (48)$$

where δt is defined by the reciprocal of the sampling rate, and

$$A_{\infty} = [A - BG - KC] \quad (49)$$

The computational format of the PC-1000 is

$$[\underline{u}_{k+1} \mid \hat{\underline{x}}_{k+1}]^T = \begin{bmatrix} F_{11} & F_{12} \\ F_{21} & F_{22} \end{bmatrix} \begin{bmatrix} \underline{y}_k \\ \hat{\underline{x}}_k \end{bmatrix} \quad (50)$$

where the dimensions of the partitions are: F_{11} : 16x16, F_{12} : 16x32, F_{21} : 32x16, and F_{22} : 32x32. Putting equations 47 and 48 into this form defines the partitions as

$$F_{11} = 0 \quad (51)$$

$$F_{12} = -G \quad (52)$$

$$F_{21} = A_{\infty}^{-1}[\exp(A_{\infty}\delta t) - I] K \quad (53)$$

$$F_{22} = \exp(A_{\infty}\delta t) \quad (54)$$

PC-MATLAB was used to calculate the partitions F_{21} and F_{22} .

Table X lists the predicted and measured damping levels for all four modes. As predicted, modes 1 and 3 were mostly unaffected. The mode 2 damping level was not predicted with the same accuracy as was achieved in the analog feedback test, but the analog test used only the shaker (the most predictable of the three actuators) for control input. The smoother actuator command signals provided by the estimator greatly improved the behavior of the proof mass actuators (as was hoped), and the result is that mode 4 damping was much more predictable than it was previously for the gain verification tests.

Time plots were obtained for an impact and measurement at position 5, and these are shown in Figure 29. The predicted response was generated by a simulated (and scaled) impulse response at the same position. Beyond the initial differences due to the nature of the inputs (ideal impulse vs eraser tipped impact), the time responses show good

Table X. Optimal Control Design #1 Results

Mode #	Predicted Damping (%)	Measured Damping (%)
1 (Z1)	6.4	6 - 7
2 (Z2)	5.9	5.3 ± .3
3 (Z3)	1.2	1.3 ± .1
4 (T1)	3.7	3.6 ± .2

agreement. Figure 30 shows the affect of the controller on the torque mode. The torque mode was excited by impacting at the edge of the base plate in the Z direction. This caused no measurable Z-axis bending. Because the sensors were mounted in the Y direction, the resulting Y-axis bending did not show up in the measurements, (providing displacements were small), and the resulting measurements showed a clean torque response. Together with the model verification discussed in Chapter V, the results of the first controller design inspired confidence in the model development process.

Optimal Control Design #2

The second controller design used the same estimator as the first, but the control gain matrix was selected such that mode 2 was assigned exclusively to actuator C, and mode 4 would again be controlled by actuators A and B. Instead of minimizing a quadratic cost functional, the gains for the controller were assigned according to

$$u_A = u_B = -\underline{\hat{x}}_4 \quad (55)$$

$$u_C = 10\underline{\hat{x}}_2 \quad (56)$$

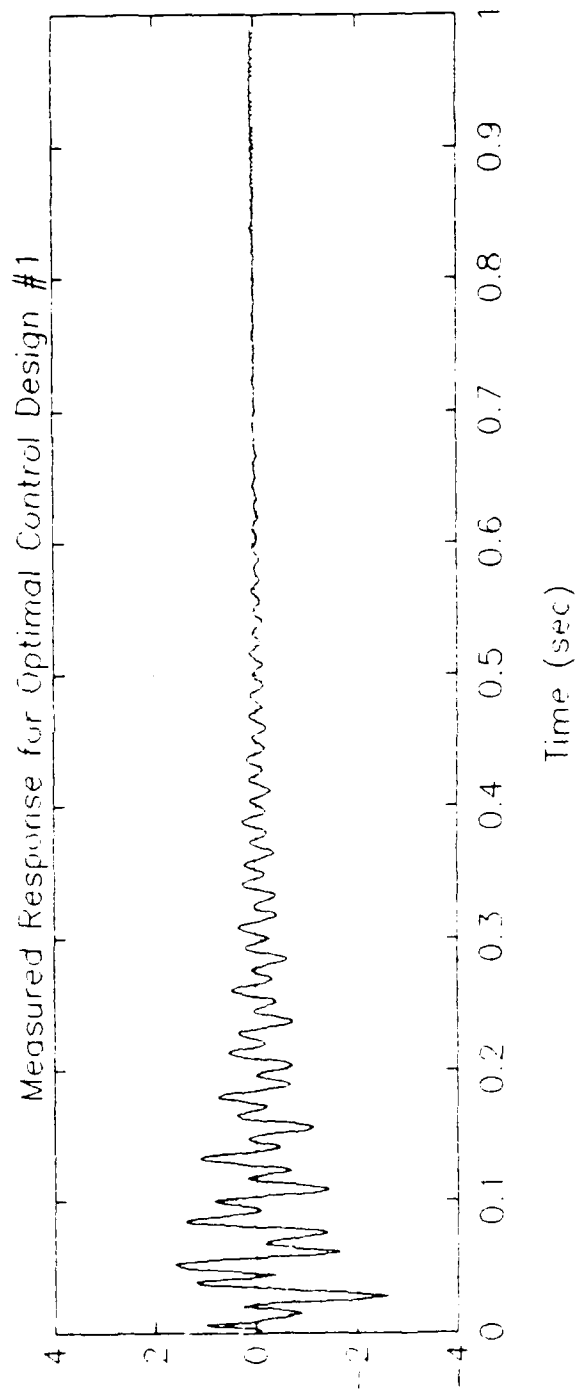
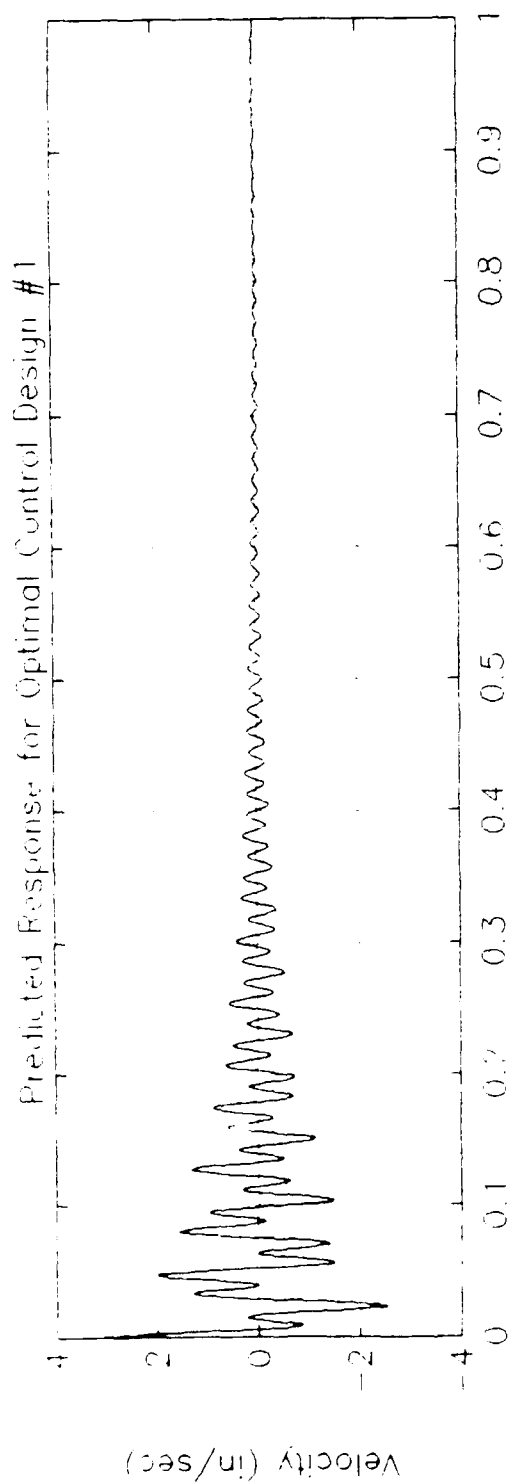


Figure 29. Optimal Control Design #1, Position 5 Response

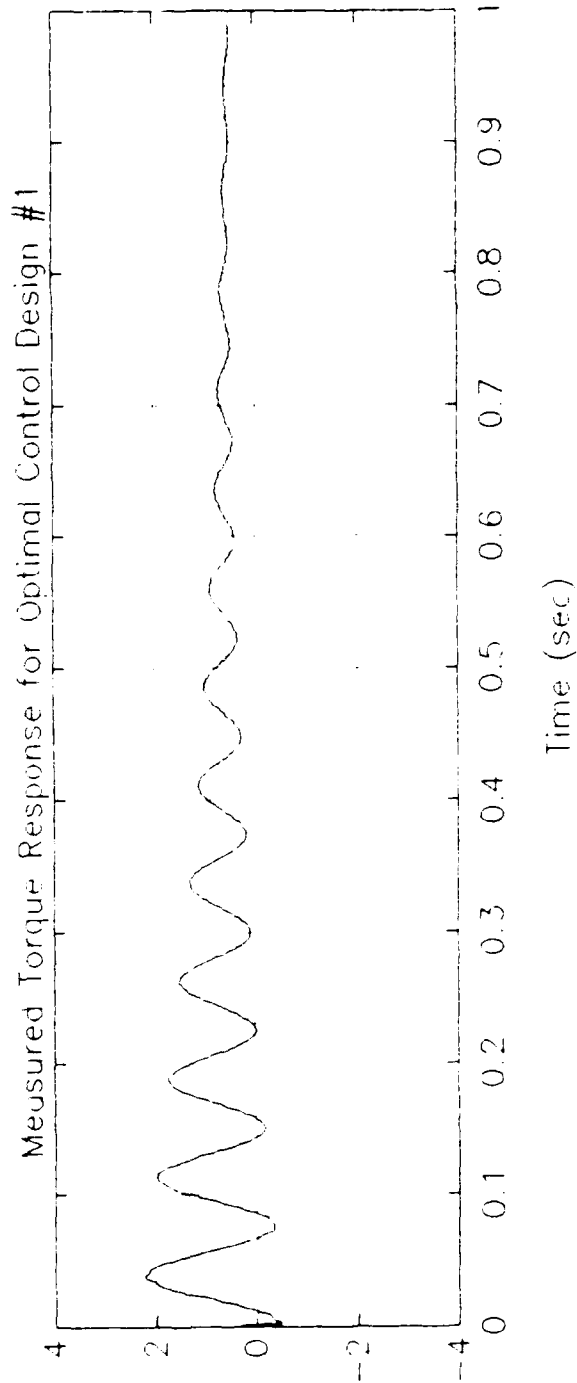
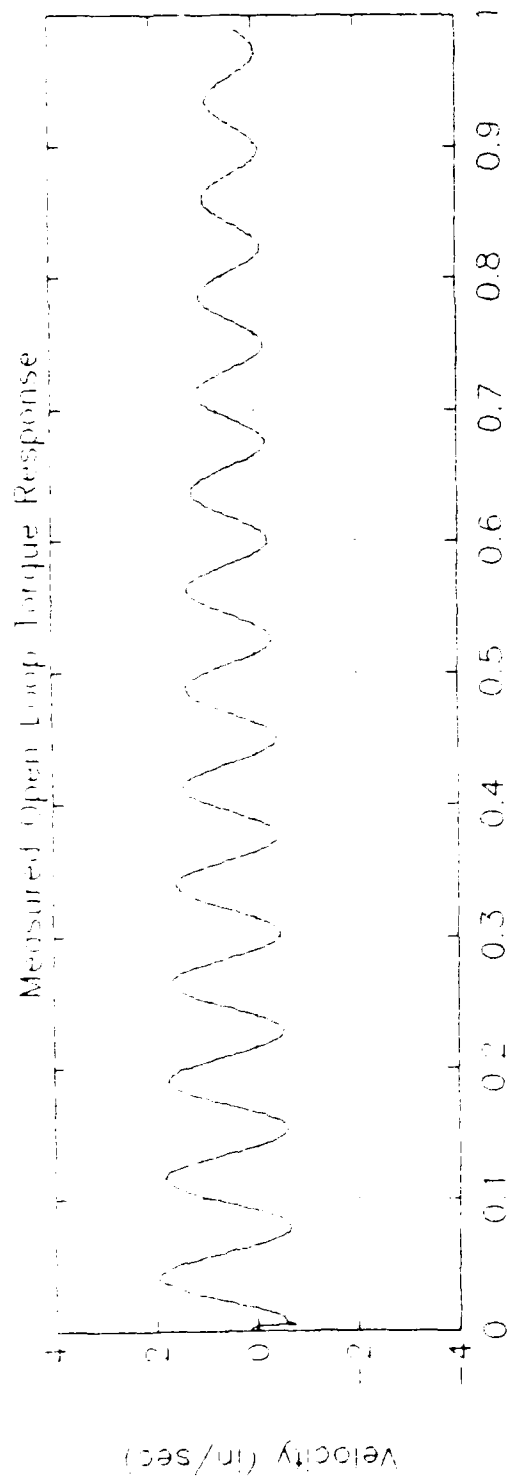


Figure 30. Optimal Control Design #1, Torque Response

Although not obvious from the equations, these gains are significantly higher than those used in the first controller design. (Less than half this amount of control force was used for control of mode 4 in design #1, and less than one fifth this amount was used for control of mode 2.) Once again, the controller was told to leave modes 1 and 3 alone.

Table XI lists the predicted and measured damping levels with the second controller engaged. With the exception of a larger than expected increase in mode 3 damping, the model accurately predicted the measured results. The discrepancies in mode 3 damping levels may have been caused by drift in the estimator which was known to occur. Time responses at position 5 are shown in Figure 31. The effect of mode 2 cancellation is clearly evident in the time responses, and the predicted response closely resembles the measured response. Figure 32 shows the effect of the controller on the torque response.

Table XI. Optimal Control Design #2 Results

Mode #	Predicted Damping (%)	Measured Damping (%)
1 (Z1)	7.0	6 - 7
2 (Z2)	20.3	20.4 \pm .3
3 (Z3)	1.2	1.6 \pm .2
4 (T1)	6.9	7.0 \pm .2

Estimate Inadequacies

As described above, the estimator and controllers provided predictable results when controlling modes 2 and 4. An optimal control design demonstrating control over mode 3 was attempted, but the results were very unpredictable. After a significant amount of troubleshooting, the culprit was found to be the estimator which was implemented with the controllers. The weighting matrices for the estimator were

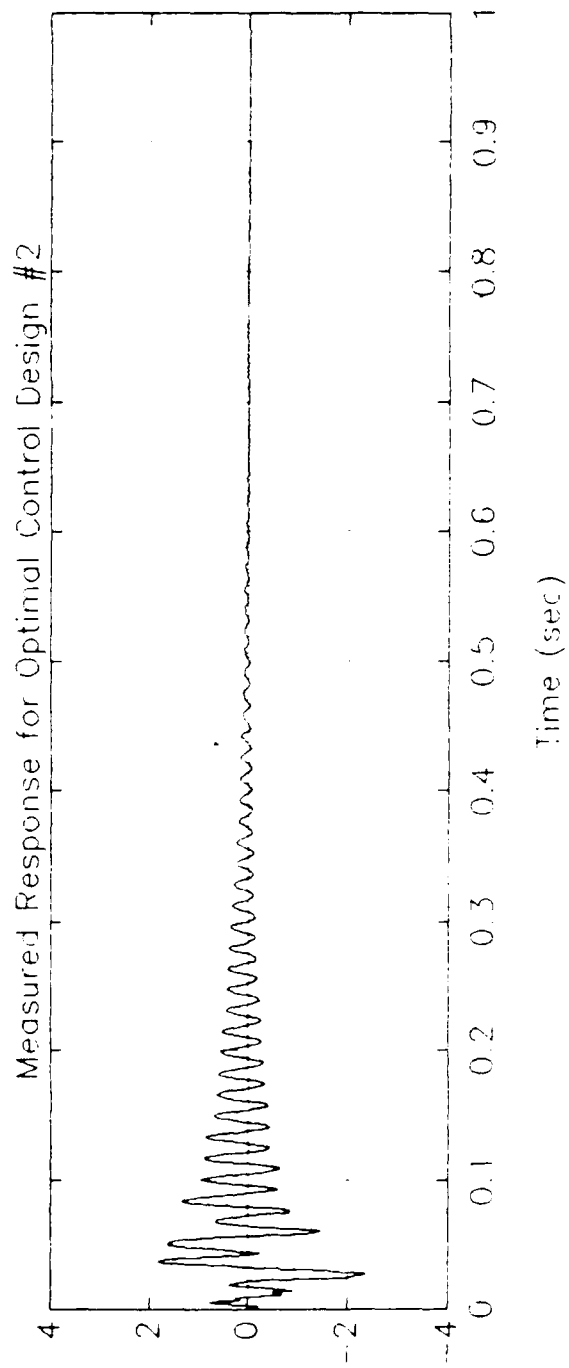
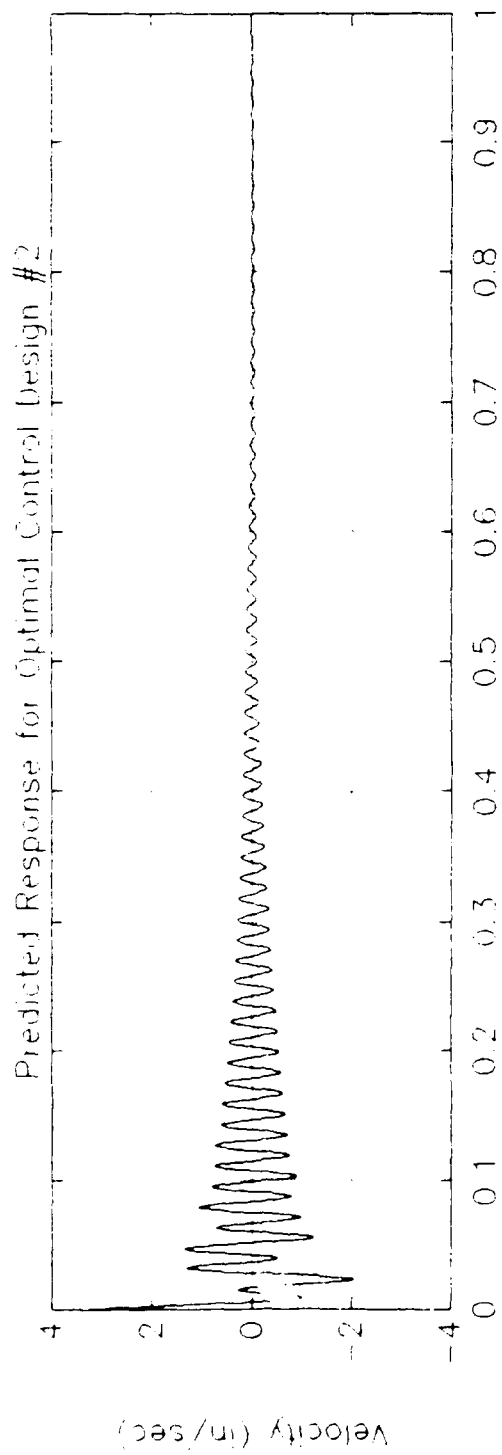


Figure 31. Optimal Control Design #2, Position 5 Response

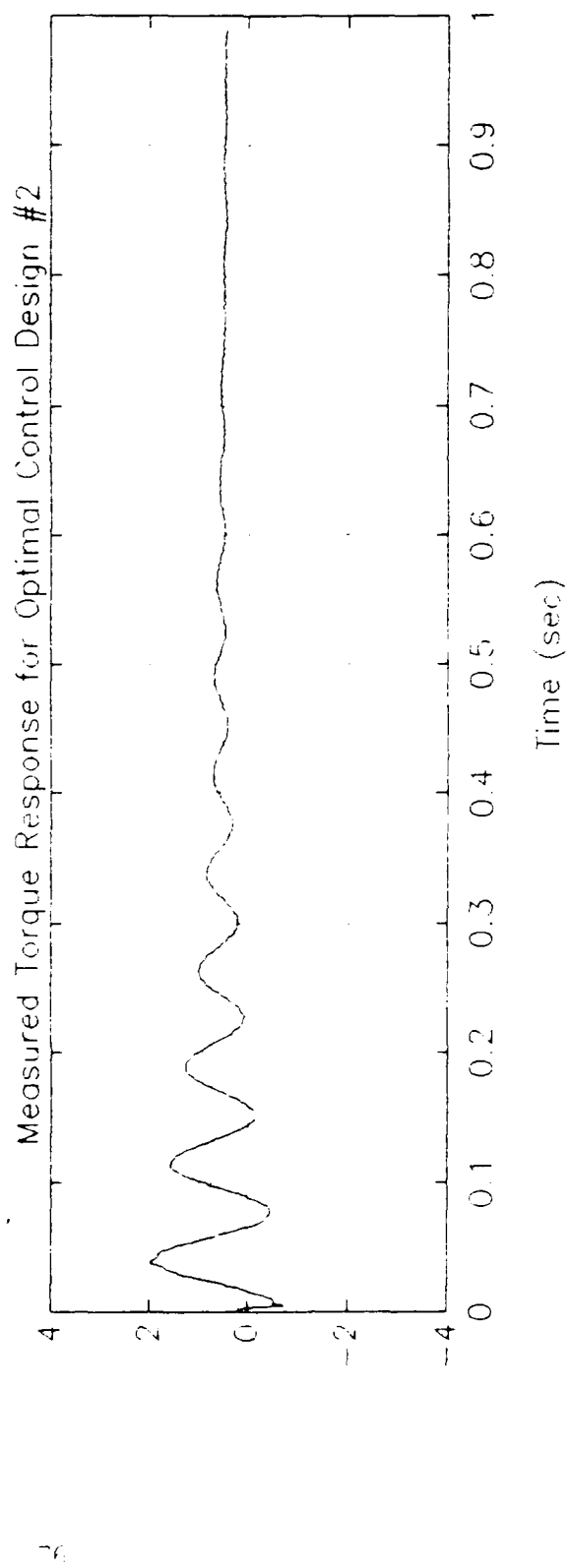
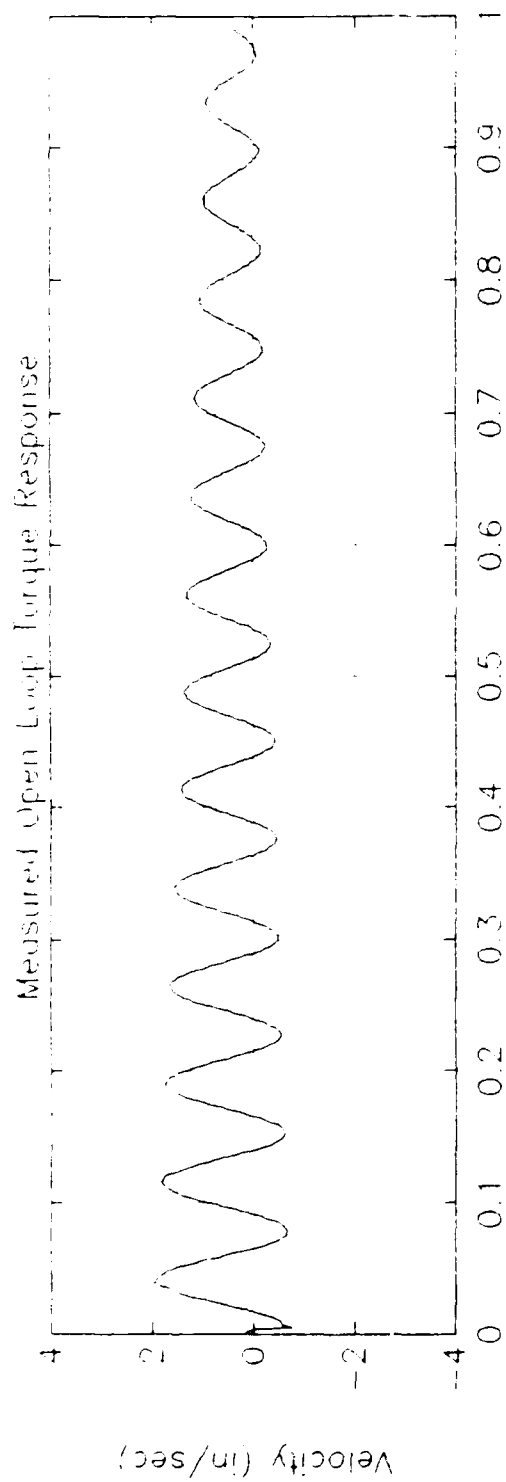


Figure 32. Optimal Control Design #2, Torque Response

modified, but this did not always help. In cases where the estimator damping on mode 3 was decreased (assuming greater "faith" in the model), the predictability and effectiveness of mode 3 control increased only marginally at best. In cases where the estimator damping on mode 3 was increased (assuming greater "faith" in the measurements), the entire system would be driven unstable. This was perplexing because direct measurement feedback without a filter actually produced predictable results during the system/gain verification tests. (These tests were discussed in the previous chapter.)

The root of the problem seems to be in the models for the measurement and plant noise which were used to generate the estimator gains. As a first cut, these models assumed uncorrelated, white, gaussian noises for both the plant and the sensors. In fact, these are known to be time correlated noises. The sensor noises (which initially appear at the acceleration level) become time correlated as they pass through the integrator circuits. There should also be a time correlation between the noises on the modal position and velocity states. Although the details will not be presented in this report, a better method for modeling these noises would be to assume zero mean, white, gaussian noises at the acceleration level, and then use a state augmentation procedure to combine linear shaping filters for the noise with the original system model. Even with this augmented system model, however, it is assumed that the acceleration noises are white, and this assumption will eventually need to be checked. The state augmentation procedure will increase the size of the final compensator according to the order of the shaping filters, but the PC-1000 can accomodate up to a 32 state compensator which should be more than sufficient for this problem. The noise modelling and state augmentation procedure can be found in Reference 21.

VII. Modal Suppression Techniques

Theory

Using a reduced order dynamic model for the estimator/controller can significantly decrease the computational burden for a large system. While this is not a problem with the ABE, it is easy to imagine a large, complex system which might have 50-100 modes in the same bandwidth where the ABE has four. In general, a large structure will present many more modes than can be reasonably controlled by a single system. If the system can be subdivided and subsets of the modes to be controlled assigned to separate controllers, the implementation of the control system can be greatly simplified. Often not all the modes may require active control to meet vehicle performance criteria. In such cases, reducing the order of the control model can greatly reduce the size and weight of the requisite control system.

The difficulty with implementing a reduced order model is that the sensors will generally still contain information about the modes which have been omitted from the model. Also, since the actuators operate on a continuous structure, they will excite and possibly destabilize these ignored modes. These effects have been classified as observation and control spillover respectively (14). Work by Coradetti (15) showed that spillover could be eliminated by finding a transformation matrix which is applied to the feedback gains, thus "suppressing" the omitted modes. Calico and Janiszewski (16) showed that eliminating either observation or control spillover was sufficient to ensure stability of the suppressed modes, and they demonstrated a procedure for calculating the appropriate transformation matrix. Wright (17) implemented this modal suppression technique on a single bending axis of a cantilevered beam. While being able to show increased stability in the second bending mode of the beam without destabilizing the

first or third modes, direct correlation between predicted and measured performance was not achieved. Cristler (8) applied modal suppression techniques to a single bending plane of the original ABE; however, observability and controllability problems associated with attempting to control second mode using proof mass actuators located near a node position prevented him from achieving conclusive results. Having corrected the observability and controllability problem with new sensor and actuator locations, it was decided to reattempt modal suppression techniques with the modified ABE.

The modal suppression technique begins by classifying the modes of the system as either controlled, suppressed, or residual. The state vector for the system is reordered in the form of

$$\underline{x}^T = [\underline{x}_c^T | \underline{x}_s^T | \underline{x}_r^T] \quad (57)$$

where \underline{x}_c is an n_c -vector of controlled states, \underline{x}_s is an n_s -vector of suppressed states, and \underline{x}_r is an n_r -vector of residual states. The modes included in \underline{x}_c are only those necessary to establish satisfactory system performance. In general, the controlled modes do not contain all the lowest frequency modes of the system. The suppressed states are defined as those modes which could potentially be destabilized in the process of controlling the more critical modes. The residual modes are those which can be safely ignored without fear of having them destabilized. In a multi-controller system, the controlled and suppressed modes would be partitioned into control groupings, and selected suppression used to decouple the multiple controllers. (See Ref 16.)

Using this partitioning, the state space model can be written as

$$\dot{\underline{x}}_c = A_c \underline{x}_c + B_c \underline{u} \quad (58)$$

$$\dot{\underline{x}} = A\underline{x} + B\underline{u} \quad (59)$$

$$\dot{\underline{x}} = A\underline{x} + B\underline{u} \quad (60)$$

$$\underline{y} = C\underline{x} + C\underline{x} + C\underline{x} \quad (61)$$

The control input is defined by

$$\underline{u} = -G\underline{x} \quad (62)$$

The coupling of the control \underline{u} into the suppressed and residual equations could excite and potentially destabilize these modes; this effect is known as control spillover.

A similar situation exists for the estimator. The estimator has the form

$$\dot{\underline{\hat{x}}} = A\underline{\hat{x}} + B\underline{\hat{u}} + K(\underline{y} - \underline{\hat{y}}) \quad (63)$$

$$\underline{\hat{y}} = C\underline{\hat{x}} \quad (64)$$

Note that $\underline{\hat{y}}$ still contains information about the suppressed and residual modes. This coupling can induce errors into the estimated state and thus generate inappropriate control commands, possibly driving the system unstable. This effect is known as observation spillover.

To maintain system stability, it is sufficient to eliminate either type of spillover (16). In most situations, it is more efficient to eliminate observation spillover. Eliminating

control spillover would effectively require an additional actuator for each mode to be suppressed, while the elimination of observation spillover requires an additional sensor (which is usually less expensive and lighter in weight) for each mode to be suppressed. This experiment will attempt to eliminate observation spillover.

The elimination of observation spillover is accomplished by constraining the estimator gain and output matrices such that

$$KC_c \neq 0 \quad (65)$$

$$KC_s = 0 \quad (66)$$

For a reduced order controller the residual modes are ignored, and the solution to equation 66 can be found by singular value decomposition of C_s . If C_s is of full rank, a solution exists only if the number of sensors is greater than the number of suppressed modes. This is necessary because eliminating the observation requires constructing a new measurement set \underline{w} , which is a linear combination of sensor outputs. The new set \underline{w} is of reduced dimension because the suppressed modes have in effect been subtracted out of the measurements. The dimension of \underline{w} will be n_s less than the original output set \underline{y} . The results of the singular value decomposition of C_s are an orthogonal set of left singular vectors which can be partitioned into two sets; defining the set associated with the zero singular values as Γ , equation 66 becomes

$$\Gamma C_s = 0 \quad (67)$$

Defining a new relation to represent the output after the suppressed modes are removed

$$\underline{w} = \Gamma \underline{y} \quad (68)$$

equation 61 becomes

$$\underline{w} = \Gamma C \underline{x}_e + \Gamma C \underline{x}_r + \Gamma C \underline{x}_s \quad (69)$$

If we ignore the residual modes and use the results of equation 67

$$\underline{w} = \Gamma C \underline{x}_e \quad (70)$$

The new estimator/controller equations become

$$\dot{\underline{x}}_e = (A_e - B_e G - K \Gamma C_e) \underline{x}_e + K \Gamma \underline{y} \quad (71)$$

$$\underline{u} = -G \underline{x}_e \quad (72)$$

The discrete time formulation of equation 71 and its adaptation for use in the PC-1000 is identical to equations 47-54, when the full state matrices are replaced with their reduced order counterparts, and the estimator gain matrix K is replaced with ΓK .

Modal Suppression Design #1

As an example of the modal suppression technique, the control gains of the second optimal control design discussed in the previous chapter were implemented on a reduced order estimator/controller. State 3 (mode 3 bending) was designated as the suppressed

state, and the residual states were defined as the unmodelled higher frequency modes. As a comparison set, the same reduced order controller was implemented without suppressing mode 3 from the measurements. The predicted damping levels for both cases are listed in Table XII. In the case where modal suppression was not applied, an increase in mode 3 damping was predicted; however, ignoring modes could have just as well caused a decrease in damping to the point of instability. Although the potential destabilizing effect is not predicted to occur in this case, other selections for the suppressed modes, or a different structure altogether could have caused this potential problem to materialize. The case where modal suppression was applied predicts (as expected) no change in mode 3 damping. The same gains produce less of an increase in mode 2 damping than they did with the full order optimal control design, but the "size" of the compensator has been reduced and mode 3 should be unaffected by control of the other modes.

Table XII. Modal Suppression Design #1 Predictions

Mode #	Damping (%)		
	Open Loop	Without Suppression	With Suppression
1 (Z1)	6.4	6.7	6.6
2 (Z2)	2.4	17.5	13.2
3 (Z3)	1.2	1.8	1.2
4 (T1)	0.84	6.9	6.9

Measured results from the implementation of modal suppression design #1 on the ABE are listed in Table XIII. Although not predicted, the ignored mode (Mode 3) was slightly destabilized when suppression was not applied. It is not surprising that the

controller without suppression produced unpredictable results for mode 3 damping because the estimator was not told to look for mode 3 information. The mode 2 prediction for the controller without suppression actually came closer than expected to the measured values. For the controller with suppression applied, there is good agreement between the predicted and measured values for mode 2 damping. Mode 3 did not lose stability under the controller with suppression applied, but the measured damping was significantly different than that predicted by the model. Mode 3 should have been unaffected by this controller, but the measured value showed more of an increase in damping than it did for the second optimal control design. Suspected reasons for this discrepancy are slight coupling between modes 2 and 3 which have not been accounted for, and an estimator whose inaccuracies are much more prevalent in mode 3. The estimator problems were discussed in the previous chapter.

Table XIII. Modal Suppression Design #1 Results

Mode #	Damping (%)		
	Open Loop	Without Suppression	With Suppression
1 (Z1)	6.4	6-7	6-7
2 (Z2)	2.4	17.4 \pm .5	12.7 \pm .5
3 (Z3)	1.2	1.0 \pm .2	2.2 \pm .2
4 (T1)	0.84	7.1 \pm .2	7.0 \pm .2

Modal Suppression Design #2

A more dramatic example of the modal suppression technique would demonstrate that a middle frequency could be suppressed while both higher and lower frequency

modes were being controlled. To demonstrate this, mode 2 was designated as the controlled mode, and a feedback gain matrix was constructed such that actuator C would control mode 3, and actuators A and B would control modes 1 and 4. The residual modes were again considered to be the unmodelled higher frequency modes. A comparison test was generated which utilized the reduced order controller without suppressing mode 2 information from the measurements. Table XIV lists the predicted damping levels for the two cases. Ignoring mode 2 without suppressing it shows an increase in the damping level for that mode, but again, on a different system this could have caused a decrease in damping and/or instability.

Table XIV. Modal Suppression Design #2 Predictions

Mode #	Damping (%)		
	Open Loop	Without Suppression	With Suppression
1 (Z1)	6.4	6.6	6.2
2 (Z2)	2.4	7.0	2.4
3 (Z3)	1.2	7.9	7.5
4 (T1)	0.84	6.9	6.9

The modal suppression design #2 was attempted on the beam, but the results were extremely unpredictable. The reason for the unpredictable results is the estimator which was used in the control implementation. The weighting matrices for the estimator were adjusted, but at best this caused a marginal increase in predictability, and at worst the estimator caused the entire system to go unstable. In its present form, the estimator can not be used for control of mode 3, and the suggested changes to the estimator mentioned in the previous chapter should be investigated prior to reattempting this modal suppression design.

Suppression of mode 2 was also attempted using direct measurement feedback. This is similar to the analog measurement feedback which was run during system verification phase, except mode 2 information was suppressed from the measurements. (The suppression necessitated a digital implementation for this test.) The resulting set of "measurements" contained one signal which was dominated by mode 3, and two signal which were dominated by a combination of mode 1 and mode 4. The signal dominated by mode 3 information was fed back directly to the shaker (actuator C). Table XV list the predicted and measured results of the direct feedback implementation. Although this test did show that mode 2 could be suppressed while controlling mode 3, it did not demonstrate predictable behavior by the system. The measured damping in mode 3 is significantly greater than that predicted by the model. This discrepancy is somewhat disturbing because the earlier analog feedback test provided very good results. However, the whole idea of using a modal suppression controller without an estimator of some sort is not realistic in itself. This test was primarily designed to see if mode 3 could be controlled at all while suppressing mode 2. The suppression design #2 with the estimator in place could not produce any significant increase in mode 3 damping.

Table XV. Results of Suppression with Direct Measurement Feedback

Mode #	Damping (%)		
	Open Loop	Prediction	Measured
2 (Z2)	2.4	2.4	2.3 \pm .2
3 (Z3)	1.2	4.0	7.0 \pm .3

VIII. Conclusions and Recommendations

Fundamental Issues

Prior to closing out this report, a brief discussion of some of the design issues which must be addressed by this and other structural control experiments is warranted. One of the fundamental issues is whether the experiment will represent a scale model of a class of structure, or simply a controls experiment. The first category places much more stringent constraints on the type of actuators and sensors, as well as the design of the structure used in the experiment. For instance, in order to provide a model for a large space structure, only inertial sensors and actuators can be used. Presently, the availability of sensors and actuators for this type of experiment is limited. While accelerometers can provide excellent measurements of structural vibrations, integrating their output to provide velocity measurements introduces low frequency drift, and integrating a second time to obtain position feedback would compound the problem further. Most of the actuators being used in space structure experiments must be custom made, and in the case of the linear proof mass actuators, they provide inadequate control force for the lowest frequency modes. On the other hand, a controls experiment which makes no attempt to simulate a zero-gravity environment has a wealth of options to choose from in the selection of sensors and actuators. The structural dynamics shaker used for the modified ABE provided sufficient and predictable control force, and there are "off the shelf" optical sensors which can accurately measure both position and velocity without the need for integration. Because these instruments often require fixed mountings, they are not always appropriate for a LSS experiment; however, they can perform nicely as feedback elements in a controls experiment. Although any control system for a LSS will need to be adapted for and tested with inertial instruments, valid

testing for the control algorithm itself can be run on a "controls" experiment.

Having said this, the reader might ask "Where does the ABE fit into this discussion?". The ABE was originally developed as a simple space structure model using inertial sensors and actuators. Out of necessity the ground mounted shaker was added, thus invalidating the original goals of a space structure simulation. However, it is the author's opinion that the ABE still represents a valid controls experiment for the LSS vibration problem. As such, the author would not be disappointed to see other ground referenced sensors and actuators find their way onto the system. The results of the ABE can still be applied to the LSS problem, as well as other applications for control of structural vibrations.

Capabilities and Limitations of the ABE

The modified ABE is a simple and usable baseline experiment for the structural vibration controls problem. Because of the simplicity of the structure, it is not capable of demonstrating some of the intricacies of larger, more complex structures which will undoubtedly have many more vibration modes, with many of these modes being coupled. However, the ABE does provide a test platform on which simple implementations of candidate controllers can be evaluated prior to being tested on much more complicated systems. Although the ABE has its idiosyncrasies, it is well understood, and a good model for the system has been developed.

If the ABE is to be used in the future, several modifications to the system should be considered. The first improvement should be in the sensor channels. The instrumentation amplifiers in the feedback path should be replaced with low noise amplifiers that also provide better offset and zero adjustments. Related to the offset problem, the operation of the PC-1000 needs to be investigated more closely to

determine the cause of offsets which develop in the state estimation process. Part of this problem is caused by non-zero mean sensor noise, and part of the problem may lie with the estimator algorithms being used. Time constraints did not allow a complete investigation of this problem. If offsets continue to be a problem, instrumentation amplifiers should be added between the PC-1000 outputs and the actuators in order to remove the offsets. Once the measurement channels have been revamped, a statistical analysis of the sensors, actuators, and system model should be considered. This could be used to design improved estimators and controllers based on stochastic methods.

Although the ABE is capable of producing predictable results using the proof mass actuators, the behavior and low frequency output of these devices leaves much to be desired. The actuators have been "compensated to death", and should be replaced before additional compensation is considered. Alternatives to these include other proof mass actuator designs, small pneumatic reaction jets, or additional structural dynamics shakers. Another intriguing alternative is the use of torque motors to provide applied torque at node positions. Small, but relatively powerful torque motors with flywheels could be applied in equal and opposite pairs at node positions on the beam. These devices would not experience the same momentum storage limitations as the linear proof mass actuators, and they also represent a significant size and weight savings.

An additional use for the ABE which has not yet been fully developed is its potential for testing different system identification techniques. Adaptive parameter estimation techniques which account for changes in the configuration could be tested on the ABE. The importance of these methods is due to the fact that a complete modal analysis on an

actual space structure can not be conducted each time the configuration changes.

Related to this problem, robust control algorithms which allow for parameter changes could also undergo preliminary testing on the ABE.

Bibliography

1. Meirovitch, L., Baruh, H., Montgomery, R., Williams, J., "Nonlinear Natural Control of an Experimental Beam," Journal of Guidance and Control, Vol. 7, No. 4, 1984, pp. 437-442.
2. Juang, Jer-Nan, Turner, James D., "Research in Slewing and Tracking Control", Proceedings of NASA/DOD Control/Structures Interaction Technology Conference, 1986, pp.869-880.
3. Schaechter, D.B., Eldred, D.B., "Experimental Demonstration of the Control of Flexible Structures," Journal of Guidance and Control, Vol. 7, No. 5, 1984, pp. 527-534.
4. Aubrun, J.N., Ratner, M.J., "Structural Control for a Circular Plate". Journal of Guidance and Control, Vol. 7, No. 5, 1984, pp. 535-545.
5. Martin, Joe, "A Free-Free Beam for the Study of Spacecraft Control", MS Thesis, The Ohio State University, Columbus, Ohio, 1987.
6. Kotnik, Paul T., "Modelling and Control of a Flexible Manipulator System", MS Thesis, The Ohio State University, Columbus, Ohio, 1987.
7. Gruzen, A., Vander Velde, W.E., "Robust Reduced-Order Control of Flexible Structures Using the Optimal Projection/Maximum Entropy Design Methodology", American Institute of Aeronautics and Astronautics, Inc., 1986, pp. 1-9.
8. Cristler, Thomas, "Active Vibration Control of a Cantilevered Beam with Three Elastic Coordinates", MS Thesis, Air Force Institute of Technology, Wright-Patterson AFB, Ohio, 1987.
9. Breitfeller, Eric F., "Modelling and Control of a Cantilevered Beam with End-Mass", MS Thesis, The Ohio State University, Columbus, Ohio, 1988.

10. Roark, R.J., Young, W.C., Formulas for Stress and Strain, (Fifth Edition), McGraw-Hill, New York, 1975.
11. Structural Dynamics Canon, Quixote Measurement Dynamics, Inc., Document 50630, Cincinnati, Ohio, 1984.
12. STAR Modal Operating Manual, Structural Measurement Systems, Inc., San Jose, California, 1988.
13. PC-1000 Systolic Array Processor Operations Manual, Systolic Systems Inc., Campbell, California, 1987.
14. Balas, M.J., "Active Control of Flexible Systems", AIAA Symposium on Dynamics and Control of Large Flexible Spacecraft, Blacksburg, Virginia, June 14, 1977.
15. Coradetti, T., "Orthogonal Subspace Reduction of Optimal Regulator Order", Proceedings of the AIAA Guidance and Control Conference, Boulder, Colorado, August 6-8, 1979.
16. Calico, Robert A., Jr, Janiszewski, A.M., "Control of a Flexible Satellite via Elimination of Observation Spillover", Proceedings of the Third VPI&SU/AIAA Symposium on the Dynamics and Control of Large Flexible Spacecraft, Blacksburg, Virginia, June, 1981.
17. Wright, Richard L., Jr, "Experimental Control of Simultaneously Excited Structural Modes", MS Thesis, Air Force Institute of Technology, Wright-Patterson AFB, Ohio, 1985.
18. Meirovitch, L., Analytical Methods in Vibrations, McMillan Publishing Co., New York, 1967.
19. Ridgely, D. Brett, Banda, Siva S., Introduction to Robust Multivariable Control, AFWAL-TR-85 3102, Flight Dynamics Laboratory, Air Force Wright Aeronautical Laboratories, Air Force Systems Command, Wright Patterson AFB, Ohio, 1986.

20. PC-MATLAB, The MathWorks, Inc., Sherborn, MA, 1987.
21. Maybeck, Peter S., Stochastic Models, Estimation, and Control Volume I, Academic Press, Inc., San Diego, CA, 1979.

Appendix A: Component Specifications

LINEAR MOTORS

**KAISER
ELECTROPRECISION**

DEFINITIONS (Continued)

CONTINUOUS RMS CURRENT - Using maximum power dissipation and 60Hz impedance (since it is essentially resistive), a maximum current rating can be calculated from $P = I^2 R$. However, the resistance used in this calculation is at maximum temperature, not the room temperature value given on the data sheet.

The resistances of both the coil and the secondary increase at 0.4% per degree Celsius, and the typical temperature rise of the secondary is about 2-3 that of the coil. RMS current rating is calculated from this information, or measured experimentally.

RMS current rating multiplied by force constant gives RMS force rating. This is a useful number of comparing capabilities of motors, and is similar to rated torque of a rotary motor.

PULSE CURRENT - Three factors limit the maximum current pulse that may be applied to the motor:

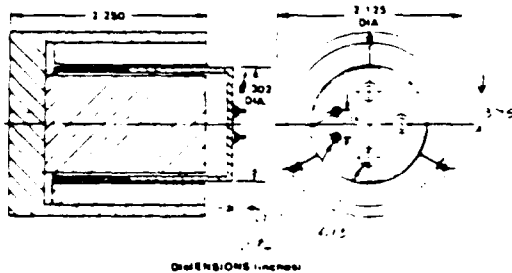
- Demagnetization
- Heating damage to the coil connectors
- Physical strength of the armature assembly

Armatures are normally tested for strength at high temperature so that this failure mode should not be the limiting one. The other two processes depend on current pulse width as well as amplitude. Demagnetization only becomes a problem after secondary current, whose flux opposes armature flux, decays. Damage to connections only occurs if the current pulse is long enough to heat them excessively. The value given on the data sheet is a conservative one based on tests and experience.

MODEL 512 LINEAR MOTOR

The Model 512 is for use in disc recording systems, and other applications requiring servo-controlled linear motion. Constant force range is 0.9 inches. Total stroke is 1 inch.

Special units can be built with force constant up to 2.1 lb-amp.



DIMENSIONS (inches)

MOTOR CHARACTERISTICS AT 25°C

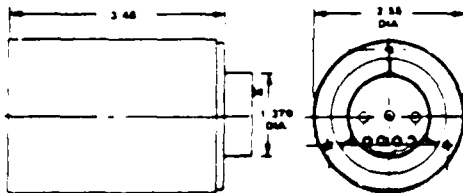
Force Constant	= 0.9 lb-amp
Coil DC Resistance	= 6 ohms
Coil inductance (unextended)	= 52 mH @ 1 kHz
Coil Mass	= 22.5 gm
Total Motor Weight	= 195 gm (7.0 oz)

MAXIMUM RATINGS AT 25°C AMBIENT

Coil Temperature	= 100°C
Power Dissipation	= 36 watts
Continuous RMS Current (dissipation limited)	= 2.4 amps
Pulse Current	= 10 amps (0.1 sec)

MODEL 517 LINEAR MOTOR

The Model 517 is a permanent-magnet moving-coil DC linear motor designed for positioning heads on floppy disc drives and for other applications requiring a compact linear driver. The constant force stroke length of the standard unit is 1.8 inches. Special motors of the same diameter but greater length can be designed for stroke requirements up to 3 inches without loss of efficiency. Customer specified coil resistances and mounting interfaces can be provided. Single and bifilar wound coils are available.



DIMENSIONS (inches)

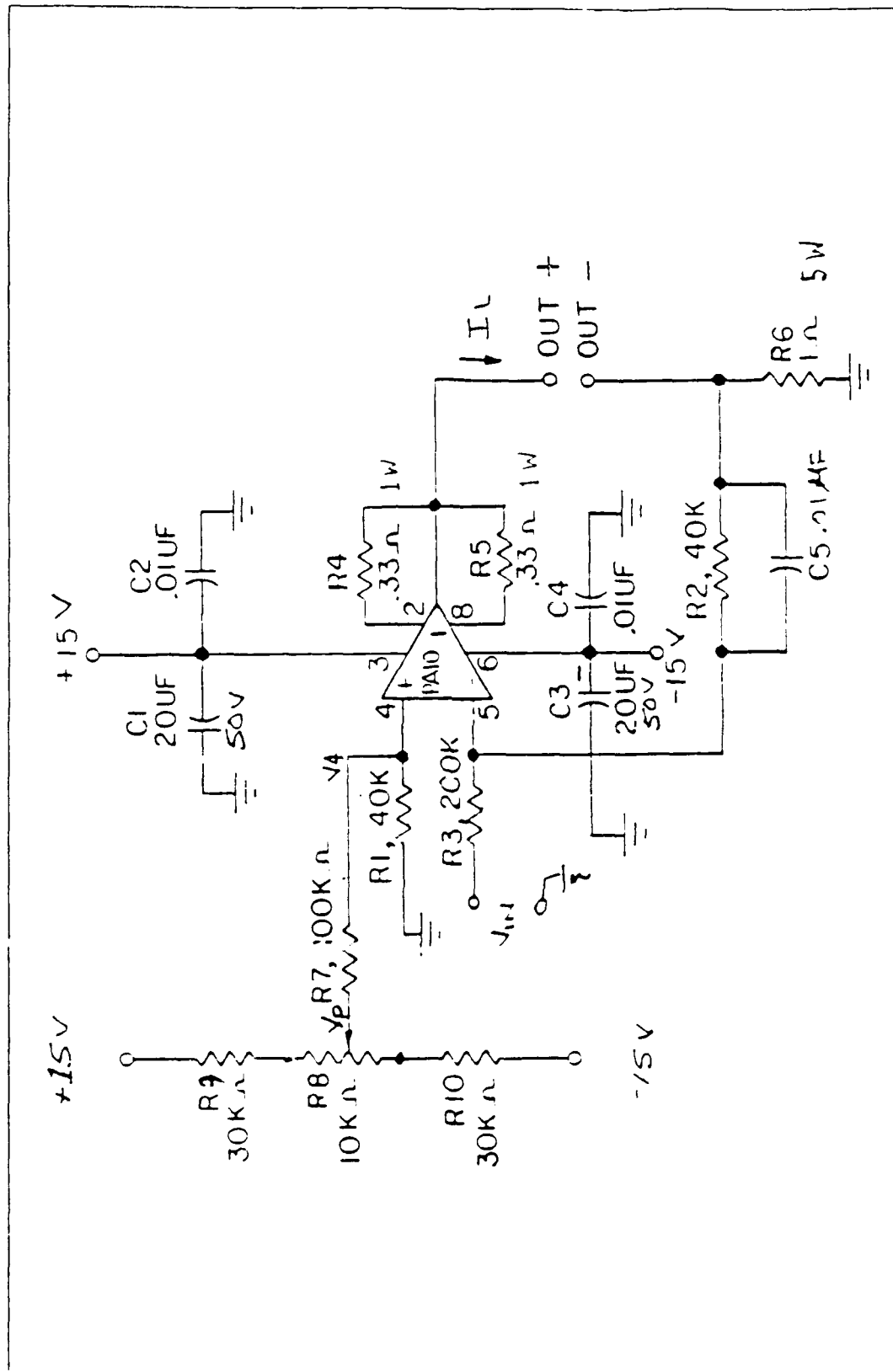
MOTOR CHARACTERISTICS AT 25°C

Bifilar Winding - electrical characteristics for one half of winding

Force Constant	= 1.8 lb-amp
Coil DC Resistance	= 12 ohms
Coil inductance (unextended)	= 20 mH @ 1 kHz
Coil inductance (extended)	= 3.6 mH @ 1 kHz
Thermal Resistance (coil to air)	= 15 °C/W
Coil Mass	= 4 gm
Total Motor Weight	= 1.1 lb

MAXIMUM RATINGS AT 25°C AMBIENT

Coil Temperature	= 150°C
Power Dissipation	= 6 watts
Continuous RMS Current (dissipation limited)	= 0.7 amps
Pulse Current	= 10 amps (0.1 sec)



Power Amplifier Circuit Diagram

ENDEVCO® MODELS 2262-25/2262C-25 **LOW g (DAMPED) PIEZORESISTIVE ACCELEROMETERS** ± 25 g

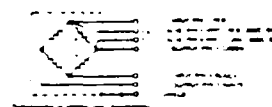
The Models 2262-25 and 2262C-25 Accelerometers are designed to measure a broad variety of long duration, low level acceleration phenomena. ENDEVCO's PIEZITE® Type P-111 elements are employed in a bridge circuit to obtain a high level output at ± 25 g full scale. This output is high enough to drive most tape recorders and low frequency galvanometers directly without amplification. The Model 2262C-25 is a six-wire device that uses a pair of fixed resistors in half the bridge to present a fixed resistance to the extra pair of leads for shunt calibration techniques.

Although the rated range of these transducers is ± 25 g, they may be used to ± 50 g. A unique system of overrange stops limits the movement of the seismic element allowing the units to withstand shock up to 80 times their rated range without calibration shift. Viscous damping extends their useful frequency range and reduces the effect of spurious, high frequency vibrations. Typical applications for these accelerometers include transportation environment testing, transient accelerations on large structural members, and combined environments of steady state acceleration plus transient inputs.



(All values are typical at -75°F (-24°C) unless otherwise specified.)

	MODEL 2262-25	MODEL 2262C-25
RANGE	± 25	± 25
SENSITIVITY		
100 mV excitation (at 100 Hz)		
Typical/Minimum	mV/g 20/16	10/8
NON-LINEARITY & HYSTERESIS		
% of reading, max. to full range	% ± 1	± 1
FREQUENCY RESPONSE		
25% max. (at 100 Hz)	Hz 0 to 850	0 to 850
MOUNTED RESONANT FREQ	Hz 2500	2500
DAMPING RATIO	0.7 \pm 0.15 \pm 0.10	0.7 \pm 0.15 \pm 0.10
TRANSVERSE SENSITIVITY (max)	% 3	3
THERMAL SENSITIVITY SHIFT		
(ref. -75°F -24°C)	% -5 -20 -2 -5	-5 -20 -2 -5
	$^{\circ}\text{F}$ 0 -25 -75 -150 -200	0 -25 -75 -150 -200
	$^{\circ}\text{C}$ -18 -6 -24 -66 -93	-18 -6 -24 -66 -93
ZERO MEASUREMENT OUTPUT (max)	mV ± 25	± 25
THERMAL ZERO SHIFT (max)	mV ± 20	± 20
BASE STRAIN SENSITIVITY	EO g 0.005	0.005
ELECTRICAL		
EXCITATION*	Vac 10.0	10.0
INPUT RESISTANCE*	Ω 1800	1000
OUTPUT RESISTANCE	Ω 1400	1000
INSULATION RESISTANCE	M Ω 100 leads to case	100 leads to case
GROUNDING	Cable shield common to case	Cable shield common to case
	Case isolated from sensors	Case isolated from sensors
PHYSICAL		
WEIGHT (excluding cable)	oz (gm) 1.28	1.28
CASE MATERIAL	Stainless steel, type 416	Stainless steel, type 416
ELECTRICAL CONNECTIONS	Integral six-pin connector	Integral six-pin connector
MOUNTING TORQUE	Use for 10-32 mounting stud	Use for 10-32 mounting stud
	18 (in 2 Nm)	18 (in 2 Nm)
ENVIRONMENTAL		
ACCELERATION LIMITS		
(in any direction)		
Static	g 250	250
Shocks	g 250	250
Temperature	g 2000	2000
Operating	$^{\circ}\text{F}$ ($^{\circ}\text{C}$) 0 to $+200$ (-18 to $+93$)	0 to $+200$ (-18 to $+93$)
Non-Operating	$^{\circ}\text{F}$ ($^{\circ}\text{C}$) -20 to $+220$ (-29 to $+104$)	-20 to $+220$ (-29 to $+104$)
Humidity	hermetically sealed by welding and glass-to-metal fusion	hermetically sealed by welding and glass-to-metal fusion
CALIBRATION DATA SUPPLIED		
(at -75°F -24°C) and 10.00 VAC excitation)		
FREQUENCY RESPONSE RANGE	Range in Hz	
SENSITIVITY (at 100 Hz)	mV/g	
ZERO MEASUREMENT OUTPUT	mV	
MAXIMUM TRANSVERSE SENSITIVITY	% of calibrated sensitivity	
MOUNTED RESONANT FREQUENCY	Hz	
DAMPING RATIO	Ratio of critical damping	
INPUT AND OUTPUT RESISTANCE	Ω	



NOTES

Non-linearity above ± 25 g is $\pm 0.5\%$ of reading, maximum to 50 g.

Frequency response at a damping ratio of 0.7 is $\pm 15\%$ $\pm 0.5\%$ typical at 0° -200°F (-18° $+93^{\circ}\text{C}$) and 2000 Hz.

Thermal Zero Shift (max) values specified are at 0° -200°F (-18° $+93^{\circ}\text{C}$) reference -75°F (-24°C).

*Rated excitation: 10.0 VAC. The strain gauge elements have a positive temperature coefficient of resistance of approximately 0.5% per $^{\circ}\text{F}$.

*Other excitation voltages may be used to 5.0 VAC but should be specified in order to obtain a more accurate calibration. Warmup time to meet all specifications is two minutes, maximum. ENDEVCO Model 4427 Signal Conditioner is recommended as the excitation source.

*Measured at approximately 1 VAC. Bridge resistance increases with applied voltage.

ACCESSORIES INCLUDED

Model 2261-1, 10-32 or Model 2261-4, M5 metric mounting stud.

2262-25, Model 22278-30 Cable Assembly, 6-conductor, shielded, 30 in. (76 cm) long.

2262C-25, Model 22238-30 Cable Assembly, 8-conductor, shielded, 30 in. (76 cm) long.

U.S. Patent Nos. 3,511,871; 3,511,872; 3,511,873; 3,511,874; 3,511,875.

Continued product improvement necessitates that Endevco reserve the right to modify these specifications without notice. Endevco maintains a program of constant surveillance over all products to ensure a high level of reliability. This program includes attention to reliability factors during product design, the support of stringent Quality Control requirements, and a quality corrective action procedure. These measures, together with conservative specifications, have made the name Endevco synonymous with reliability.



World Headquarters: 30700 Rancho Viejo Road, San Juan Capistrano, CA 92675 USA (714) 493-8181 Telex: 68-5808 TWX: 910-586-1415

HPD SERIES—HERMETICALLY SEALED (PIN TERMINATION)

- HERMETICALLY SEALED BY TIG AND EB WELDING
- IMPERVIOUS TO HOSTILE ENVIRONMENTS
- THROUGH-BORE CONSTRUCTION

HPD Series units are similar to the DC-D and HCD Series. Tungsten inert gas (TIG) and electron beam (EB) welding provide hermetic sealing that is free from oxidation,

producing faults that may cause leakage. For this reason, HPD Series LVDT's are impervious to dirt, water, steam spray, and most corrosives. They have been qualified at pressures up to 1000 psig (70 bars) and are suitable for numerous high-pressure applications. HPD units employ a glass-sealed, pin-terminal header that allows the core and core rod to pass through the unit. HPD units have double magnetic shielding that makes them insensitive to external magnetic influences.

GENERAL SPECIFICATIONS

Input: ± 15 V DC (nominal), ± 20 mA
 Operating Temperature Range: 0°F to $+160^{\circ}\text{F}$ (-18°C to $+70^{\circ}\text{C}$)
 Survival Temperature Range: -65°F to $+200^{\circ}\text{F}$ (-55°C to $+95^{\circ}\text{C}$)
 Null Voltage: 0 V DC
 Ripple: Less than 25 mV rms
 Linearity: $\pm 0.25\%$ full range
 Stability: 0.125% full scale

Temperature Coefficient of Scale Factor: $0.04\%/^{\circ}\text{F}$ ($0.08\%/^{\circ}\text{C}$)
 Shock Survival: 250 g for 11 milliseconds
 Vibration Tolerance: 10 g up to 2 kHz
 Coil Form Material: High density, glass-filled polymer
 Housing Material: AISI 400 series stainless steel
 Electrical Termination: 6-pin terminal header
 Output Impedance: Less than 1 Ohm

PERFORMANCE SPECIFICATIONS AND DIMENSIONS

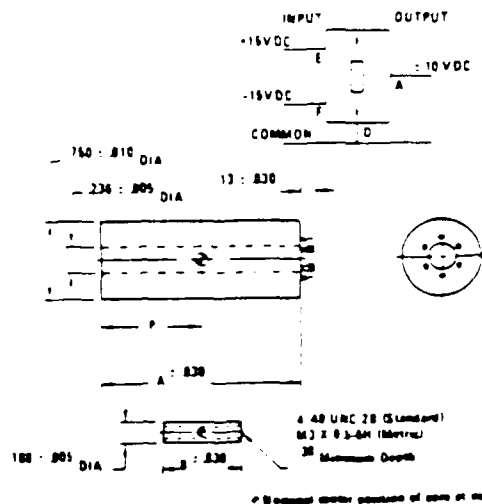
LVDT MODEL NUMBER	NOMINAL LINEAR RANGE	SCALE FACTOR	RESPONSE - 1σ	WEIGHT Grams	HEIGHT	DIMENSIONS	P
	inches	V/inch	Hz	Body Core	inches	inches	inches
950 HPD	± 0.050	200	500	36 2	2.40	0.59	0.55
125 HPD	± 0.125	80	500	45 3	3.23	1.10	0.96
250 HPD	± 0.250	40	500	57 5	4.10	1.80	1.39
500 HPD	± 0.500	20	700	77 8	5.79	3.00	2.23
1000 HPD	± 1.000	10	200	115 10	8.05	3.80	3.32
2000 HPD	± 2.000	5.0	200	169 13	11.42	5.00	5.05
3000 HPD	± 3.000	3.3	200	231 14	16.67	6.20	7.50
5000 HPD	± 5.000	2.0	200	284 17	20.45	6.20	9.56
10000 HPD	± 10.00	1.0	200	520 24	34.57	12.00	16.61

ORDERING INFORMATION

(Fold out page 32 for instructions on how to use this chart.)

OPTION NO	906	910	929	940	950
MODEL NO					
950 HPD	N	B	B	-	X
125 HPD	N	B	B	-	X
250 HPD	N	B	B	-	X
500 HPD	N	B	B	-	X
1000 HPD	N	C	X	-	X
2000 HPD	N	C	X	-	X
3000 HPD	N	C	X	-	X
5000 HPD	N	C	X	-	X
10000 HPD	N	C	X	-	X

Note 1: See outline drawing for metric thread size.
 Note 2: Consult factory for mass dimensions and thread size.





ACOUSTIC POWER SYSTEMS, INC.

Systems for Generating Controlled Vibration

SPECIFICATIONS

Average Output, into shaker reactive load
Peak Output, into shaker reactive load
Current Output, peak (random noise)
Current Output, continuous
Frequency Range
Input Signal Voltage
Input Impedance
Noise — referred to max. output
Current Monitor output
Input Power
Rear Panel Connectors
Power Output
Input Current Monitor
AC Power
Weight
Size HxWxD

Model 114

125 V-A rms
250 V-A rms
6.0 A peak
4.0 A rms
0-2000 Hz
2 V peak
100 K ohm
-90 dB
250 mV/A
120 V, 50-60 Hz, 300 W
220-240 V optional
WK3-31 S (Cannon)
BNC Type 3 ea
Std 3-Pin Receptacle
25 lb (11.3 kg)
5.22 x 17 x 9.25 inches
133 x 432 x 235 mm

Model 124

250 V-A rms
500 V-A rms
12.0 A peak
8.0 A rms
0-2000 Hz
2 V peak
100 K ohm
-90 dB
125 mV/A
120 V, 50-60 Hz, 600 W
220-240 V optional
WK3-31 S (Cannon)
BNC Type 3 ea
Std 3-Pin Receptacle
45 lb (20 kg)
5.22 x 17 x 13.25 inches
133 x 432 x 337 mm

Model 124-EP

250 V-A rms
750 V-A peak
18.0 A peak
8.0 A rms
0-2000 Hz
2 V peak
100 K ohm
-90 dB
125 mV/A
120 V, 50-60 Hz, 600 W
240 V optional
WK3-31 S (Cannon)
BNC Type 3 ea
Std 3-Pin Receptacle
45 lb (20 kg)
5.22 x 17 x 13.25 inches
133 x 432 x 337 mm

SPECIFICATIONS

Input Signal Level
Input Impedance
Output Signal Level
Output Source Impedance
Frequency Range
Noise — referred to max. output
Weight
Size HxWxD

Model 115

1 V peak
100 K ohm
0 to 10 V peak
50 ohm
0-5000 Hz
-90 dB
10 lb (4.5 kg)
5.22 x 17 x 6.25 inches
133 x 432 x 159 mm

Note: Rack adapters are included with amplifiers & control panels for standard 19-in rack mounting.

SYSTEM CABLES Shaker to Power Amplifier

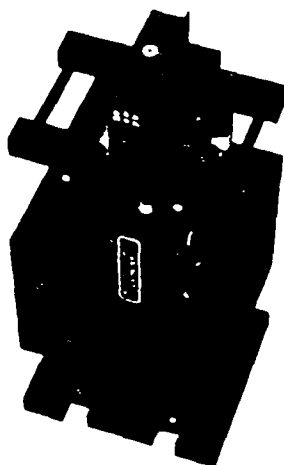
System Interconnect Cable 0081-20A-2C Standard length 20 feet section A, 2 ft section C

Models 113, 113-AB and 113-LZ to Models 114, 123 & 124

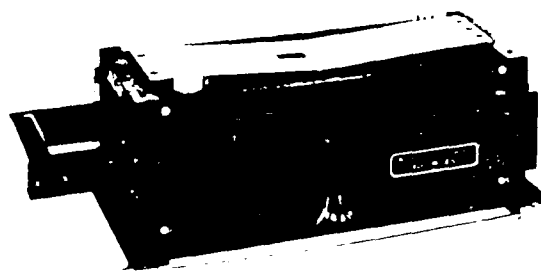
System Interconnect Cable 0081-20A Standard length 20 feet

Models 113-LA, 120S, 129, and 220, to Models 114, 123, 124 and Extension

5731 PALMER WAY, SUITE A, CARLSBAD, CA 92008 U.S.A. • (619) 438-4848 • FAX (619) 438-8845 • TELEX 4995113 (SHAKE)



APS 113 with
0112 Reaction Mass



APS 113 Air Bearing Shaker

OPTIONAL CONFIGURATIONS

APS 113-AB Air Bearing Model Air lubricated bushings replace the linear ball bushings used in the basic **ELECTRO-SEIS** armature guidance system. In addition an air distribution system, tie down and leveling base are provided.

The near zero friction of the air bushings is an essential feature for measuring resonance decay rates in very lightly damped structures.

The Air Bearing configuration extends the application of the basic APS 113 to include the calibration and evaluation of accelerometers and other motion transducers in the seismic frequency range.

APS 113-LZ Low Impedance Coil

All features of the basic

ELECTRO-SEIS Shaker are retained. The drive coil is wound in a manner which allow series or parallel connection, offering the user the choice of standard or low impedance. This option is required if the shaker is to be used with the APS 124

DUAL MODE Power Amplifier for extended frequency range or random noise excitation.

APS 113-HF High Force Coil

All features of the basic

ELECTRO-SEIS Shaker are retained as in the APS 113-LZ. The drive coil is provided to match the APS 124 **DUAL MODE** Power Amplifier for 40% increase in force with a 50% duty cycle (1/2 hr cycle).

APS 113-LA Lightweight Armature

The body of the **ELECTRO-SEIS** Shaker is retained but the armature and guidance system are replaced with elements offering substantial weight reduction. The drive coil is lightened — with corresponding reduction in maximum force — and the armature guidance system elements are reduced in size and weight. This results in a corresponding reduction in cross axis stiffness and load carrying ability. The long stroke capability is retained and the frequency range for maximum force output is extended to 1000 Hz.

The Lightweight Armature is a desirable feature when using the shaker for exciting structures having low modal mass.

SPECIFICATIONS

	Model 113	Model 113-AB	Model 113-LA	Model 113-LZ	Model 113-HF
Maximum Force (vector)	30 lb 133 N	30 lb 133 N	10 lb 45 N	30 lb 133 N	42 lb 186 N
Maximum Velocity (vector)	30 in/s 76 cm/s	30 in/s 76 cm/s	30 in/s 76 cm/s	30 in/s 76 cm/s	30 in/s 76 cm/s
Maximum Stroke (p-p)	6.25 in 158 mm	6.25 in 158 mm	6.25 in 158 mm	6.25 in 158 mm	6.25 in 158 mm
Armature Weight	4.9 lb 2.2 kg	5.1 lb 2.3 kg	6.7 lb 3.0 kg	5.0 lb 2.27 kg	4.9 lb 2.20 kg
Maximum Overhung Load at Armature Attachment Point	20 lb 9 kg	2 lb 9 kg	2 lb 9 kg	20 lb 9 kg	20 lb 9 kg
Air Pressure Required	N/A	30 psig 2 kg/cm ²	N/A	N/A	N/A
Armature Coil Impedance	3 Ohm	8 Ohm	4 Ohm	8 Ohm 2 Ohm	4 Ohm
Total Shaker Weight	90 lb 36 kg	80 lb 36 kg	75 lb 34 kg	80 lb 36 kg	90 lb 36 kg
Shipping Weight	100 lb 45 kg	100 lb 45 kg	95 lb 43 kg	100 lb 45 kg	100 lb 45 kg
Overall Dimensions					
Length	20.7 in 526 mm	20.7 in 526 mm	20.7 in 526 mm	20.7 in 526 mm	20.7 in 526 mm
Width	8.4 in 213 mm	8.4 in 213 mm	8.4 in 213 mm	8.4 in 213 mm	8.4 in 213 mm
Height	6.6 in 168 mm	6.6 in 168 mm	6.6 in 168 mm	6.6 in 168 mm	6.6 in 168 mm
Matching Power Amplifier					
Sine Wave	APS 114	APS 114	APS 114	APS 124	APS 124
Random				APS 124-EP	APS 124-EP

50% Duty Cycle

Appendix B: Advanced Beam State Space Formulation

$$A = \begin{bmatrix} 0 & & & 1 & & & \\ & 0 & & & 1 & & \\ & & 0 & & & 1 & \\ & & & 0 & & & 1 \\ -153.21 & & & & -1.584 & & \\ & -21672 & & & & -6.949 & \\ & & -156292 & & & & -9.567 \\ & & & -7035.9 & & & -1.407 \end{bmatrix}$$

$$\Phi = \begin{bmatrix} 1.2165 & 8.9336 & 8.2405 & 0 \\ 3.3689 & 9.9497 & 5.2033 & 0 \\ 6.1463 & -.7806 & -.6255 & 0 \\ 0 & 0 & 0 & 6.5328 \end{bmatrix}$$

$$\Phi^T D_u = \begin{bmatrix} 6.1463 & -6.1463 & -1.2165 & 3.3689 \\ -.7806 & .7806 & -8.9336 & 9.9497 \\ -.6255 & .6255 & -8.2405 & 5.2033 \\ 6.5328 & 6.5328 & 0 & 0 \end{bmatrix}$$

$$C_\phi = \begin{bmatrix} 1.2165 & 8.9336 & 8.2405 & 0 \\ 3.3689 & 9.9497 & 5.2033 & 0 \\ 6.1463 & -.7806 & -.6255 & 6.5328 \\ -6.1463 & .7806 & .6255 & 6.5328 \end{bmatrix}$$

$$B = \begin{bmatrix} 0 \\ \phi^T D \end{bmatrix}$$

$$C = \begin{bmatrix} 0 & | & C_\phi \end{bmatrix}$$

For the estimator used in the optimal control designs of Chapter VI

$$Q = .1 * I(4 \times 4)$$

$$R_0 = 50 * I(4 \times 4)$$

$$G^T = \begin{bmatrix} I(4 \times 4) & | & I(4 \times 4) \end{bmatrix}$$

$$Q_0 = GQG^T$$

For the controller used in the optimal control design #1

$$Q_c = \begin{bmatrix} 0 & & & & & & \\ & 1 & & & & & \\ & & 0 & & & & \\ & & & 1 & & & \\ & & & & 0 & & \\ & & & & & 10 & \\ & & & & & & 0 \\ & & & & & & & 1 \end{bmatrix}$$

$$R_c = \begin{bmatrix} 2 & & & & \\ & 2 & & & \\ & & 3 & & \\ & & & 10000 & \\ & & & & \end{bmatrix}$$

Appendix C: Z-248 Modifications

This appendix discusses reasoning for, and results of a modification to a Zenith 248 computer. The modification was performed by Capt. Dave Jacques (GAE-89D) and Mr. Dan Rioux (ENY Lab Technician). The modification consisted of the following:

1. Installation of a 386 upgrade kit. This kit replaces the 286 microprocessor, main memory, and the I/O card.
2. Installation of a 64KB memory cache board.
3. Replacement of the 2MB memory expansion board with a 4MB (32 bit) expansion board.
4. Replacement of the 80287 math coprocessor with an 80387 math coprocessor.
5. The addition of a 40 MB hard drive.

Background

The subject Z-248 machine is being used in the aero lab (room 150) for structural dynamics and control research. The STAR MODAL software package, together with a B&K Signal Analyzer, is being used for experimental modal analysis. STAR MODAL runs under Microsoft Windows on the Z-248. Because Windows is a graphics environment, any programs which use Windows as a shell are inherently slow. The problem compounds itself each time an additional window is put on the screen. STAR MODAL has the additional complication of requiring lengthy calculations to perform many of its functions. Articles in PC Magazine and other publications suggested that Windows applications are best suited for 80386 based computers because of the

increased speed of these machines. The aero department already had several 386 upgrade kits, and it was decided that the subject Z-248 would be used as a test case for the upgrade kits.

Discussion

The basic upgrade kit consists of a backplane board, 16 MHz 80386 microprocessor board, 1MB Main Memory Board, and I/O Card. The new backplane board provides 32 bit expansion slots for additional memory boards, as well as 8 bit and 16 bit slots for standard Z-248 cards. The microprocessor board provides slots for both an 80287 and an 80387 math coprocessor. Installation of the upgrade kit requires complete removal of all circuit cards in the Z-248. The new backplane board used the same mounting holes and hardware as the old one, and there were no complications with the installation procedure. The entire process of installing the upgrade kit took approximately one hour. The 2MB (16 bit) memory expansion board that was present in the Z-248 prior to the upgrade could not be used because the 16 bit memory card is not compatible with the 32 bit slot in the new backplane board. All other cards (including the video card, Codas A/D board, and GPIB board) are compatible and are being used in the upgraded Z-248.

Benchmark tests of the upgraded Z-248 revealed significant speed increases due to the 386 processor. The PC Tools speed rating was 890% (% of original IBM PC performance) after the upgrade, as compared to 375% prior to the upgrade. (The standard Z-248 uses an 8 MHz 80286 microprocessor.) Despite the significant improvement in the benchmark tests, the difference was not nearly as noticeable while running programs. This was primarily due to slow disk access times. Additional delays are caused by a fast processor having to wait for slower memory, and at the time of the original upgrade the 80387 math chip had not yet come in. Therefore, the computer was

still using an 8 MHz 80287 math coprocessor for numeric calculations. Once the new math chip was added, times for numerical computations decreased by more than a factor of two.

In order to alleviate delays caused by the memory limitations, several other modifications were made to the Z-248. A 4MB, 32 bit memory expansion board (Z-515 card) was installed primarily for use as a RAM disk and disk cache. A 64KB high speed memory cache board (Z-525 card) was installed to improve memory access time. A memory cache works in much the same way as a disk cache by writing most frequently used information into high speed (25 nsec) memory while the system memory operates at a slower speed (100 nsec).

The memory cache board made a modest improvement in the benchmark ratings, improving from 890% to 960%. However, the combination of the RAM disk and the memory cache significantly improves the speed as seen by the operator while running applications. The delays in waiting for graphics screen recalculation much shorter. In general, the computer is noticeably more "lively" with the additional modifications.

There were several annoying problems encountered while installing the memory expansion board which should be noted. The memory board can be used for either extended or LIM/EMS expanded memory. If the LIM/EMS memory is to be used, a device driver (EMM.SYS) must be loaded in the config.sys file. This driver is only found in Zenith DOS version 3.21 or later. The first problem encountered is that the diagram found in the board installation instructions does not indicate how much memory will be set aside for EMS under specified switch settings. The Z-386 manual supplied with the upgrade kit should be consulted for this information. A second problem encountered is that Windows v2.03 would not run if EMM.SYS was loaded, thereby eliminating the possibility of using LIM/EMS memory with this version of Windows. It

is possible that a later version of Windows would have alleviated the problem with the EMM.SYS driver.

The second hard drive was added for two reasons; additional disk storage was required for programs and data files, and a faster hard disk access time was desired. The hard disk that came with the machine was a relatively slow (67ms access time) 20 MB drive. The new hard disk offered modest speed improvements (40ms access time) and double the storage space. To further enhance the disk access performance, a hard disk cache was set up with the additional memory on the 4 MB expansion board. The only disk caching program which would work with Microsoft Windows was SMARTDRIVE (supplied with Windows); therefore this is the program which was used. SMARTDRIVE significantly improves the performance (read speed) of Windows by allowing it to read disk files from fast memory instead of a relatively slow hard disk.

An additional problem which developed not related to the upgrade kit (as far as could be determined) was software limitations brought on by Windows. Desqview-386 multitasking software was purchased with the intention of using it on the modified Z-248. However, the 386 memory manager supplied with Desqview (QEMM-386) was incompatible with Windows. This seemed to be primarily a problem with Windows because it was the only piece of software which was tried and would not work with Desqview. This problem only reinforced a lesson which was learned during the course of this modification, the lesson being: Microsoft Windows is not configured to a particular machine, the machine is configured to Windows!

Recommendations

Graphics based software is inherently slower than text based programs because of screen recalculation. These and any other computationally intensive programs stand to

benefit from a 386 upgrade kit, and this option should be considered. However, the old memory expansion boards are not compatible with the upgrade kits. If RAM disks or other expanded memory applications are to be used, new 32 bit memory boards will need to be purchased. Additional speed increases can be realized by installing a memory cache board, and if the primary applications on the Z-248 are math intensive, an 80387 math coprocessor should also be considered. An additional performance enhancement which was not included in the subject Z-248 is a high speed video card. There are many 16-bit video cards commercially available, and these would make a noticeable difference in the screen refresh rate for graphics based software. A word of warning on the 16-bit video cards however; the AFIT AERO department machines equipped with the CODAS data acquisition systems are incompatible with these cards because the CODAS system requires a jumper connection to an EGA monitor, while the 16-bit cards have only VGA connections. (The video modes of these new cards can handle the EGA modes, but the hardware connections are incompatible.)

The only problems with the entire upgrade were due to the memory expansion board. Zenith should be contacted concerning software incompatibilities between DOS, Windows and the memory expansion boards.

Vita

David R. Jacques was born [REDACTED] At an early age he moved with his parents to Bethlehem, Pennsylvania where he graduated from Liberty High School in May, 1978. Following high school, he attended Mansfield State College as a music education major for one year before transferring to an engineering curriculum at Lehigh University. In August of 1980 he joined the Air Force ROTC program at Lehigh, and in June of 1983 he received the degree of Bachelor of Science in Mechanical Engineering and was commissioned as a Second Lieutenant in the Air Force. His first assignment was to the Foreign Technology Division, Wright-Patterson AFB where he served as an armament systems analyst. In March of 1988 he married [REDACTED] and in May of 1988 he left the Foreign Technology Division and entered the School of Engineering, Air Force Institute of Technology, Wright-Patterson AFB, Ohio.

REPORT DOCUMENTATION PAGE

Form Approved
OMB No. 0704-0188

1a. REPORT SECURITY CLASSIFICATION UNCLASSIFIED			1b. RESTRICTIVE MARKINGS		
2a. SECURITY CLASSIFICATION AUTHORITY			3. DISTRIBUTION / AVAILABILITY OF REPORT Approved for public release; distribution unlimited		
2b. DECLASSIFICATION / DOWNGRADING SCHEDULE					
4. PERFORMING ORGANIZATION REPORT NUMBER(S) AFIT/GAE/ENY/89D-15			5. MONITORING ORGANIZATION REPORT NUMBER(S)		
6a. NAME OF PERFORMING ORGANIZATION School of Engineering		6b. OFFICE SYMBOL (If applicable) AFIT/ENY	7a. NAME OF MONITORING ORGANIZATION		
6c. ADDRESS (City, State, and ZIP Code) Air Force Institute of Technology (AU) WPAFB, OH 45433-6513			7b. ADDRESS (City, State, and ZIP Code)		
8a. NAME OF FUNDING / SPONSORING ORGANIZATION		8b. OFFICE SYMBOL (If applicable)	9. PROCUREMENT INSTRUMENT IDENTIFICATION NUMBER		
8c. ADDRESS (City, State, and ZIP Code) WRDC/FIBG WPAFB WL/ARCD Kirtland AFB			10. SOURCE OF FUNDING NUMBERS		
PROGRAM ELEMENT NO.	PROJECT NO.	TASK NO.	WORK UNIT ACCESSION NO.		
11. TITLE (Include Security Classification) BASELINE EXPERIMENT FOR ACTIVE CONTROL OF STRUCTURAL VIBRATIONS					
12. PERSONAL AUTHOR(S) David R. Jacques, B.S., Captain, USAF					
13a. TYPE OF REPORT MS Thesis		13b. TIME COVERED FROM _____ TO _____		14. DATE OF REPORT (Year, Month, Day) 1989 December	
15. PAGE COUNT 117					
16. SUPPLEMENTARY NOTATION					
17. COSATI CODES			18. SUBJECT TERMS (Continue on reverse if necessary and identify by block number)		
FIELD	GROUP	SUB-GROUP	Vibration Control Vibrators (Mechanical)		
13	09		Structural Vibrations		
			Flexible Spacecraft		
19. ABSTRACT (Continue on reverse if necessary and identify by block number) Thesis Advisor: Dr. Robert A. Calico Jr. Dean, School of Engineering					
20. DISTRIBUTION / AVAILABILITY OF ABSTRACT <input checked="" type="checkbox"/> UNCLASSIFIED/UNLIMITED <input type="checkbox"/> SAME AS RPT <input type="checkbox"/> DTIC USERS			21. ABSTRACT SECURITY CLASSIFICATION UNCLASSIFIED		
22a. NAME OF RESPONSIBLE INDIVIDUAL Dr. Robert A. Calico Jr., Dean, Sch. of Engr.			22b. TELEPHONE (Include Area Code) (513) 255-3025		22c. OFFICE SYMBOL AFIT/EN

UNCLASSIFIED

A baseline experiment is developed which can be used to evaluate control systems for large space structures. The experiment consists of an inverted cantilever beam. Proof mass actuators and a structural dynamics shaker provide the control forces, and integrated output of beam-mounted accelerometers provides velocity feedback. A programmable controller allows different control algorithms to be evaluated. System damping and frequency response are determined with and without the controller engaged, and experimental results are compared to analytical predictions. Modal suppression techniques are attempted in order to demonstrate active control of selected modes while maintaining overall system stability.

UNCLASSIFIED